2-1-2013

MEMS based heavy metal detector

Inas Ramsis

The American University in Cairo

School of Sciences and Engineering

MEMS Based Heavy Metal Detector

By

Inas Raafat Ramsis

A thesis submitted in partial fulfillment of the requirements for the degree of

Master of Science in Nanotechnology

Under the supervision of:

Dr. Sherif Sedky

Professor of Physics, American University in Cairo

Founding Provost, Zewail University

Dr. Mohamed Serry

Assistant Professor, department of Mechanical Engineering, American University in Cairo.

Dr. Mohamed Swillam

Assistant Professor, Physics department, American University in Cairo.

Fall 2012

To my family,

my brother.

Acknowledgements

I would like to express my deep thankfulness to all the people who helped me in fulfilling this research and rendering it to such a level. First and foremost, I would like to thank my supervisor Prof. Sherif Sedky for his valuable contributions to this research, and for his support, guidance, and his endless knowledge and research skills that he taught me during this research that without it this work would have never been achieved. I also would like to acknowledge the support and guidance of Dr. Mohamed Serry and his valuable contribution and comments that guided me during the research, and also for his guidance for me during the fabrication phase which taught me how to use the clean room facilities at the American University in Cairo (AUC). I would like to acknowledge Dr. Mohamed Swillam for his valuable contribution and guidance in research and for his valuable comments that taught me a lot during the optical design and simulation and that without them this work would not have been achieved.

I would like also to thank my colleagues, especially Eng. Kareem Khairallah for his help and contribution in the optical design. I would also like to acknowledge Eng. Mohamed Ibrahim for helping me during the use of microfabrication facilities, also I would like to thank Eng. Hani Tawfik for helping me in taking the SEM images.

I would like to express my deep appreciation for The Youssef Jameel Science and Technology Research Center (YJ-STRC) that has provided me with financial support and state-of-the-art equipment to conduct this work.

At last but not least I would like to express my warm appreciation for my family because everything I have achieved is because of them, without their love, inspiration and guidance I would not be able to come to this point, thank you so much for being there for me.

Abstract

Water pollution by toxic heavy metals is one of the most serious environmental hazards to humans' health. As they are emitted into the water resources and adsorbed by soil, plants, fish and animals and eventually accumulate in human bodies causing a variety of serious diseases. Therefore, there is an urgent need to develop a continuous, rapid, automatic, and on-site heavy metals environmental monitoring system for the online detection of heavy metals pollution at various water resources and industrial waste networks.

In this thesis the main objective is to develop a microfluidic platform for heavy metal analyte sensing in which a variety of sensing schemes can be applied. The proposed platform contains microfluidic microchannels for the handling and separation of heavy metal analytes to improve the selectivity, integrated with a sensing device for the optical detection and monitoring of various heavy metal analytes and concentrations.

In this context, the design and micro-fabrication of polymer based microchannels were conducted as the microfluidic platform on which the integration of the various optical sensing materials can take place. Afterward a novel design of MEMS based Fourier transform spectrometer is proposed, in which a new scheme for input Gaussian beam splitting into symmetrically two semi Gaussian beam is introduced using V shape mirror. The design is fully integrated and can operate in the Infrared and visible region. The analysis shows that, a minimum resolution of $9nm$ at a wavelength of $1.45\mu m$ and a mechanical displacement of $160\mu m$ is achievable. Unlike the traditional Michelson interferometer which returns half of the optical power to the source, this design uses the full optical power to get the interference pattern using movable reflecting mirrors thus enhancing the signal to noise ratio, and allowing the use of differential moving scheme for the mirrors which increase the optical path difference by a factor of four. An analytical model that describes the beams propagation and interference is derived using Fourier optics techniques and verified using Finite Difference Time Domain (FDTD) method. Then, a mechanical model that describes the mirror displacement to produce optical pass difference is derived and verified using finite element method (FEM). Finally, the effect of different design parameters on the interference pattern, interferograme and resolution are also shown.

Table of Contents

List of Figures

List of Tables

1 Chapter I Introduction

Environmental pollution by toxic heavy metals is one of the most serious environmental hazards to humans' health. By definition heavy metals are metals having an atomic weights varying between 63.5 and 200.6 $gmol^{-1}$, and their density is higher than 5 gcm^{-3}. Small doses of heavy metals are sometimes necessary for some living organisms, however when such doses exceed a certain level it becomes dangerous and additionally some types of heavy metals are not important for living organism, and they can be considered as source of toxicity and affect water resources and influence humans health like mercury, cobalt, lead and cadmium [1, 2].

Due to the fast increase in urbanization and industrialization, heavy metals are transported to water resources through water runoff, causing water contamination by receiving polluted bodies and species from urban and industrial areas, As all of these polluted species are emitted into the water resources and accordingly adsorbed by plants, fish and animals and overtime accumulate in human bodies thus cause a variety of serious diseases (Illustration in Figure 1.1). For example, mercury (Hg), that is a widely used material in the fabrication of industrial chemicals and electronics, causes kidney and brain damage upon exposure. Lead (Pb) which can be accumulated in humans' body leading to an increase in blood pressure, and Cobalt (Co) that is used in many industries like heavy metal production, diamond polishing. As most heavy metals are non-biodegradable and they are also chemically stable, they can accumulate for very long time in humans body and the environment [3-5]. When humans are exposed to such type of metals, they may be subject to many diseases such as asthma. Accordingly, these elements are easily absorbed by plants and animals, or they can be released in air and water thus affecting human health as they are accumulated in their body causing several severe diseases.

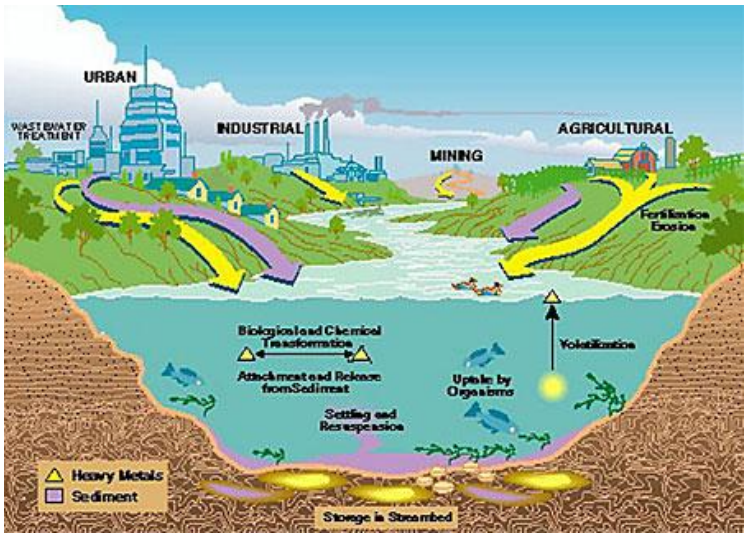

Figure 1.1 Water pollution with Heavy metals [2-3]

Due to its serious environmental hazardous effect on humans' health, environmental monitoring systems of heavy metals are highly desired. The monitoring systems of heavy metals can be used to check the existence of heavy metals in lakes and rivers or to confirm the purity of water from heavy metals traces after the handling of water.

To measure the traces of heavy metal, conventional methods with high capabilities and sensitivity in tracing low level of heavy metal ions have been used, such as inductively coupled plasma mass spectroscopy (ICP-MS), atomic absorption spectrometry (AAS), electrochemical and potentiometric techniques, X-ray fluorescence, and molecular absorption spectroscopy [3, 6].

Figure 1.2 illustrates the procedure followed in conventional heavy metals detection techniques which incorporate the following steps:

- Sample collection step.
- Transportation of the samples from the field to the laboratories where tests are conducted.
- Sample preparation steps.
- Analysis and measurements steps.

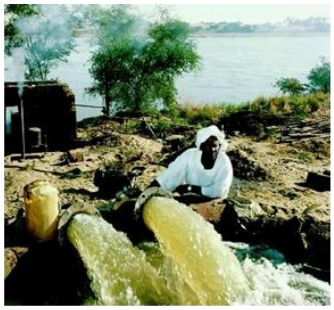

Sample collection

Sample preparation and analysis

Figure 1.2 Illustration of sample collection and treatment needed in conventional method monitoring (Non-robust sampling and analysis techniques) [3-4]

The current conventional heavy metal detection methods suffer from the following drawbacks; the sample collection and preparation steps are costly and time consuming. Additionally sample composition may be damaged or altered due to time delay, these methods are inaccessible to remote areas which suffers the most from water pollution. Additionally it is necessary to have online monitoring by government and remote accessibility to detect any change or pollution in water resources.

1.1 Objectives

Therefore, there is a dire need to develop an online, automatic, continuous and rapid monitoring system, which can be accessible to remote areas. Accordingly, our main objective is to develop a microfluidic platform that can be used for sensing heavy metal ions using a variety of optical sensing materials. The proposed system is divided into two parts; the first one includes microfluidic microchannels for handling and separation of heavy metal analytes in which the sensing material with the appropriate buffer can be integrated to improve selectivity. Then the microchannels are integrated with a sensing device for the optical detection and monitoring of various heavy metal analytes and concentrations (Figure 1.3). The integration of this system will result in the following advantages:

- Online detection
- Higher sensitivity and faster response time
- No need for sample preparation
- Higher versatility, capability of detecting variety of heavy metals (Hg, Cd, As, Pb, and Cr).
- Remote sensing
- Accessibility to remote areas

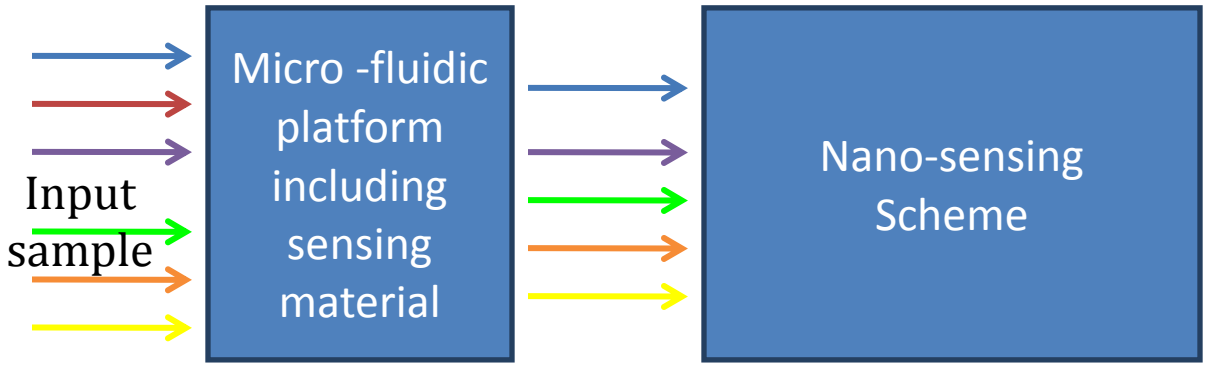

Figure 1.3 Schematic for the proposed system for the online monitoring of heavy metals in water

In this context, this work focus on the microfabrication of microfluidics channels for the microfluidic platform, for the handling and integration of the sensing materials of heavy metals. In addition, it considers verification, analysis and optimization of micro-spectrometer as an optical sensing device for the heavy metal detection.

1.2 Monitoring Schemes of heavy metals

Many monitoring and sensing on-site techniques have been developed for on-site detection of heavy metals in water; their working principle may be based on optical detection, piezoelectric sensors, bio detectors that involve enzyme and ion selective electrodes and electrochemical sensors. The profits of on-site detection of heavy metals are the automatic analysis conducted in the field without the need of sample collection, transportation and preparation before the analysis. In the following sections, an overview of optical detection and electrochemical sensing of heavy metals is given which can be then integrated on a suitable microfluidic platforms for environmental online monitoring systems [4-6].

1.2.1 Optical detection of heavy metal

Between the various detection techniques, optical sensing of toxic heavy metals is one of the most widely used methods for the detection of contaminating elements with great commercial benefits. Optical sensors can be described as small devices that respond to the presence of heavy metals by generating an optical signal proportional to the type and concentration of the heavy metal. Optical sensors are basically formed of the following elements;

- Sensitive material where a precise interaction occurs helping in the identification of the analyte.
- A transducer that converts the product of the interaction into an optical signal.
- An optical sensor that consists of a photodetector or microspectrometer is required for the detection of the output optical signal. This optical signal may be absorbance, transmittance, reflectance or any other optical change in the spectrum [7].

Recently, optical sensors for heavy metal detection have gained more interest. The concept of optical sensing of heavy metal can be through intrinsic ion sensing of heavy metal, or the use of lipophilic ionophores, or the use of immobilized indicators dyes [4, 8].

Generally in intrinsic ion sensing, the sensing mechanism can be conducted through the intrinsic properties of the heavy metal ions, as various metal ion undergo changes in absorption spectra in the visible region to the near infrared region which can be optically sensed[9, 10]. The lilophilic-ionophores for the detection of heavy metals are considered as carriers to enhance the selectivity of the optical sensors. In this scheme the detection process is conducted through these ionophore receptors, in which ions can bind selectively, additionally these ionophores can be combined with chromophores or fluophores. In this case the ionophores bind with the metal ion while the chromophore or the fluorophore converts this binding into an optical change that can be detected [11-13]. Figure 1.4 illustrates the basic principle of using a fluoroionophore for optical detection; in this case the analyte binds selectively to the fluoroionophore which results in a fluorescence emission that is optically detected.

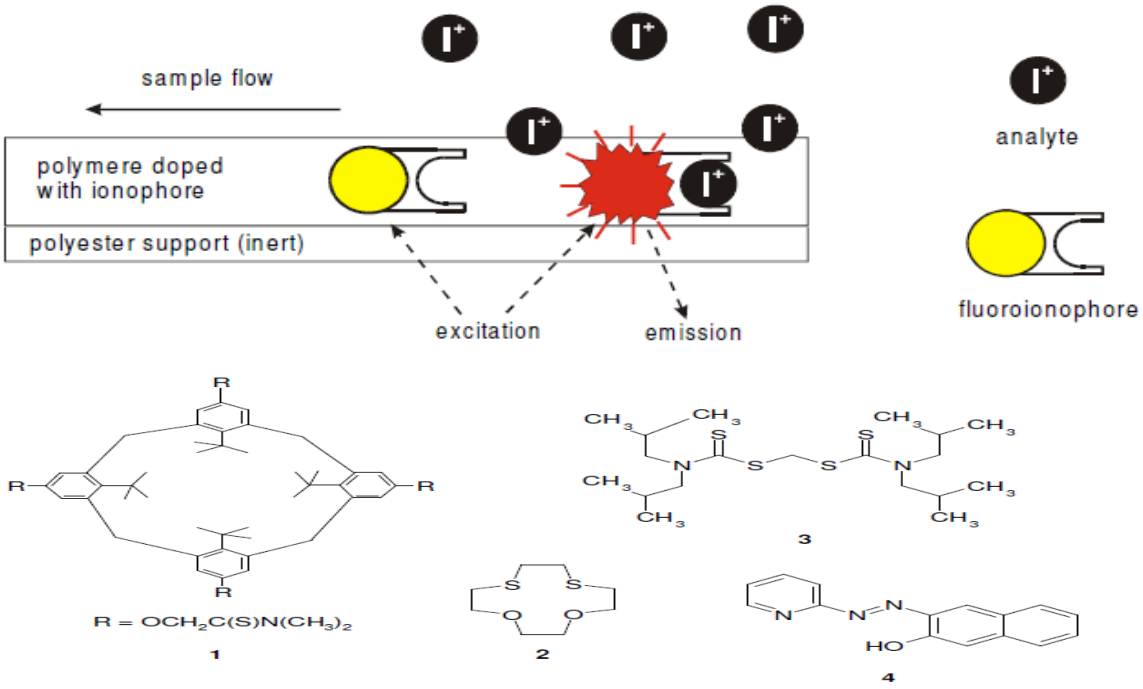

Figure 1.4 Illustration of the Fluoro-ionophore sensing mechanism, example of various types of ionophores used in optical sensing [4]

From these types of optical sensors used before by Yang et al., synthesized chromophores- and fluorophores functionalized polymers for Co (II) ion detection. However they required long synthesis process, complex analysis, delay in the signal response and they suffer from low selectivity and sensitivity [14].

Even though a lot of research and work have been conducted in the field of optical sensing of heavy metals still it undergoes several disadvantages such as low selectivity, sensitivity instability, and reversibility of the process. To overcome these drawbacks new schemes including combination of several approaches and additional adjustment and buffers may be introduced to increase the selectivity of the optical indicators [15].

Lately new nano-materials with controlled size, shape, and composition that provide a great development in the optical sensing of heavy metals have been developed by El-Safty et al. [5]. This new class of optical sensors is developed by using 3D monolithic discs as chromophore platforms which allow sensitive detection of metal ions up to sub-picomolar ($<10^{-11}$ mol/dm^3) and at the same time this is done with fast time response within few seconds [5].The detection takes place through the strong interaction with metal ions through [metal-Probe] complexation. As a result of these interactions, color changes with addition of high concentration of metal ions. As a reaction to the binding between the heavy metal analyte and chemical-probes an optical signal in the visible light spectrum is detected (Figure 1.5), that is proportional to the concentration of the analyte, which is then detected through an optical spectrometer which has an enhanced properties for the selectivity and reversibility of the operation [14, 16].

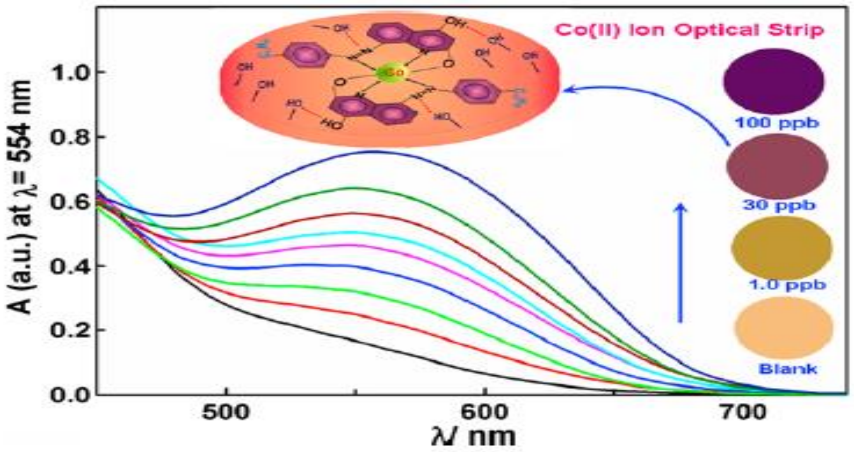

Figure 1.5 3D monolithic optical sensors [14]

In this section a brief overview of the different approaches used for optical sensing of heavy metal was discussed, in the following section an overview of another approach for heavy metal detection using electrochemical sensing is given. Next, a survey on the microfabrication of microfluidic channels will be given followed by an overview of the different types of MEMS based spectrometers that can be used as a sensing device for the monitoring of heavy metals using optical schemes thus reviewing all the components needed for the microfluidic platform to reach an on-site detection of heavy metals.

1.2.2 Electrochemical method for heavy metal detection

Electrochemistry can be widely used for environmental online monitoring. Electrochemical detectors fulfill many advantages for the on-site monitoring of contaminants as it is highly selective, rapid, sensitive, and low cost, additionally it can be designed in a compact and portable way. The working principle of such sensors is based on having a transducing element covered with recognition element, which can be either a biological or a chemical element (Figure 1.6). In this case the required information about the contaminant is acquired through an electrical signal resulting from the interaction between the target analyte and the recognition element. It is generally based on three electrodes configuration; working electrode, reference electrode and counter electrode [17, 18].

The electrochemical sensors can be divided into two main groups according to the resulting electrical signal; either amperometric or potentiometric electrochemical sensors. In amperometric based electrochemical sensor, the transduction of the output detected signal is done by fixing the electric potential of the working electrode relative to the reference electrode at a specific value and then detect the output current signal versus time. The potential is used for the electron transfer; the output current signal is proportional to the rate of electron transfer reaction which is related to the amount of the recognition element giving results about the concentrations of the analyte. In case of potentiometric electrochemical sensor, the detected signal is acquired through a conversion of the recognition process into a potential signal that is proportional to the amount or concentration of the analyte that goes through the recognition

process. In these detectors, ion selective electrodes are mainly used to obtain the potential signal. In spite of the fact that these types of sensors are very simple, with low cost and high selectivity, they still suffer from low sensitivity and take longer time than the amperometric sensors which are being more widely used now [18, 19].

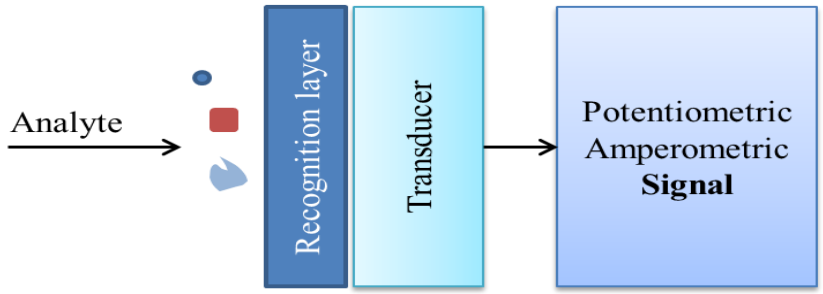

Figure 1.6 Electrochemical sensors scheme

One of the important constituents of the electrochemical sensors is the transducing element that is why there is an ongoing research for the development of the material used as a transducer in the electrochemical sensor. Due to the development in the area of nanomaterials, this unique kind of material offers a great advantages and development in the electrochemical sensors as they have exceptional mechanical, chemical and electrical properties which make them highly useful for the electrochemical sensors in comparison to the conventionally used materials. Additionally these nanostructures have high surface area which result in higher electron transfer and increase the amount of ions detected at lower time. These nanomaterials could be carbon nanotubes, graphene, nanoparticles or any other nanostructures that can be developed to be used in electrochemical sensing. Due to the advantages offered by the small size and unique properties of nanomaterials, this will help in the development of heavy metal detection techniques with higher selectivity and sensitivity. In addition, it will make it possible to go for further miniaturization in the sensors size so that it can be easily used in on-line monitoring and integrated with the whole platform in order to achieve a complete device for environmental monitoring. In this context, nanostructures platforms and nanomaterials based electrochemical electrodes ranging from carbon based nanomaterials to metallic nanoparticles and other natural nanostructures are being examined for the development of electrochemical sensing [20].

Carbon based nanostructures such as carbon nanotubes, graphene and fullerenes has gained a lot of interest to be used as electrodes or to modify conventional ones in the field of electrochemical sensing of heavy metals. Carbon nanotubes (single wall or multi-wall nanotubes) can be great candidates due to their unique properties, electrocatalytic activity and high surface area. Accordingly the modification of carbon nanotubes with functionalized molecules which have higher affinity to specific ions of heavy metal is a good approach for developing electrochemical electrodes with higher selectivity towards chosen target analytes. Additionally it increases the sensitivity at lower accumulation time due to the high surface area of these nanmomaterials thus acting as a preconcentration that concentrate the ions. Figure (1.7a, 1.7b) shows an example of carbon nanotubes functionalized with Cysteine for the detection of Pb^{2+} and Cu^{2+} [21]. Beside the use of carbon nanotubes in modifying the electrochemical electrodes, metallic nanoparticles have been also studied to enhance the properties of the electrodes. As an example Figure 1.7c shows the use of gold nanoparticles (AuNPs). In this approach, first DNA strand is immobilized on a gold electrode, on the other side another complementary DNA strand containing T-T mismatch. On this second strand is an immobilized gold nanoparticle. In this case when the mercury ions exist it forms a complex T-Hg^{2+}-T, thus enabling the immobilization of gold nanoparticles on the electrode. After that a CV measurement is obtained of the RuHA complex that is existing which can be associated to the percent of DNA on the surface, that is by its turn is proportional to the concentration of the existing mercury ions [21, 22].

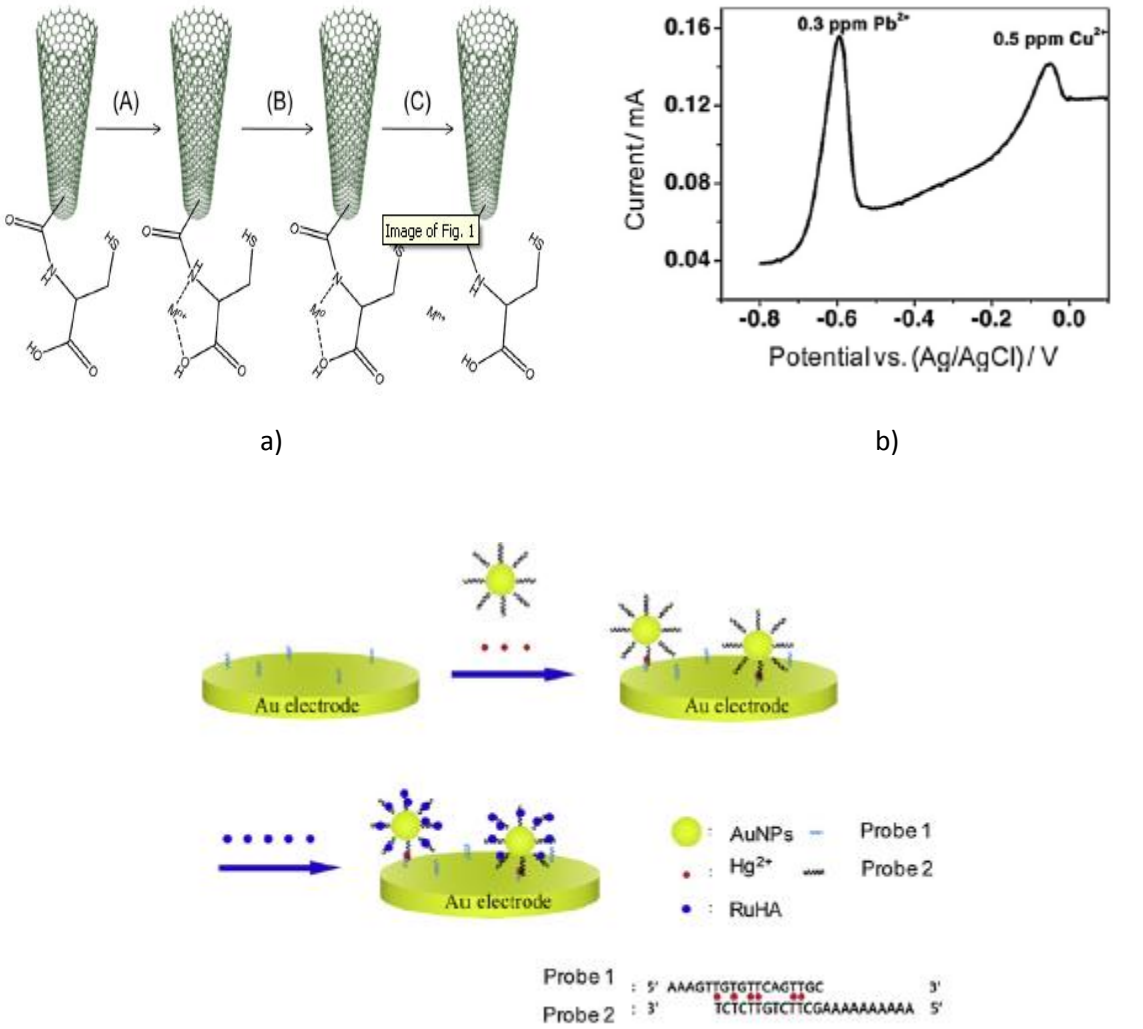

Figure 1.7 Carbon nanotubes based electrochemical electrodes b) output signal for anodic stripping voltametry detecting Pb and Cu ions c) gold nanoparticles (AuNPs) for the detection of mercury ions Hg^{2+}[20]

Nanomaterials are also used to enhance the performance of potentiometric based electrochemical sensing. In potentiometric sensing mainly two devices are generally used; ion selective electrode and field effect transistors. Figure 1.8 shows an example of using nanostructures to enhance field effect transistors for electrochemical sensing. Field effect transistors are based on measuring the

current flow across the transistor between the drain and source. The drain and source are connected via semiconducting channel, the conductivity of which is varied by external potential. Nanostructures with their unique properties when they are incorporated into field effect transistors enhance the stability of its response and its performance. Usually the semiconducting channel is replaced by carbon nanotubes or semiconductor nanowires. These nanostructures enhance the sensing capabilities to a very low detection limit, and also they can be functionalized to have certain selectivity towards specific target ion thus enabling the concentration and separation at the same time. Silicon nanowires have been used for copper ions detection by modifying them with glycyl-glycyl-histidine as a copper ion detecting agent. The concentration of copper ions was measured as a function of the change in the conductance of the silicon nanowire. Another example using single wall carbon nanotubes for mercury ions, single wall carbon nanotubes are affected sensitively by the chemical environment around them due to their band gap energy dependence on the dielectric or reduction that is happening. Figure1.8a shows that when the nanotubes are exposed to mercury ions a reduction of mercury ions takes place converting them from Hg^{+2} to Hg^{o} allowing their deposition on the carbon nanotube wall. Additionally a change in the conductance proportional to the mercury ions concentration takes place; Figure 1.8b shows a change of current with respect to the time according to the concentration of existing Hg ions. However when lead ions Pb^{+2} are present, the same reaction doesn't occur which proves the specifity of the sensor and this can be due to the fact that mercury ions are thermodynamically favorable to make a reduction reaction with the nanotubes than the lead ions which remain Pb^{+2} and no reduction can take place [20, 23].

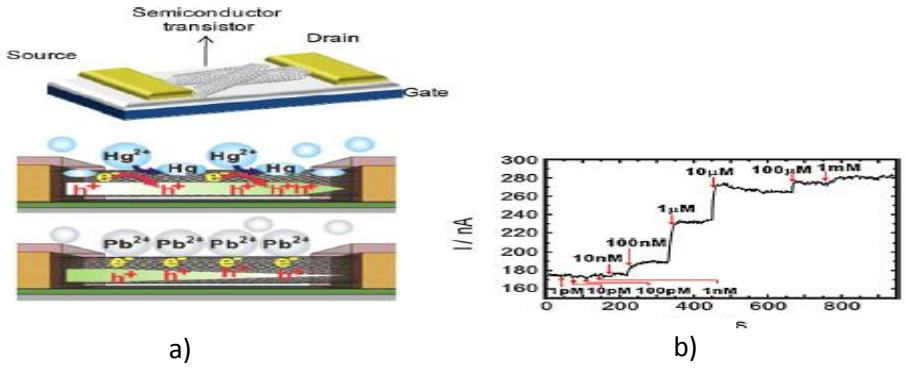

a) b)

Figure 1.8a) Example of potentiometric electrochemical sensors using field effect transistor (FET) with single wall NT for selective detection of Hg b) Change in current with respect to the time according to the existing concentration of Hg ions [20]

Electrochemical sensing is a highly efficient technique for heavy metals ion detection, and the incorporation of nanomaterials can enhance the detection level and also allow the miniaturization of the system to be integrated on microfluidic platforms for on-site monitoring systems.

According to the two detection techniques discussed above, the optical detection and electrochemical sensing of heavy metals, they can be highly efficient for heavy metals detection. This work focus on the use of optical detection of heavy metals, thus in order to take advantage of these schemes a microfluidic platform for the integration of the optical material, or the electrochemical sensing electrodes need to be built, which can be used for the handling and separation of heavy metal ions in order to increase the selectivity and enables the diversity of the detector to be used for different types of heavy metals.

The aim of this thesis is to develop the microfluidic microchannels and to design an optical microspectrometer as a detector for the optical signal which can be integrated afterwards with the microfluidic platform. Hence in the following section a survey about the different techniques for microfluidic channels is presented in order to find the suitable approach for fabrication. Afterwards in this thesis the system is based on optical detection thus a review for the different types of microspectrometer commonly used is given as the optical sensing device.

1.3 Microfluidic microchannels

As the first part of this research consists on developing microfluidic platform for the fluid handling and the integration of fluid a sensing material, one of the main components of microfluidics is microchannel. Thus an overview on microfluidics microchannels is given in this section in addition to a review on the most commonly used microfabrication techniques for microchannels.

Recently, microfluidics are very commonly used in order to produce diverse miniaturized devices to be used in lab-on-a-chip applications and biomedical diagnostics. Generally, microfluidics are dealing with the performance, specific control and handling of fluids that are restricted to a small device space usually at a size range of a few millimeters. One of the most

important components in a microfluidic system is the microchannel which constitutes the core of the microfluidic system (Figure 1.9). Microchannels can be considered as a groove or a via that encapsulates or move the fluids from one part to another, its diameter ranges from 100 nanometers to several hundred micrometers, which make it very useful in mimicking the role of capillaries in the micron scale [24, 25].The fact of this micro scale is typically related to various features which include: small volumes, small dimensions, low power consumption and the effects of the micro dimensions which will be discussed later. As a result, these microchannels offer unique advantages in practical applications like sample handling, reagent separation, mixing and detection. In addition microchannels require small sample volume from 100nl to 1000µl which makes them ideal for handling costly and hard-to-obtain samples. Microfluidic channels, which first emerged in the 1980s, they are characterized by a wide range of applications which have been used commercially in the development of printer heads, cell separation, lab on a chip technology, and heat exchange applications [26, 27].

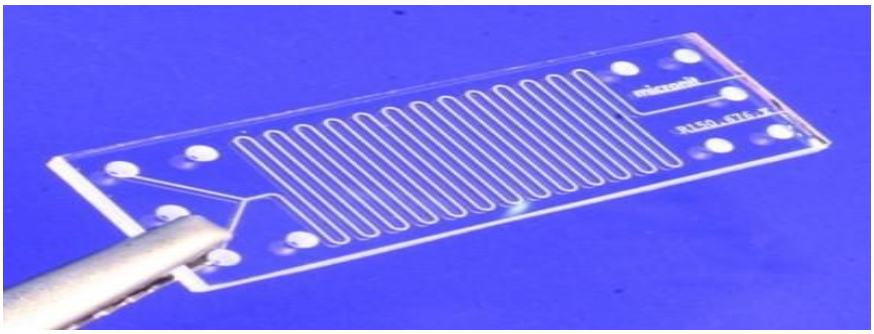

Figure 1.9 Microfluidic microchannel[22]

The basic principle of this fluidic microchannel which makes it unique and advantageous is that the performance of fluids at the microscale differs significantly from the performance of fluids at the macroscale. The difference in behavior involves the difference in many properties like surface tension, energy dissipation and the resistance of the fluids which all begin to control the system. Studies of microfluidics show how their performance changes and how they can be used for new applications. As a result, at these micro scales (channel diameters from 100 nm to 10 um), there are various interesting and unintuitive properties. Firstly, Reynolds's number in

particular, which compares the moment of a fluid to its viscosity, become very low. Therefore, the flow of fluids in the microchannels is strictly laminar. In addition, another key consequence is that when the fluid flow is laminar, there is no mixing that occur as in macrofluidics but diffusion dominates between them (see Figure 1.10), which enables the designed devices for separating and detecting cells that are based on the laminar fluid diffusion interface [25, 28]. Microfluidic channels are characterized by more uniform reaction conditions and higher grade products in single and multistep reactions. For fluid injection into the microchannel an external pump that forces the movement of fluid is used (this is usually a syringe pressure pump)[26].

Figure 1.10 Illustration of laminar flow using glacier as shown there is no mixing between the two sides of ice [28]

In conclusion, this miniaturized device system offers several advantages over conventionally macro devices, which includes lower need for solvents, reagents, and samples. This can be very useful for valuable samples with small reaction times, portability, lower cost, low energy consumption, higher functionality, and potential for parallel operation. An important application for the microfluidic device is blood flow in simple microchannels which can be used as a diagnostic tool [29]. In our case microchannels are used as housing for the mesoporous carriers with immobilized chemical-probes in which the water is injected to react with the carriers for the heavy metal detection.

With this recent development in microfluidic systems, there was an intense research in microchannels fabrication techniques, in order to reach simple fabrication process with low cost, low processing time and best biocompatibility. First microchannels were fabricated in silicon

substrates then in glass using conventional lithographic and etching techniques. Recently, there was a trend towards making microchannels using soft lithography or polymer based microchannels, in which the body of the microchannels is made out of a thick photoresist. The following section is a review on the development of microchannels fabrication techniques [27, 30].

1.3.1 Microfabrication

Microfabrication is defined as the process of making MEMS devices, MEMS stands for **M**icro-**E**lectro-**M**echanical-**S**ystems, so it is the idea of combining electronic circuits with mechanical components in one system in the micron scale [14]. Microfabrication is a wide term that it is used to describe the fabrication of miniaturized devices. It consists of the etching of silicon substrates, thin film deposition, micromilling. Microfabrication offers a very specific control in making the features. In the next section an overview of the different microfabrication techniques used for microchannels fabrication is given, such as bulk micromachining, surface micromachining, soft lithography fabrication and polymer based microchannels. In each technique the basic principle is given in addition to the advantage and disadvantage of each technique and how the development in microfabrication technology affects the costs and simplicity of the process to be suitable for new miniaturized systems [31].

1.3.1.1 Bulk micromachining of microchannels

Bulk micromachining can be described as the process that etches deeply into the substrate. In this technique the microchannels are made out of the bulk of the silicon wafer, which can be achieved by several means; dry etching or wet etching. For the dry etching, the reactive ion etching (RIE) is used to etch the microchannels into the substrate, but usually the use of the reactive ion etching gives rough surfaces and tapered side walls “This is especially the case when the width of the trench is on the same order of magnitude as the depth”, which could highly affect the fluid flow in the microchannels. While, on the other hand, if wet anisotropic etching is used with the appropriate crystalinity, this will result in vertical side walls that have mirror like finishing. After that the next step is to enclose the microchannels etched in the

substrate by bonding another wafer which could be glass substrate on top of the microchannels [31, 32].

A description of the fabrication process flow for bulk micromachining of microchannel is given in Figure 1.11 The process starts with a silicon wafer on which there is a thin layer of native oxide. Then a photoresist is spun on the wafer and the pattern is transferred using photolithography. The native oxide is removed using Hydrofluoric acid (HF), and silicon is etched using wet etching in developer solution which is a diluted solution of tetra methyl ammonium hydroxide (TMAH).Etching occurs at elevated temperature in case of dry etching "deep reactive ion etching" depending on the required structure anisotropically. Finally the oxide is totally stripped, and the glass wafer is bonded on the top of the microchannel to enclose it [33, 34]. (Cf. Figure 1.11)

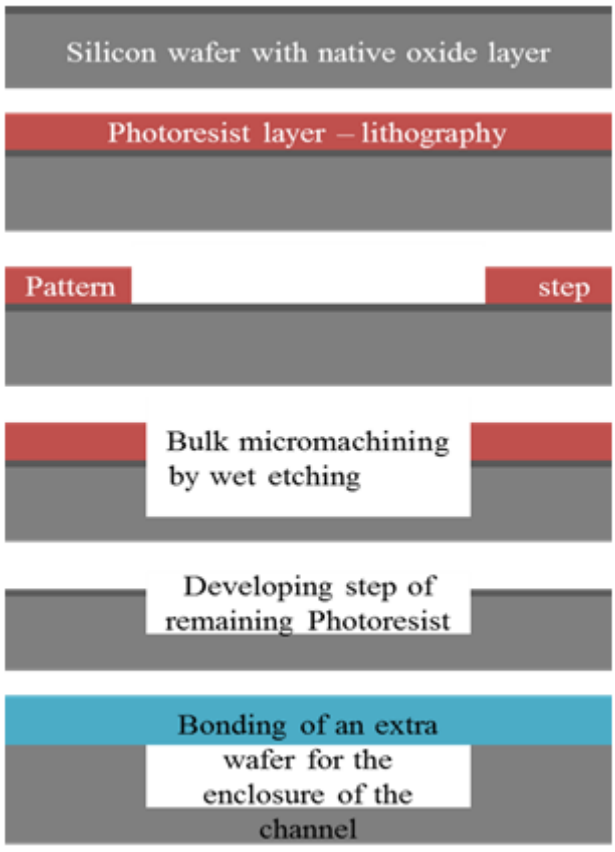

Figure 1.11 Process flow of wet anisotropic etching of microchannels (adapted from [33])

This technique has a number of disadvantages. If proper channel aspect ratio is maintained, the channel could collapse during wafer bonding. The collapsing of the channel depends on wafer thickness, stiffness, surface adhesion energy and on the geometry of the channels. This technique is also sensitive to contamination, also it is costly as it requires deep etching using RIE for vertical side walls, and an additional wafer is required for the bonding [27, 30].

1.3.1.2 Surface micromachined microchannels

As we have seen before in bulk micromachining of microchannels there is a need for an extra substrate to cover the microchannels, the microchannels are fabricated using several etching and lithographic steps which increase the complexity of the process and require high costs. In contrast the proposed surface micromachining approach for microchannels fabrication is done on a single substrate using sacrificial layer approach to obtain the channels [35].

Surface micromachining is the process in which a sacrificial layer is deposited between the substrate and the structural layer then detached from beneath the structure layer, leaving free standing structures (Cf.Figure 1.12) [35-37].

.

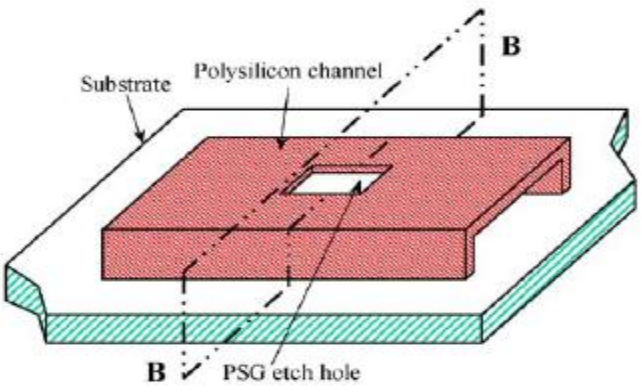

Figure 1.12 Side wall for the polysiliconmicrochannels [36]

The process flow of the polysiliconmicrochannels follows the following sequence: First a deposition and patterning of a polysilicon layer in order to obtain a higher height for the channel (Figure 1.13a). Next a phosphosilicate glass layer (PSG1) is deposited and it acts as a sacrificial layer, and it is patterned to obtain the microchannel body (Figure 1.13b). Afterwards, a deposition and patterning of a 2 μm thick polysilicon is made which is the structural layer of the microchannel (Figure 1.13c). In order to remove the PSG1 sacrificial layer, the structure is immersed in HF solution which attacks the PSG1 through the etch hole that are patterned in the top of the structural layer, finally the process is accomplished by rinsing and drying [34, 36, 38].

At this point it is important to note that the etching holes are not only essential for the removal of the sacrificial layer inside the microchannels but are also useful for taking away the air bubbles that usually block the microchannels during the fluid flow. The dimensions of the etch hole must be small enough so the surface tension of the liquid can still held the liquid inside otherwise the liquid won't be held inside the channel [36, 39].

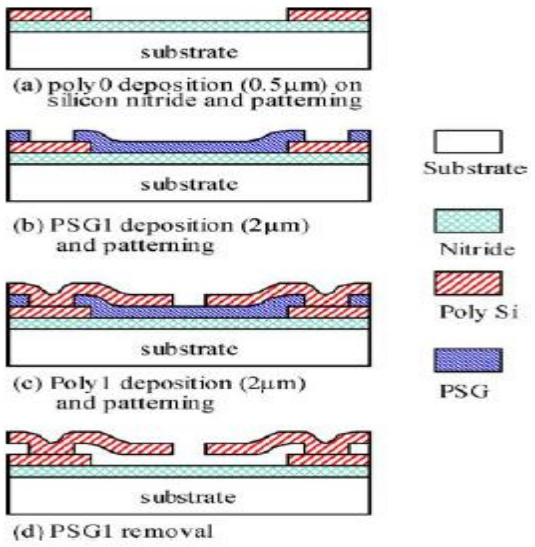

Figure 1.13 Process flow for polysiliconmicrochannels [36]

In spite of the limitation imposed by surface micromachining on the channel height, still it can be an interesting alternative solution instead of using bulk micromachining, thus eliminating the use of an extra wafer for the enclosure of the microchannel which is very costly.

1.3.1.3 Soft lithography

Recently with the development in MEMS fabrication techniques, there has been a trend to replace silicon and glass microchannels fabrication with polymers based microchannels. This is due to the complex fabrication processes and costs coupled with the conventional microfabrication process of silicon and glass. One of these new methods is the soft lithography in which conventional lithographic techniques are used to create a template in a thick film of photoresist, this is followed by filling this template with a curable polymer like polydimethylsiloxane (PDMS) and producing many replicas of the microchannels [39, 40].

Soft lithography can be considered as a two-step process; the first one is the fabrication of a master reusable template, in this step, a layer of thick photoresist like the negative photoresist SU8 is spun and patterned on a glass substrate, then the exposed photoresist is developed and the template is fabricated (Figure 1.14). In the next step PDMS is poured on the top of the template, and then it is degassed in a vacuum chamber. PDMS is then cured at 70°C for thirty minutes. After solidification, the PDMS is detached from the template. The last step is bonding. First, the cured PDMS is introduced to inductively coupled plasma (ICP) treatment under O_2 reactive gas. By this step the PDMS surface is treated and the adhesive forces between the PDMS and the glass substrate are increased so that a strong bonding occurs between them (Figure 1.14) [41-43].

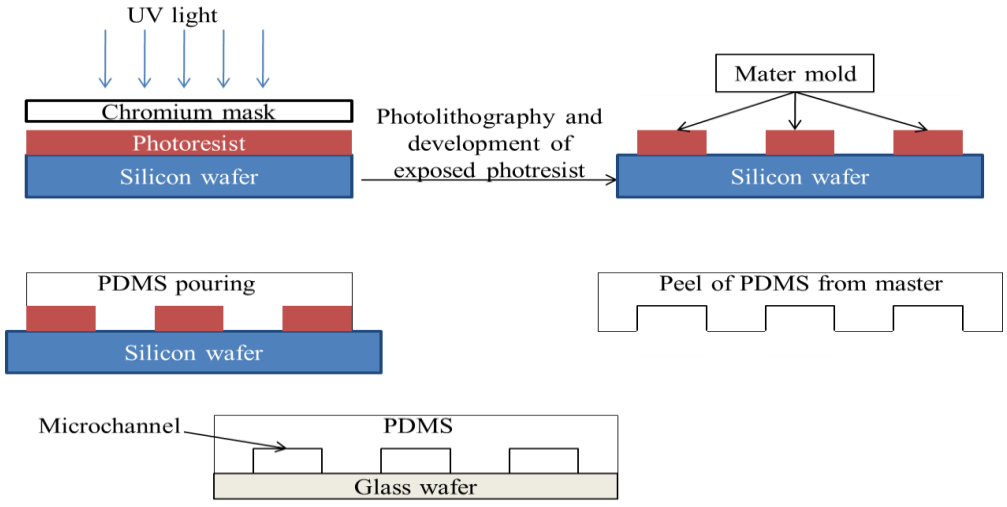

Figure 1.14 Process flow for PDMS based microchannels (adapted from [42])

In soft lithography there is no need for the complex processes used in conventional fabrication techniques used in silicon and glass processes. In addition PDMS is a very good material for microchannel fabrication, but the main problem in creating microchannels out of PDMS is that it is hydrophobic. This results in uncontrolled absorption on the microchannel walls, so the microchannels must be coated with another material to change its properties [41, 44, 45]. That is why a novel fabrication technique that relies on creating the microchannels body out of thick photoresist will be described in the following section.

1.3.1.4 Polymer based microchannels with an in-plane integrated microfluidic interconnects

In this approach instead of using PDMS to form the microchannels, the body of the microchannels is made out of SU-8 which is a thick negative photoresist. In addition, in this example a new approach that offers the integration of interconnects between the microchannels and the macro-world is given. In this design an SU-8 housing that contains the inlet and outlet of the microfluidic system is patterned and in between there is the microchannel (Figure 1.15). In this approach the integration of the interconnects rely on the plug-in format, in this case the "pin" is a non-coring needle while the "socket" is the PDMS septum that will be introduced into the SU-8 housing patterned at the inlet and outlet of the microchannels. With this design the microchannels can be reached easily by the outside world just by introducing the needle into the PDMS. The beauty of this process relies on its reusability due to the resealing of the PDMS when it is pierced by a non-coring needle [46, 47].

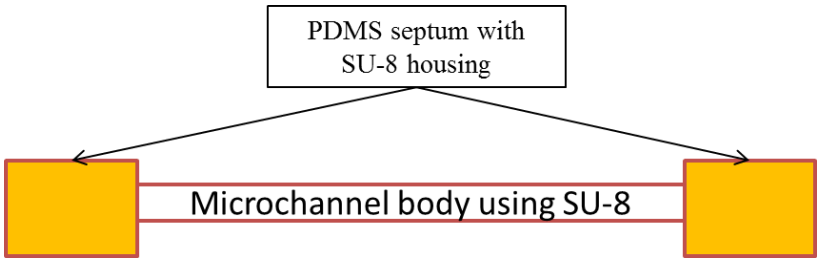

Figure 1.15 Illustration of Su-8 microchannels with PDMS septum (adapted from [47])

In this design, first the PDMS septum size and shape are defined by the pattern of theSU-8 housing which can be circular or rectangular. While for the thickness of the microchannel, it depends on the dimensions of the needle that will be used and also depends on the maximum thickness that can be achieved with the photoresist. So for example, if a 33 gauge needle which have an outer diameter of 203 μm is used, so in this case the thickness of the channels needed should be about 100-200 μm greater than the outer diameter of the needle so an SU-8 layer with 300μm thickness is required [48].

The SU-8 microchannels are fabricated on a glass substrate. A layer of ParyleneC is deposited in on top of the substrate before the spinning of the SU-8. It is very useful for the adhesion of SU-8 because it improve the thermal stress that induces the delamination of the SU-8. It was shown that SU-8 delamination occurs in 100% of the setups without the ParyleneC layer. And this is due to the dissimilarity of the coefficient of thermal expansion of the glass substrate and the SU-8 which result in the bad adhesion of the SU-8 on glass substrates. ParyleneC has a high percent elongation (200%), which allows the ParyleneC to absorb the stresses due to the thermal difference between the glass and SU-8 [47-49].

In table1.1 **Adhesion-Shear Analysis** between the SU-8 2000 (which is used in this process) with different kind of substrate is given, the analysis shows a poor adhesion of SU-8 on a glass substrate that is why there is a need for the paryleneC as an adhesion promoter [49].

Table 1.1: Adhesion shear analysis between SU-8 2000 and different kind of substrate [49]

Substrate	SU-8 2000 (MPa)
Si	53
SiN	43
GaAs	66
Ni	45
Au	29
Al/Cu (99/1)	23
Cu	38
Cu with Ap-300 adhesion promoter	56
Glass	**Poor**
Glass with HMDS prime	Poor
Glass/Al_2O_3 with Ap-300 adhesion promoter	92
Quartz	61

Next a 300 µm layer of SU-8 is spun, soft baked and then patterned by the conventional lithographic techniques to form the body of the microchannel and the housing for the PDMS septum. Then a post exposure baking step is made before the development of the SU8.

Afterward the area defining the septum is filled with the PDMS to create the PDMS interconnects. To specify the area filled with PDMS water mask is used to prevent the filling of the microchannels with the PDMS, and water is a good mask due to the hydrophobic properties of PDMS. Finally the entire system is enclosed within a glass substrate, and the needles are inserted in the PDMS forming a complete microfluididc system with integrated interconnects to the macro-world (Figure 1.16) [48, 49].

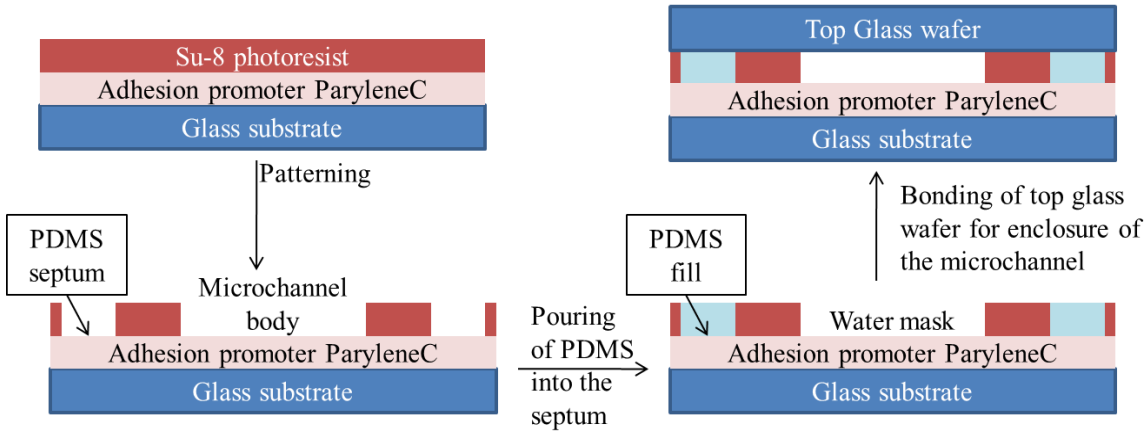

Figure 1.16 Process flow (adapted from [48])

The advantage of realizing microchannels using polymer based method is its low cost and less complexity as no etching, bonding or alignments steps are required. Additionally it solves the challenge of integrated micro-macro interconnects which in the conventional method requires good precision for alignments and require adhesives that may leak and interrupt the flow of the microchannels while in our case it is more easy and precise.

On the other hand, the major drawback of using SU-8 as the negative photoresist it is its poor adhesion to silicon and glass. Also it requires several processing steps which include a very long soft baking as well as a post exposure baking step which is time consuming. In addition, it is very hard to remove, and it needs specific solvents, therefore in chapter 2, the design and

fabrication of microfluidics microchannels with a new acrylic negative phtotoresist is proposed in this work to overcome the disadvantages of the SU-8 photoresist.

1.4 MEMS based microspectrometers

In this chapter an overview about different types of MEMS based spectrometers is given as a detector for the resulting optical signal. Optical MEMS is a class of Micro Electro-Mechanical Systems (MEMS) called MOEMS (micro Opto-electro mechanical systems) in which MEMS technology is integrated with micro optics to produce new class of optical systems for sensing (optical sensors) or manipulation of optical signals (optical mirrors or switches). The integration of micro optics with MEMS technology provides it with the advantage of micro-technology such as small size, precision, lower cost. It can be used in a variety of applications like sensors, actuators, as well as for environmental and biological applications which require portable system (lab-on-a-chip) to achieve the small sample size, fast reaction, portability and lower cost as the reactions take place on site so there is no need for transportation or complex sample preparation. MOEMS is a promising technology for various applications that cannot be achieved using either technology alone and recently it is playing an important role in a variety of applications. Optical MEMS is a field which has wide range of applications that emerged with the development of MEMS technology. Optical MEMS sensors could be used in whether environmental or biological applications. This visual detection is very useful as it requires only simple techniques that have few preparation steps and do not involve complex systems [50, 51].

One of the most important devices in MEMS optical sensors are microspectrometers. Microspectrometer is a tool designed to measure the spectrum of microscopic areas or microscopic samples. It can be configured to measure the transmittance, absorbance, reflectance, polarization and fluorescence of sample areas smaller than a micron [51, 52].

Basically microspectrometers are composed of the following components [53]:

• Input slit for spatial sampling of the radiation
• Collimating lens for the collimation of the light beam
• Dispersive element
• Focusing lens that produces image of the input slit in the plane of the sensor with the position of the image depending on the wavelength.
• Detector at the output or array of detectors depending on the dispersive element used. (See Figure 1.17)

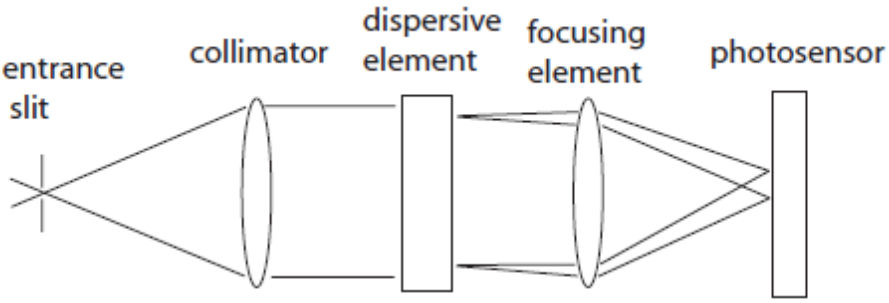

Figure 1.17 Simplified schematic of general microspectrometer device[54]

The fabrication of microspectrometers is based on silicon using MEMS technologies that gives us many advantages: small size, lightweight, and showing a demonstrated capability for spectral analysis. The fabrication using silicon process with compatible technologies, allow the integration of a complete optoelectronic system-on-a-chip. This is achieved by the integration of micro-optics components needed with microelectronic circuits. However, what is challenging in these devices is the improvement of spectral resolution to achieve high resolution and accuracy, due to the dependence of the resolution on the optical path. This limits the maximum resolution obtained by these miniature devices due to its small size which makes the path shorter. Also optical properties of silicon IC-process compatible materials and lack of adequate optical signal

conditioning could make the restriction on the maximum resolution. Microspectrometers can be operating in visible and infrared spectral range depending on the applications [59, 60].

From the principal components that differentiate the type of microspectrometers is the dispersive element used. The classification of the different types of microspectrometer is determined by the dispersion element or approach used and this involve microspectrometers based on (a) prisms, (b) gratings and (c) interferometers. Prism-based microspectrometers are not suitable for miniaturization and are not considered in this case [55, 56].

1.4.1 Grating-based microspectrometers

Grating-based microspectrometers principle is based on incident light that interferes at the grating causing dispersion. A grating based spectrometer system is shown in Figure 1.18.First the input beam is incident through a narrow entrance slit, which transforms it into a parallel beam by the use of a collimating lens or mirror. Afterwards the beam is dispersed at the grating and the dispersed spectrum is injected on the exit slit using a focusing lens or mirror. The spectrum is scanned across the exit slit either by rotating the mirror or the grating itself. Grating-based microspectrometers can be designed to work either in the visible range or at near-infrared part of the spectrum using microfabrication techniques. In these types of microspectrometers the limitation relies on the use of a transmission grating and the omission of optical signal conditioning [57-59].

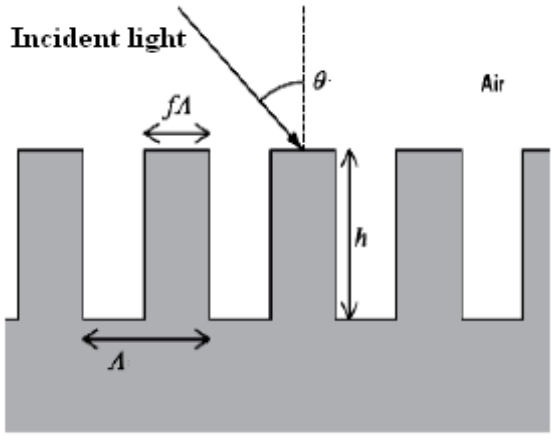

Figure 1.18 Diffraction grating structure[60]

Another case is the use of diffraction grating as dispersive elements in the microspectrometers (Figure 1.19). Essentially, a diffraction grating carries out a Fourier Transform, which makes the separation of a waveform in the time domain into a number of waveforms in the frequency domain; the refraction of light is done by variable amount varying according to the wavelength of the incident beam. It is formed of periodic spaced set of grooves etched in a mirror surface of a solid material [58, 61, 62].

The spectral resolution in a grating-based spectrometer, R, when using the first-order diffraction spectrum, is related to the number of slits, N, in the grating according to the relation: R=N.

The use of diffraction gratings as a dispersive element in microspectrometers makes the system simple. However there are some disadvantages, such as little light transmission, lower efficiency and spectrum overlapping. Additionally in grating based microspectrometer we need to use a detector for each wavelength which increase the costs and complexity [57, 62].

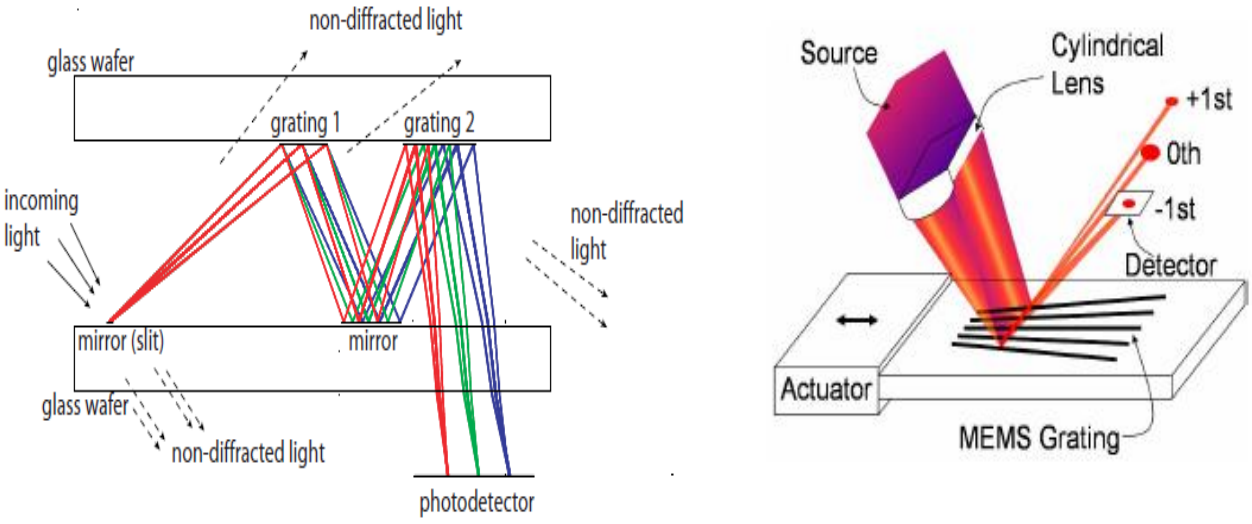

Figure 1.19 a) An example of double planner grating b) scanning diffraction grating spectrometer[54, 58]

1.4.2 Interferometer based microspectrometers

Interferometer based microspectrometer uses Fourier transform operation. Fourier transform is accomplished by computing an interference signal which contains data about the whole spectrum of the light [63, 64].

The Interferometer operation is based on the division of incident light beam into two parts that interfere together after going through two different optical paths. There are many types of interferometer based microspectrometer [50, 65, 66], they can be classified as:

a) Michelson interferometer

b) Fabry Perot interferometer

c) Laminar grating interferometer

a) Michelson interferometer

One of the most commonly used interferometer based microspectrometer is the Michelson interferometer in which the incident light is divided into two parts that interfere together after going through two different optical paths with a well-defined difference in length. The optical path length difference varies according to the wavelength which is an effective approach for the selection of a spectral component. Varying the optical path length in time allows the scan of a complete spectral part of the spectrum. The Michelson interferometer principle is based on the use of a beam splitter and two mirrors (M1 and M2) to define the two optical paths (Figure 1.20). The path difference between the splitter and the mirrors defines the optical path length difference. Measuring the path length increase between the positions of two maxima or minima of the interference pattern detected by displacing one of the mirrors in the direction of the optical axis provides the measured wavelength of the incident light [67, 68].

The integration of the beam splitter in MEMS based microspectrometer is very difficult which makes an important challenge and limitation in Michelson interferometer based

microspectrometer. That's why Fabry-Perot interferometer were introduced and has received lots of attention to eliminate the beam splitter used in Michelson interferometer [69, 70].

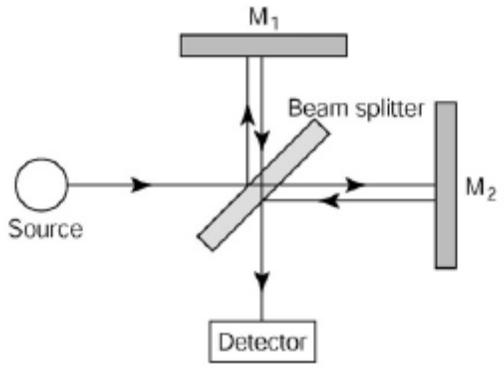

Figure 1.20 Michelson interferometer [50]

b) Fabry-Perot interferometer

Basically Fabry-Perot interferometers are constituted of two parallel mirrors with the reflecting part facing each other separated by a distance "*d*" that defines the wavelengths of light passing through the structure (Figure 1.21). In order to vary the range of wavelengths that are passing through the structure, this can be done by changing the refractive index between the two mirrors or by making one of the mirrors movable to change the separation "d" between the two mirrors, which is most commonly using MEMS based electrostatic actuator. These two mirrors with the distance separating them are forming a resonance cavity that captures standing waves of different modes. Incident beam is transmitted through this cavity and after making multiple reflections between the two mirrors M1 and M2 the beam is transmitted to the detector. Constructive interference is only obtained for wavelengths that are fitting with the resonance cavity [39- 44].

Resonance is obtained when $2nd = m\lambda_0$, where m is an integer, λ_0 is the wavelength, "d" the distance separating the two mirrors and n the refractive index [70-72].

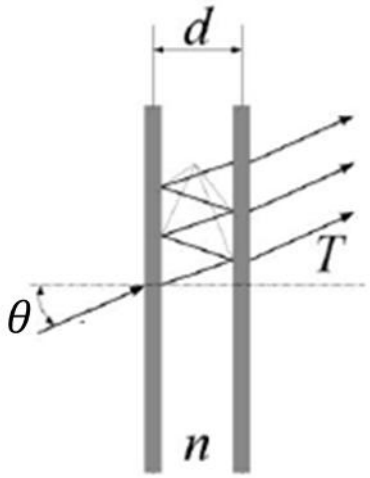

Figure 1.21 Fabry Perot Filter[65]

One of the important factors that affect the transmission of the Fabry-Perot interferometer is the reflectivity of the mirrors. If the reflectivity is low this results in a broadening in the transmission picks while if the mirrors have high reflectivity this will result in sharp transmission peaks. In the Fabry Perot interferometer this factor is describe by the *"Finesse"* which describes the capability of the interferometer to detect slightly close spectral line, in other words its ability to distinguish slightly different wavelengths which result in a higher resolution interferometer. The finesse "*F"*, in case of two perfectly parallel mirrors finesse is given by [73]:

$$F = \frac{\pi\sqrt{r}}{(1-r)} \qquad 1.1$$

Where r describes the reflectivity of the mirror.

The spectral resolution of the resonator depends on the gap between the two mirrors and the wavelengths that are passing through it, and it is given by [53]:

$$\Delta\lambda = \frac{\lambda^2}{2nd\cos\theta} \qquad 1.2$$

Where Δ λ is the spectral resolution the interferometer, λ the wavelength, *d* is the distance separating the two mirrors and *n* the refractive index.

From Eq.(1.1) and (1.2), it can be deduced that the spectral selectivity "*F*" of a Fabry-Perot interferometer is dependent on the reflectivity of the mirrors and the separation between the two mirrors while the spectral resolution "Δλ" is directly proportional to the passing wavelengths and inversely proportional to the separation "d" between the two mirrors, which means that in order to have a high resolution, a narrow spectrum is required together with a larger separation between the two mirrors [74, 75].

First Fabry–Perot interferometers for visible range were made using bulk micromachining on two wafers, followed by wafer-to-wafer bonding (cf. Figure 1.22). Silver is used for the mirrors due to its high reflectivity in this visible range. The working wavelengths are specified by the separation between the two mirrors. To control this separation between the mirrors, electrostatic actuation is used by applying an appropriate voltage between the electrodes to tune the resonance cavity to achieve the wavelength desired.

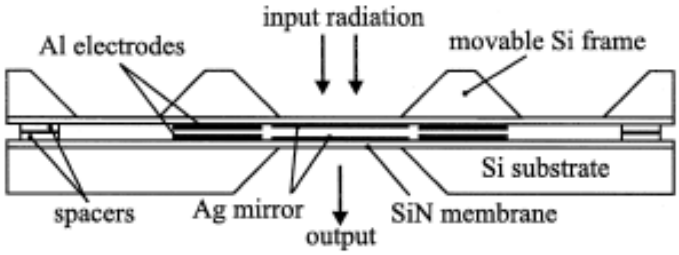

Figure 1.22 Cross section of Fabry Perot interferometer design using bulk micromachining[53]

The main problem in this case that a high amount of voltage is needed to achieve high tuning over a large spectral range however the electrostatic actuation is limited by the pull in of the comb-drive. An alternate approach to overcome this problem is to make sixteen fixed cavity

covering the visible spectrum. However, the disadvantage in this case is that the incident beam is split over the array before dispersion. Accordingly, each cavity will receive a small amount of power thus reducing the efficiency [76].

The other challenges that still affect the Fabry-Perot interferometer efficiency that it needs high precaution in fabricating mirrors with high reflectivity and flatness which will result in a narrower peak, and hence increases the resolution. In addition, the two mirrors should be perfectly parallel to each other. Furthermore, in the visible and ultraviolet range, the optical layer of the interferometer need to be very thin, which cannot be achieved by the conventional fabrication techniques. Accordingly, Atomic Layer Deposition (ALD) technology might be essential as it allows the deposition of very thin layer with precise control as well as the possibility for low processing temperatures [72, 74].

In order to overcome the disadvantages of the microspectrometer based interferometers, a novel approach based on out of plane comb-drive has been proposed. This is referred to as lamellar grating microspectrometer, and is explained in detail in the next section.

c) Lamellar grating based microspectrometer

Fourier transform microspectrometers can be realized in a more compact and robust way using lamellar grating interferometer (LGI) in which movable diffraction grating operating in the zeroth order are used. The idea of lamellar grating interferometer has been known long time ago, however limitation in the fabrication technology has stopped its development. However, recent improvements and development of the microfabrication technologies made it feasible to use LGI as it allows the fabrication of diffraction gratings with high precision, and it ensures its high speed movement in a pure translational mode using simple actuation techniques [77, 78].

Lamellar grating interferometer can be described as a binary grating with a movable depth, taking the zeroth order of the diffraction pattern (Figure 1.23). The first to design this kind of interferometer was Strong and Vanasse in 1960 [79]. A lamellar grating interferometer is a type of Fourier microspectrometer. In Michelson interferometer it is the wave amplitudes that is divided at the beam splitter, whereas in lamellar grating interferometer it is the wave front that are divided. The wave fronts are divided in a way that the incident beam is split into two halves between the front facets (fixed mirrors) and back facets (movable mirrors) (cf. Figure 1.24). The variable depth between the two mirrors defines the optical path difference traveled by the two parts of the wave. The interference is obtained by making the incident beam interacting with a spatially delayed form of itself by the variation of the distance between the two facets of the grating.

Most commonly this kind of microspectrometer was used for wavelengths greater than 100μm because below this range the tolerances are too tight for most machine shops. Recently the improvement in silicon micromachining technology has helped to overcome these restrictions for shorter wavelengths. The core of the microspectrometer design is based on two sets of electrostatic comb drives that act at the same time as an actuator and a variable-depth diffraction grating (Figure 1.25). The microspectrometer is fabricated using micromachining technology on a silicon-on-insulator (SOI) wafer, which is a CMOS compatible process [80]

The main improvements of the Lamellar Grating Interferometer design over the Michelson interferometer are the removal of the beam splitter and reference mirror, which results in a more robust, compact and lower cost system. Additionally all the micro-optics used in the design are reflective (Figure 1.26), which results in a large operating spectral range which is only limited by the type of detector used [77, 78].

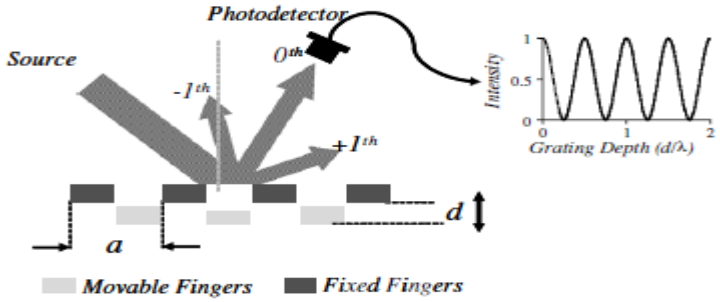

Figure 1.23 The idea of LGI is based on modulating the zeroth order which is recorded in function of the depth d introduced[81]

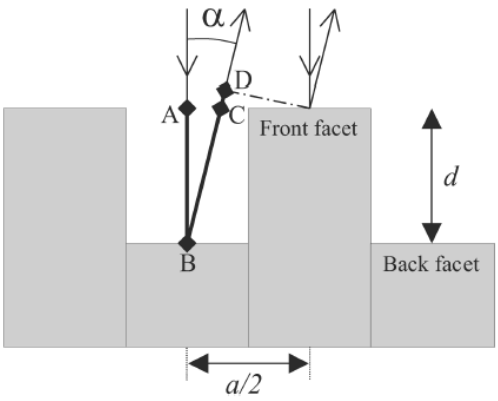

Figure 1.24 Division of the incident beam between the front facets and back facets [79]

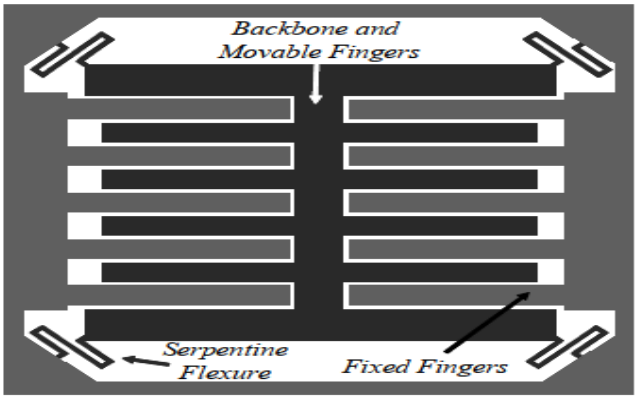

Figure 1.25 The main Structure of the LGI "Electrostatic Comb Drive" [79]

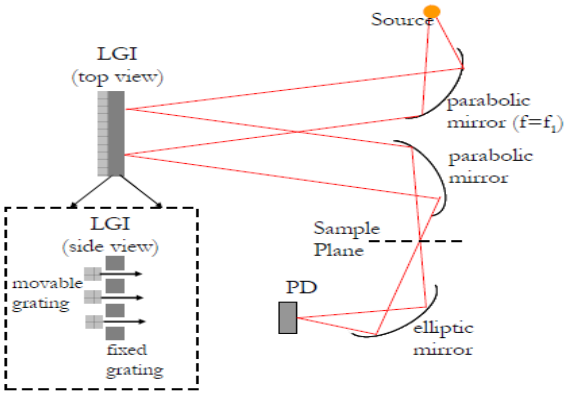

Figure 1.26 LGI structure with the reflective micro-optics and the output detector [82]

Generally the operation range of a Fourier transform microspectrometer can be expressed by the working spectral range of wavelengths such as [λ_{min} - λ_{max}] and it can be also defined by the wavenumber $k = 1/\lambda$ as [$k_{max} - k_{min}$]. The collimation of the incident beam and the optical path difference 'd' between the two traveled beam are essential factors affecting the spectral resolution of the microspectrometer. Let's assume that the incident beam is coming from a perfectly collimated point source, in this case the spectral resolution can be described by the common equation [82]

$$\Delta K = \frac{1}{OPD} = \frac{1}{2d} \qquad 1.3$$

Where ΔK is the spectral resolution, OPD is the Optical Path Difference traveled between the two halves of the incident beam, 'd' is the maximum distance achieved by the moving part of the structure.

In case that the input source is not perfectly collimated, the difference in optical path, after the collimating mirror, is given by:

$$\Delta OPD = \left| 2d\left(1 - \frac{1}{\cos\theta_d}\right) \right| \qquad 1.4$$

Where θ_d is the half divergence angle, which measures the collimation of the incident beam. The half divergence angle θ_d is dependent on the source size "aperture size" (D_s) and the focal length of the first collimating mirror (f_l), and it can be defined by:

$$\theta_d = \tan\left(\frac{D_s}{f_l}\right) \tag{1.5}$$

In order to achieve better results, there are some restrictions on the maximum value for the divergence angle, as destructive interference occurs when the OPD is $\lambda/2$, and by using small angle approximation so that $\cos\theta_d = 1 - \frac{\theta_d^2}{2}$. This leads to the following restriction on the half divergence angle that results in better spectral resolution [81, 82]:

$$\theta_d = \sqrt{\frac{\lambda_{\min}}{2d}} = \sqrt{\frac{\Delta k}{k}} \tag{1.6}$$

All the previous criteria can be applied to all types of Fourier transform microspectrometer, however there are some limitations that are specific to the lamellar grating microspectrometers and are mainly related to the construction of diffraction orders. The lamellar grating interferometer is considered as a diffraction grating with variable depth. In this type of gratings diffraction orders are detected at integer multiples of λ/Λ where Λ is the grating period. In order to ensure the separation between the orders, specifically the zeroth and first order, as the LGI deals with the zeroth order, the subsequent condition must be ensured to have good separation between orders:

$$\sin(2\theta_d) \leq \frac{\lambda_{\min}}{\Lambda} \tag{1.7}$$

Another factor that must be taken into consideration in LGI is the "Talbot images". This happens when a periodic pattern is illuminated (square-wave amplitude grating in this case) approximate images of the grating occur at integer multiple spacing called Talbot distance, which is given by [87]:

$$T = \frac{2\Lambda^2}{\lambda} \tag{1.8}$$

Where *T* is the Talbot distance.

Phase reversed images occur in distances between two successive Talbot images. At these positions the energy transmitted from the front facet escapes between the finger of the back facet and small amount of energy is reflected back from the back facet which result in a very low contrast in fringes and interference that is why Talbot phase reversal should be avoided. Talbot phase reversal occurs at half of the Talbot distance, which adds limitation on the maximum optical path difference traveled by the interferometer. In order to avoid Talbot phase reversal, the maximum displacement *'d'* should not exceed *T/2* in this case new criteria has to be considered in designing the grating period, such that [83]:

$$\Lambda > \sqrt{\lambda_{\max} d} = \sqrt{\frac{\lambda_{\max}}{2\Delta k}} \tag{1.9}$$

The operating principle of the lamellar grating interferometer is the same as that of Michelson interferometer. However instead of dividing the incident beam using beam splitter the splitting is performed by the diffraction grating. The grating is defining a rectangular phase profile to the incident wavefront. This is due to the difference in phase between the two wavefronts reflected back from the front and bottom facet of the grating. If the intensity profile is taken just after the grating, the intensity profile will be similar to the grating. However, if a far field diffraction pattern is considered, the profile will have the shape of Fourier transform diffraction grating. If a Fourier transform procedure is applied to the output signal, this will provide the wavelength of the incident light, and it has to be noted that the dc component of the Fourier transform doesn't bring any data about the incident beam. Hence, the resulting spectrum is independent on the dc component, and accordingly this principal can be used for spectral analysis of broad band sources [88].

Comb drive actuators can be the best choice for the lamellar grating interferometer, because the periodic structure of the comb fingers makes them usable as a variable depth diffraction grating. In case of using an out of plane comb drive in resonant mode, the intensity profile, I_{center}, detected by a detector positioned at the center of the diffraction pattern can be given by [84]:

$$I_{center} = A\cos^2\left(\frac{4\pi d_{\max}\cos 2\pi f_{res} t}{\lambda}\right) \qquad 1.10$$

Where, f_{res} is the resonant frequency of the comb drive, A is the amplitude, d_{max} is the maximum displacement. In Eq. (1.10) the center of the diffraction pattern should be sinusoidally modulated with respect to the optical path difference traveled by the grating. Consequently, when the fingers of the comb drive are moving at resonance, the intensity profile detected by the single detector at the central position of diffraction with respect to the grating depth will be modulated with a raised cosine function [84].

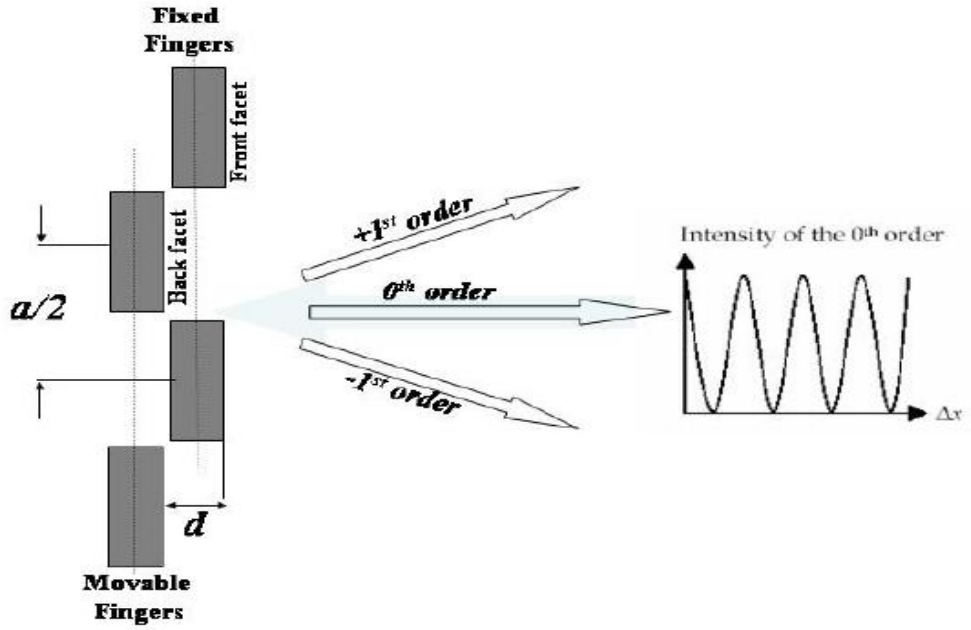

Figure 1.27 Intensity profile versus the grating depth [66]

The spectral resolution of the lamellar grating interferometer is affected by the wavelength, and it is basically restricted by the Fourier transform process. The intensity profile versus the optical path difference using monochromatic source is shown in Figure 1.27. The spectral resolution is given by [66, 85]:

$$\frac{\Delta f}{f} = \frac{\Delta \lambda}{\lambda} = 0.17 \frac{\lambda}{d_{\max}} \qquad 1.11$$

Where f and λ are respectively the frequency and the wavelength of the source. $\Delta f, \Delta \lambda$a are the minimum resolvable band-width and line-width of the interferometer, respectively.

Eq. (1.11) indicates that the resolution depends on the maximum displacement achieved. As the spectral resolution is inversely proportional to the maximum displacement reached, so it would be better to work at resonance as this will result in a higher displacement with lower driving voltage. Additionally hundreds of interferograms will be achieved in one second, which decrease the measurement time. On the other hand, this is challenging with regards to the generated interferograms [85].

As a conclusion, lamellar grating interferometer is a Fourier transform based microspectrometer. Its basic principle is simple and results in a more compact, low cost interferometer, and it can be easily integrated to obtain a complete system using single photodetector depending on the working wavelength. The design can achieve high displacement up to hundreds of micrometer which improves the resolution to be about 0.5 nm in the visible range and 5 nm in the infra-red region. There is still some study to be taken to achieve higher improvements. This type of interferometer has many advantages over the previous ones, in term of complexity, resolution, fabrication process, it can be fully integrated and it can be used over a wide spectral range only by changing the detector used.

In the next chapter a brief introduction about the mechanical modeling will be given with simulation results and a parametric study to see the effect of the design parameters on the performance of the interferometer in terms of resolution.

1.5 Thesis outline

Chapter 2 includes the design and microfabrication of a polymer based microchannels. Chapter 3 presents the verification, stability analysis and optimization of lamellar grating microspectrometers, followed by introducing a new idea for beam splitting for interferometer based microspectrometer.

2 Chapter II Fabrication of microfluidics microchannel

In this chapter, the fabrication of microfluidic microchannels is conducted as it is the most important component of microfluidic platform. In the first section of the chapter, a theoretical analysis for the design of the microchannels are given, followed by a Finite Element Method simulation using Comsol multiphysics to verify the behavior of the flow inside the channels. Afterward the process flow of the fabrication of microchannels using a new acrylic negative photoresist *AZ 125 nxt* with SEM results for the fabricated channels is included.

2.1 Fluidic analysis

In order to study the behavior of the microchannels to be used in various microfluidic applications such as fluid separation, mixing, the fluid flow and pressure drop along the microchannels are important parameters to be studied. In this context the following section includes a first order analysis model to study the pressure drop along the microchannels, afterward the results are verified by comparing them to a model conducted using Comsol.

2.1.1 Theoretical calculations

To simplify the analysis, the following model is used in the theoretical calculations and simulation. The approximation used in this model is based on the assumption that the inlet and outlet of the microchannels are considered as a square microchannel with the same width and length of 500 μm. The length of the microchannel body is chosen to be 8.8 mm, the thickness of the structure is 300 μm (Figure 2.1). In order to calculate the pressure drop along the length of the channel, Hagen-Poiseuille equation is used, and it is expressed as [86]:

$$p = RQ = \frac{128\mu L}{\pi D_{eff}^{4}} Q \qquad 2.1$$

Where R is the resistance of the fluid in Kg/m^{4}s, Q is the flow rate in m^3/s, is the viscosity of the liquid. It can be assumed to be water with (μ= 0.00103 Kg/ms), D_{eff} is the hydraulic effective diameter in *m*, and it can be described by:

$$D_{eff} = \frac{64}{k}\frac{2wh}{w+h} \qquad 2.2$$

Where k is the correction factor (fR_e), w is the width of the channel, and h is the height of the microchannel.

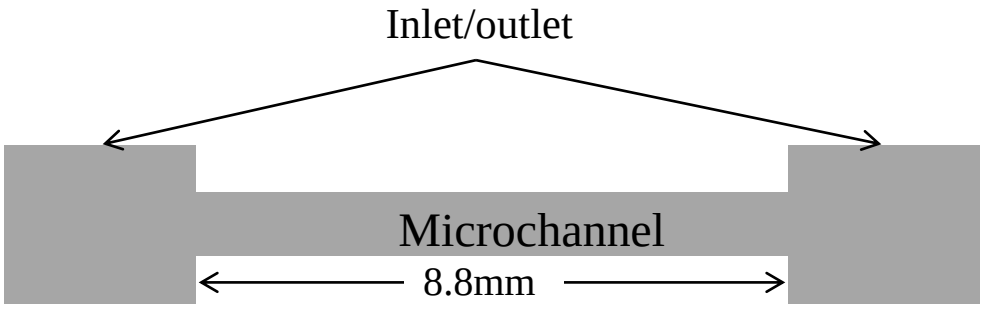

Figure 2.1 Microchannels design

In the following part two microchannels with different widths 300 µm and 400 µm are studied in order to observe the effect of the channel width on the fluid flow and the pressure drop along the microchannel.

2.1.2 Simulation results

Simulations are done using Finite Element Method (FEM) using Comsol Multiphysics simulator. Finite element method (FEM) is based on numerical approach to solve partial differential equations (PDE) or integral equations. It has been conducted on many physical problems. The approach is based on reducing the partial differential equations into a number of linear equations. In FEM, the structure is divided into a set of finite elements then the analyses are conducted [87]. Comsol Multiphysics is simulation software for finite element analysis for many physical and engineering applications. It is very useful for coupled phenomena, and

multiphysics. It contains well defined interface to MATLAB and it has many modules for different applications.

Figure 2.2 shows the simulation results of the pressure drop for a 300 µm microchannel width, followed by a comparison of the pressure drop versus the flow rate of the fluids resulting from the theoretical calculations and the simulations which verify the theoretical analysis.

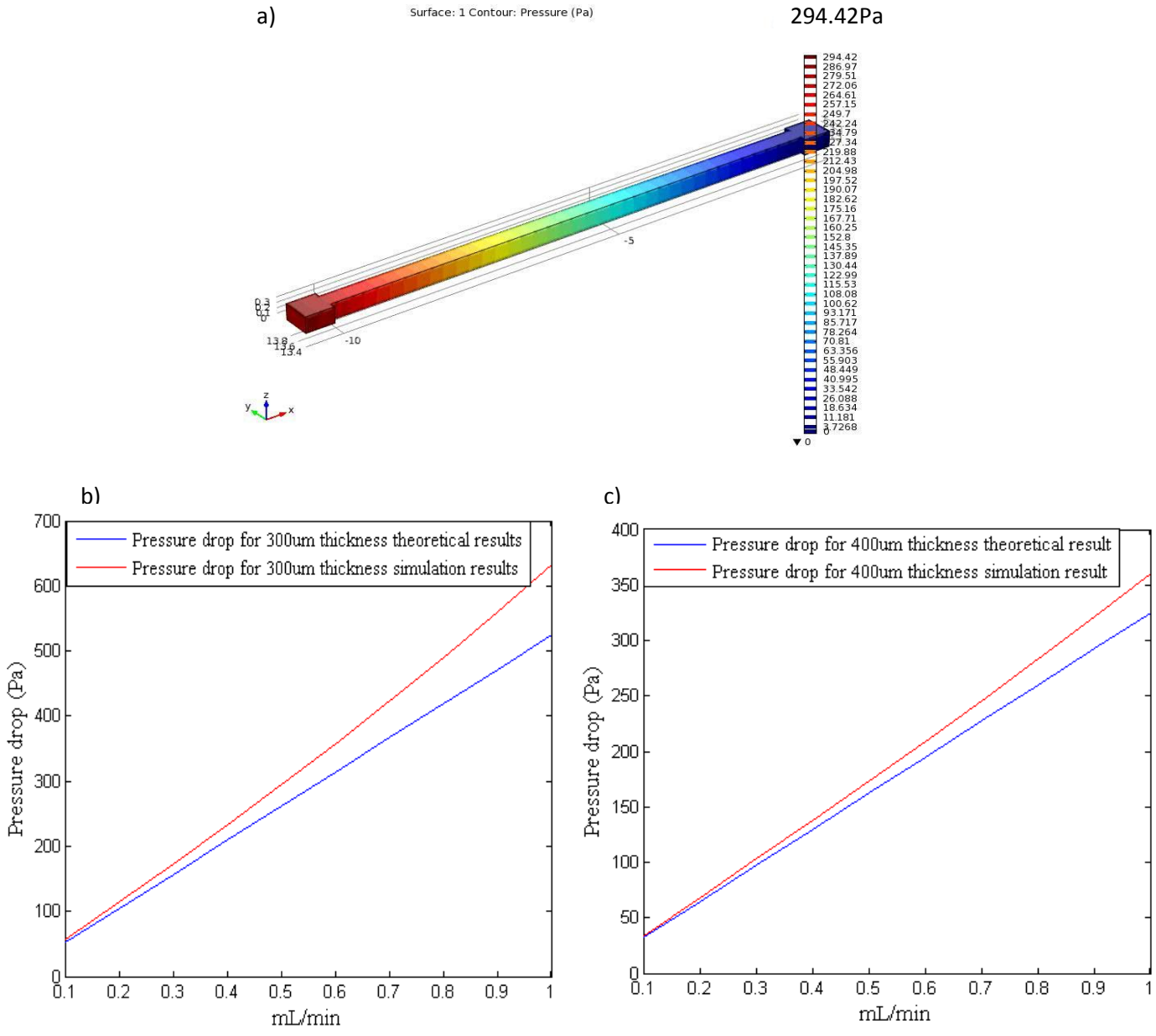

Figure 2.2 a) Pressure drop in 300 µm microchannel b) Pressure drop versus flow rate for 300 µm microchannels theoretical and simulation results c) pressure drop versus flow rate for 400 µm microchannels theoretical and simulation results

For the use of the microfluidic platform in the sensing and detection of heavy metals separation and the mixing of the fluid with various specific indicators for the detection is required. The use of multiple branches of microchannels from the main inlet is useful in order to allow the integration of specific indicator in each branch to enhance the sensitivity to a unique type of heavy metal ion. Figure 2.3 shows the simulation of multi-branch microchannels which allow the division of the input sample into multiple branches thus the handling of each one independently to meet the requirements of detecting each heavy metal ion specifically.

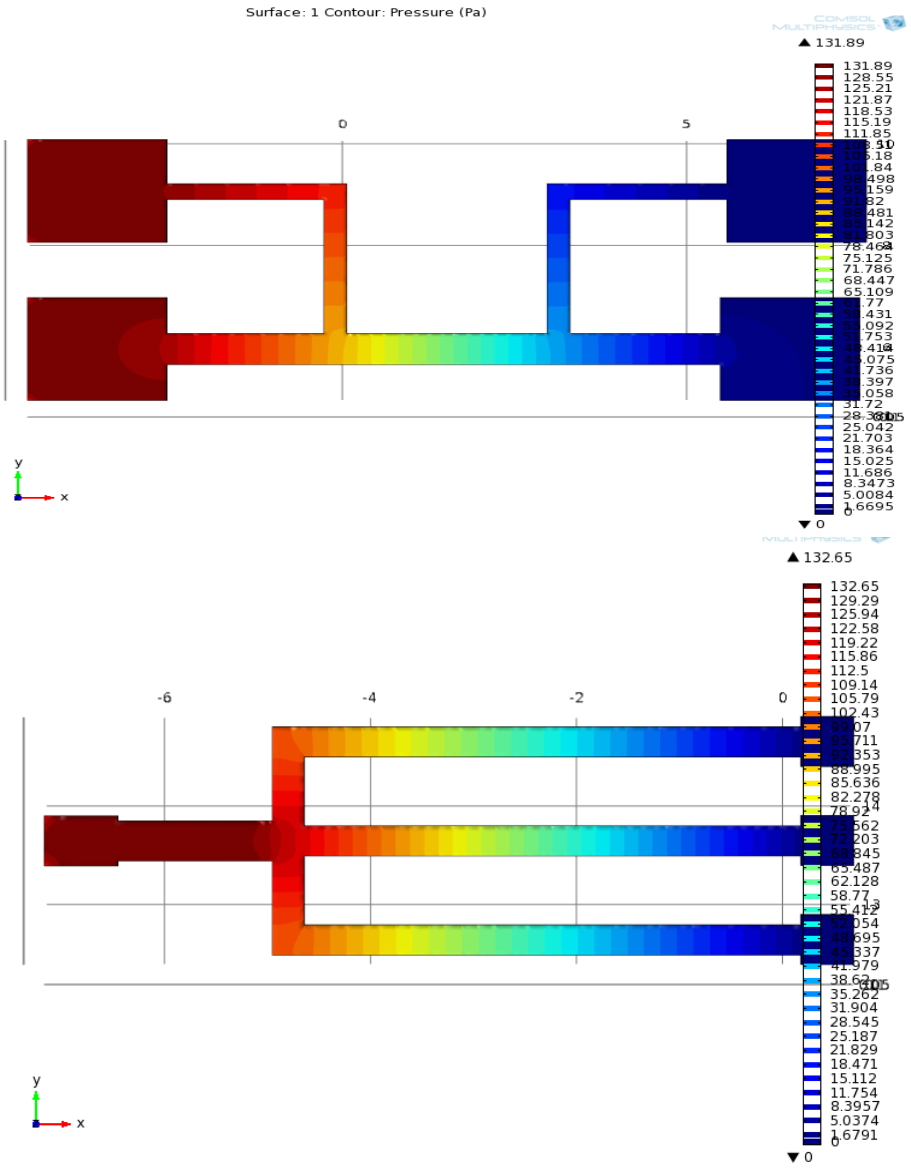

Figure 2.3 Simulation results of a) two inlets microchennel b) multi-branches microchannels

2.2 Fabrication process

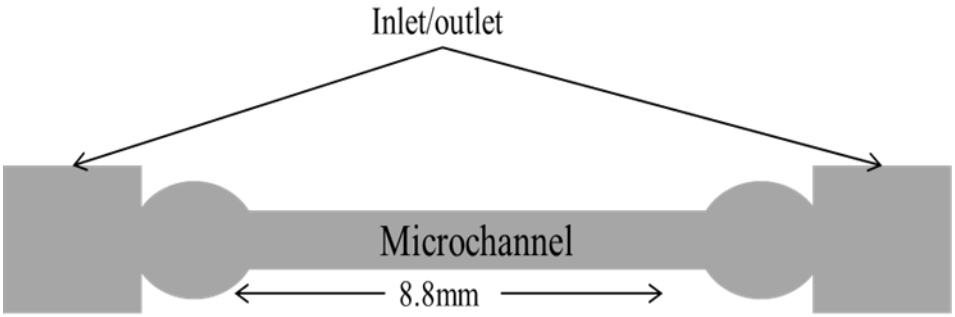

Figure 2.4 Microchannel design

For the design of this structure we have the microchannels with circular inlet and outlet and at their terminals there is a rectangular guide for the needles insertion. In this case we have in-plane integration of the needles which make the design more robust, the needles are then fixed into the structure using an epoxy for testing (Figure 2.4). For the microchannel thickness as the needles are inserted in-plane so the thickness of the channels are designed according to the needle diameter. In our case a 30 gauge needles are used which is about 300μm. So the microchannels thickness is about 350 μm to 400 μm. In this process the body of the microchannels is fabricated out of a new acrylic negative photoresist AZ 125 nxt which offers many advantages compared to SU-8 like good adhesion to silicon and glass substrates, it has a simple and rapid processing, and it can be easily removed using wet solvents like dimethyl sulfoxide or acetone or dry stripping using plasma with reactive radicals. Film thicknesses of 400, 800, and 1400 μm with an aspect ratio of 20: 1 have been achieved with this photoresist.

2.2.1 Fabrication process

The microchannels are made on a silicon wafer using AZ 125 nxt *negative* photoresist as the body of the microchannels (Figure 2.5). The photoresist spinning is done directly on the silicon wafers as it has a good adhesion with silicon. In order to determine the suitable conditions for the photoresist spinning to achieve the required thickness, Figure 2.6 shows a chart of the film thickness versus the spinning speed given by the company. The given conditions are used as a guide in order to reach the right recipe. This includes several trials to adjust the acceleration, the speed of the spinning and also the soft baking time and temperature. In order to produce robust film ready for exposure and patterning without sticking which can destroy the whole process and the mask used also. Afterward exposure and patterning are done and finally the wafer is developed. After having the microchannels structures on the silicon wafer, a glass wafer is bonded to the patterned wafer to enclose the microchannels (Figure 2.9). Finally dicing is done and the needles are inserted laterally into the microchannels.

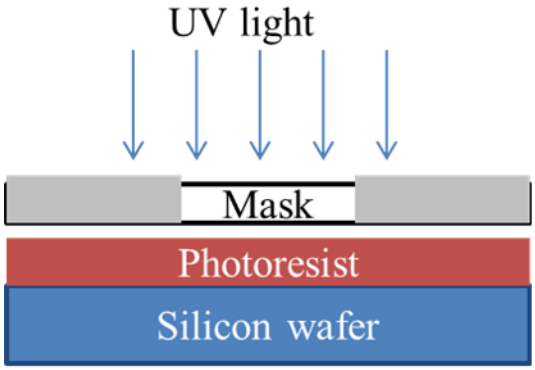

Figure 2.5 In negative photoresist the exposed area become insoluble

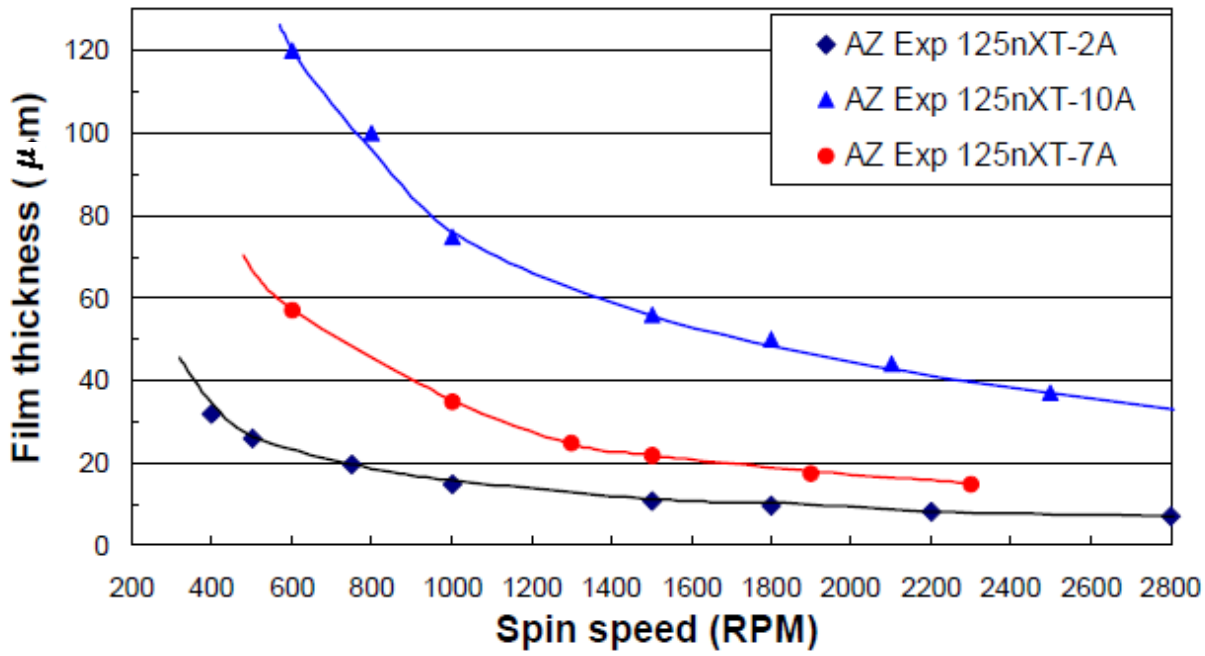

Figure 2.6 Film thickness versus the spinning speed

2.2.2 Procedure

1- Enough amount of photoresist is spun on the silicon wafer directly

2- Spin coating with speed 1100 rpm for 1.2 sec, then at a speed of 630rpm for 12sec (adjusting the acceleration to be 800rpm/sec)

3- After the coating, the photoresist film includes a residual of solvent concentration depending on the type of photoresist used and the thickness of the film. Accordingly, a soft baking step is required to decrease the remaining of the solvent available which increase the adhesion to the photoresist layer to the substrate and increase its hardening in order to prevent the sticking to the mask resulting in its contamination. The soft baking of the photoresist is done for 60 minutes at 135^{o}C temperature

4- After the soft bake, the wafer is left to cool down for 15min in order to ensure the hardening of the photoresist film and avoid the sticking to the mask during exposure

5- Exposure of the photoresist layer to the appropriate mask for patterning. The exposure is done for 340s.

6- Developing using AZ 826 MIF developer for 2-3 minutes in order to have a well-developed structure. This step is very sensitive and requires high precaution as we don't want to get an underdeveloped structure or overdeveloped one as in both cases the structure is affected

7- The resulting thickness is measured using the "decktak" and it is about 150 μm to 170 μm thickness

8- The same procedure is repeated on a glass wafer in order to bond it on the top of the silicon wafer containing the microchannels in order to get enclosed microchannels with thickness about 300 μm.

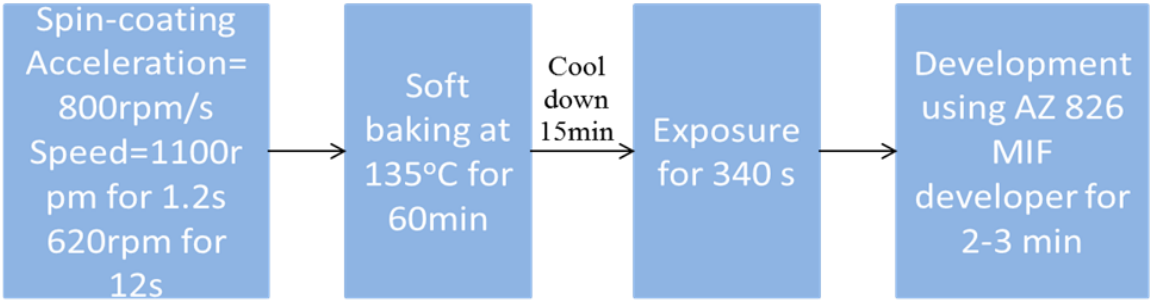

Figure 2.7 Procedure diagram for the photoresist fabrication steps

An important thing to note that in the process flow for the photoresist patterning no post exposure bake step is required (Figure 2.7). This is an intermediate step after the exposure and before development that is usually done to complete the cross linking initiating during the exposure and to harden the resist film before using it in other processes. This is a good advantage offered by the AZ125-nxt phtotoresist which decreases the time consumed and the steps required in the process flow.

Figure 2.8 shows an example of the mask used during the fabrication process of the microchannels of the patterning step

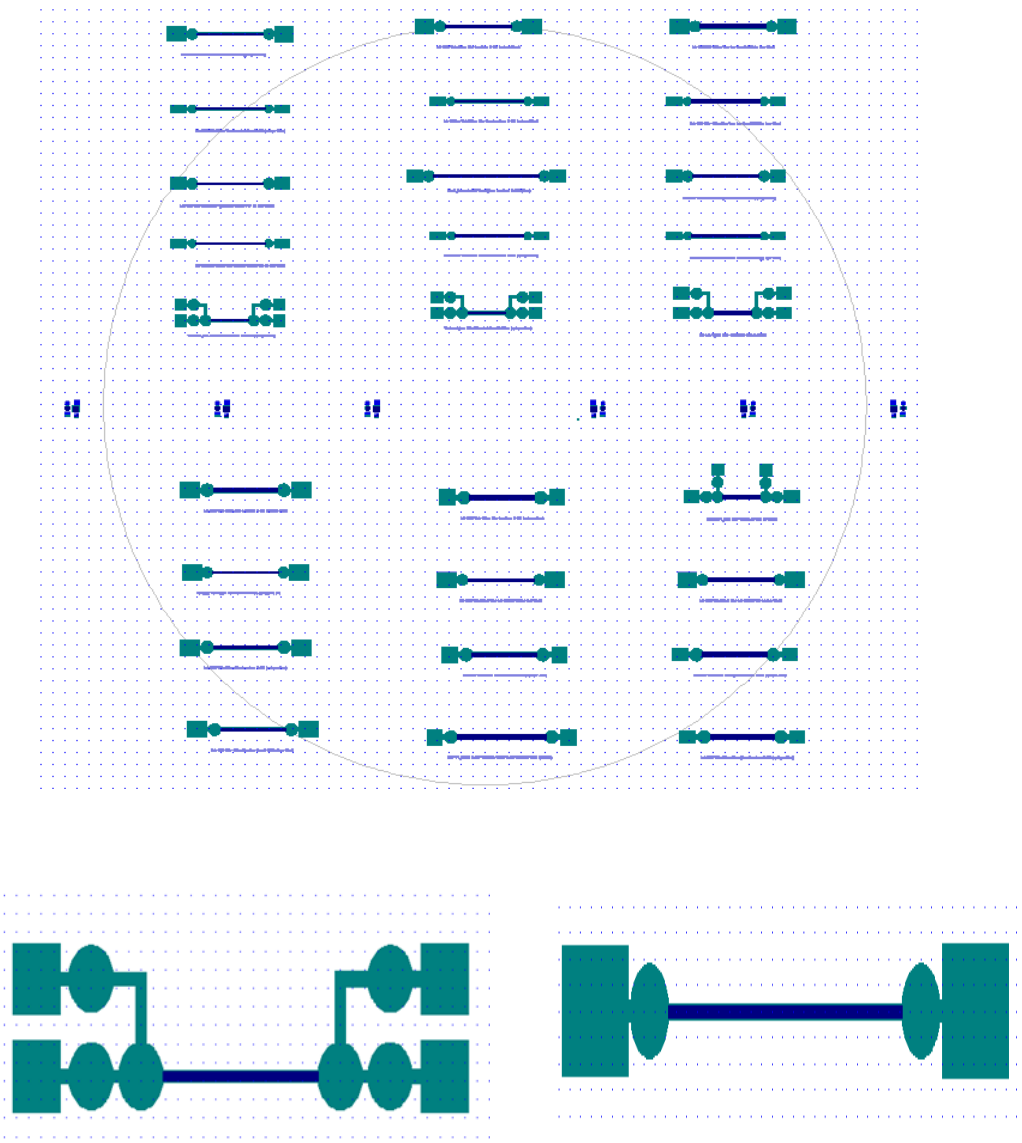

Figure 2.8 Design of the mask used for the microchannel patterning in the lithography step

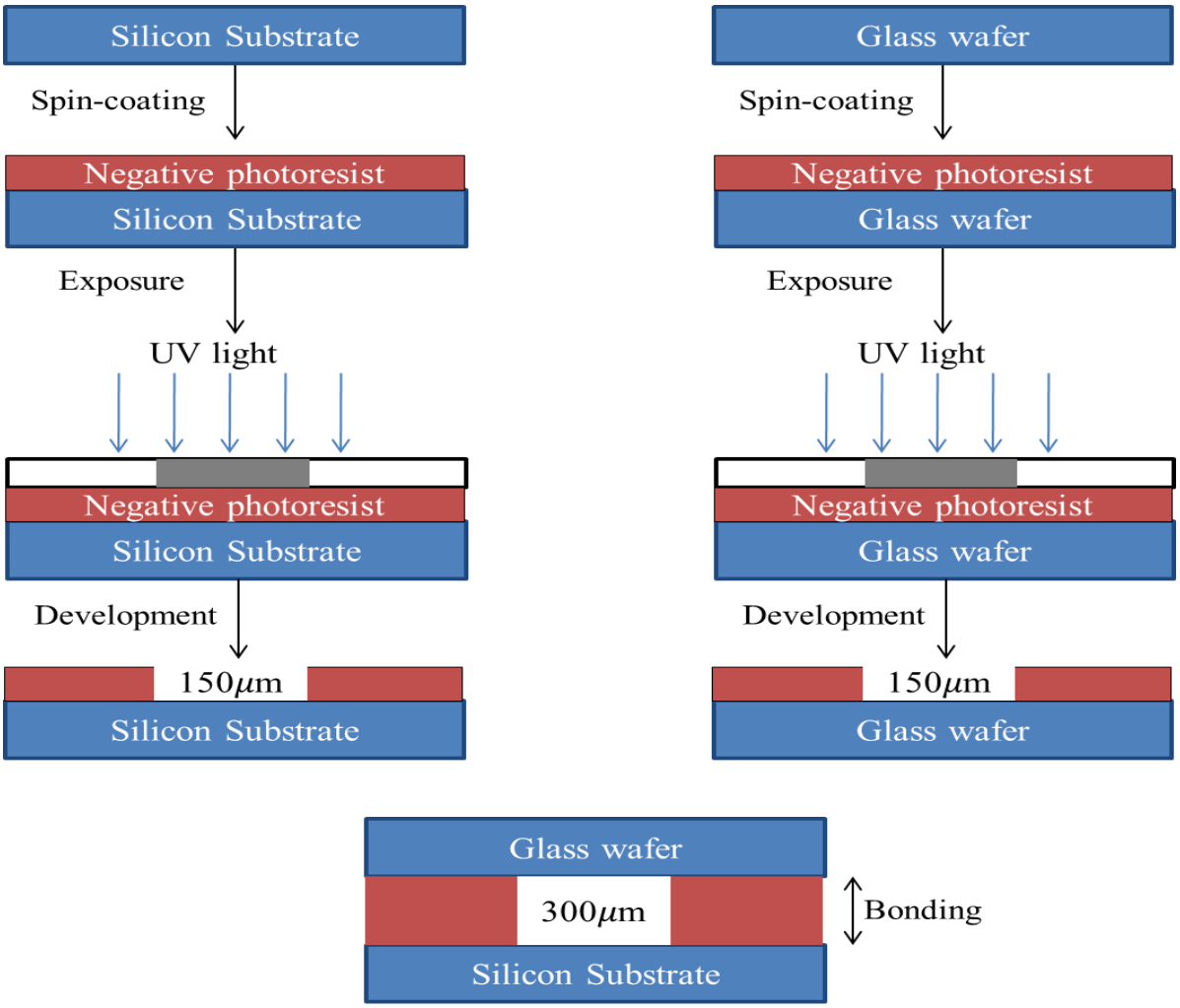

Figure 2.9 Process flow a) silicon wafer b) photoresist spinning and prebake c) Exposure and patterning d) development e) bonding of glass wafer

Figure 2.10 includes SEM images for the fabricated microchannels, Figure 2.11 is a real image for the microchannels.

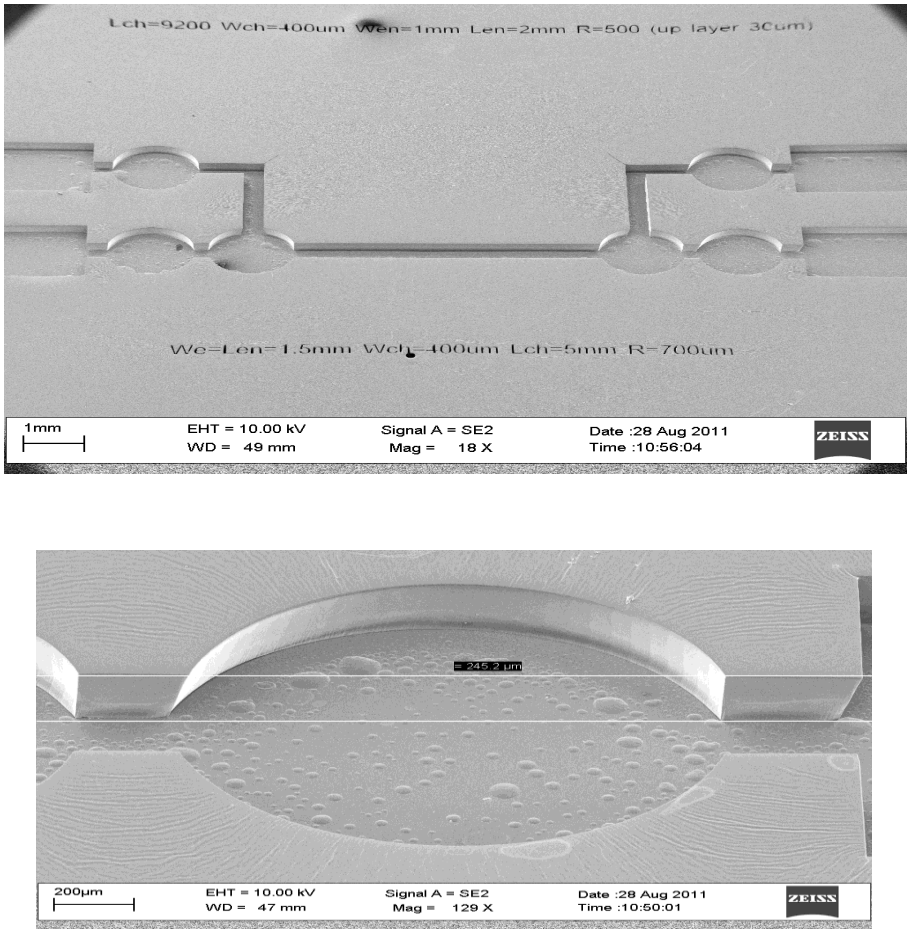

Figure 2.10 SEM images of the fabricated microchannels

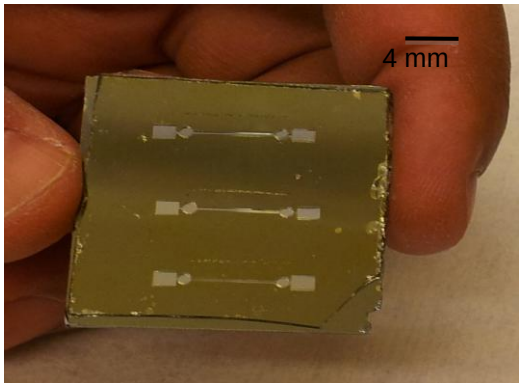

Figure 2.11 Fabricated microchannels array

Microchannels with thickness up to 300 µm were achieved with a single spinning process using this kind of photoresist. It has a rapid processing because in the case of AZ125nxt photoresist, post exposure baking is eliminated which makes the process less time consuming. These results show that this kind of resist has a better performance than the conventional one SU-8. It may replace it in many applications in order to have a biocompatible and robust design with low costs and short processing time.

3 Chapter III Analysis and simulations

In this chapter, the first section includes analysis and simulation of the mechanical model of a lamellar grating interferometer will be discussed in order to study the dynamics and stability analysis of the structure. In addition to the effect of different design parameters in order to make an optimization of the existing design for better performance is included. The second part of the chapter introduce a novel idea for beam splitting in interferometer based spectrometer that is based on spatial division of the beam using V shape mirror, FDTD simulation and a mechanical movable model for the structure are included in this chapter.

3.1 Analysis of lamellar grating microspectrometer

3.1.1 Mechanical model

As mentioned in chapter 1, the lamellar grating structure is mainly based on two sets of electrostatic comb-drives that are used as an actuator and a variable depth diffraction grating at the same time, resulting in a more compact device (Figure 3.1). The structure is working at resonance which produces higher displacement up to 100 μm peak to peak with lower driving voltage (28V) which increases the resolution of the interferometer to be about 0.4 nm in the visible range and 3.6 nm at 1.5 μm. In order to ensure the flatness of the surface during resonance, the two sets of movable fingers are positioned in a symmetric way on an H-shape backbone to provide a robust design. The H-shape backbone is attached to the fixed frame through a four folded flexure beams, which has a low stiffness to provide lower resonant frequency and high speed to fulfill the requirements of the readout electronics. Table 3.1 includes the information regarding the dimension [66] used in the design that will be used in the Comsol FEM simulation model.

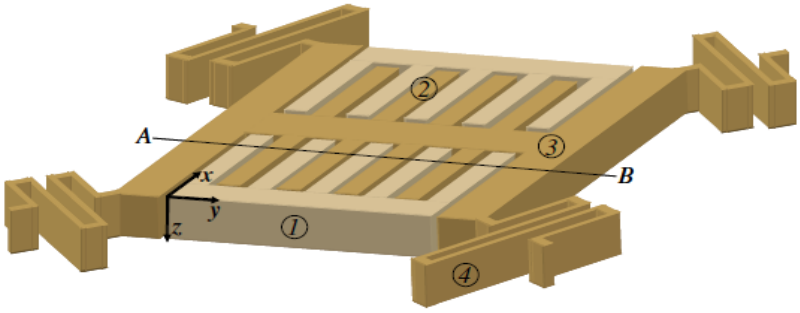

Figure 3.1 Lamellar grating structure [66].

Table 3.1: Structures dimensions

Dimensions	Value (μm)
Width of comb drive fingers	70
Length of comb drive fingers	1200
Gap between fingers	5
H-shape width	250
Number of fingers	14
Folded beam suspension length	1200
Folded beam suspension width	10
Folded beam corner width	30
Folded beam corner length	40
Gap between the folded beam suspension	20
Total length	2650
Total width	2700

The width and length of the fingers are 70 μm and 1.2 mm, respectively, and the gap is 5 μm. The high aspect ratio between the width and gap dimensions results in a high fill factor, resulting in better optical efficiency. On the other hand, the grating period increases, causing the decrease in the separation of diffraction modes according to Eq. (1.7, 1.8).The grating period has to satisfy two conditions in order to achieve good separation in orders and at the same time avoid the Talbot images thus a compromise has to be done to achieve good efficiency. Additionally to use the interferometer over a wide range, thin aluminum layer can be deposited on the fingers as a coating. Consequently increasing the reflectivity to be used in the visible and infrared range [66, 80].

3.1.2 Actuation of the mechanical part

Electrostatic comb drives are widely used as actuation mechanism for MEMS devices. Large displacement can be provided by this approach, and it is commonly used for the in-plane and out of plane actuation of micro-mirrors. Working in resonance, enable the achievement of larger displacement values with lower values of driving voltage. In resonance mode, the actuation depends on the resonance frequency and the Eigen values of the mechanical model. The change in the resonance frequency results in different oscillating mode, thus the comb-drive may be oscillating in-plane or out of plane, or rotational according to the excitation frequency [66, 80].

In lamellar grating interferometer, out of plane translational mode is the fundamental mode of the interferometer, and should be necessarily separated from the second mode to ensure that we are working in the out of plane mode. The design used provides the out of plane mode as the first mode. In order to verify the behavior of the design and the different Eigen modes and the static displacement of the structure Finite Element Method were conducted using Comsol Multiphysics® software.

For this design, structural mechanics module is used; we choose Eigen frequency study in order to verify the different oscillating modes of the structure. In the simulation only the movable part is simulated fixed in the four folded beam suspension, using the dimensions mentioned in

Table 3.1 above, and choosing 30μm which is the thickness of the structural layer of the SOI wafer (Figures 3.2, 3.3), the following results are obtained using Comsol Mutiphysics®.

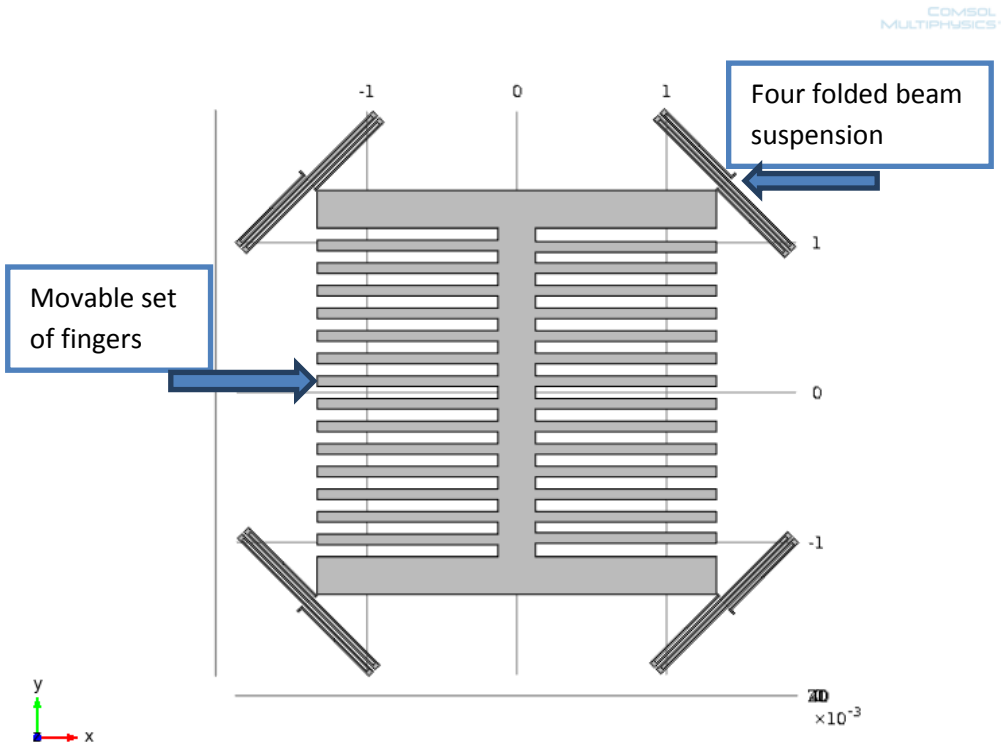

Figure 3.2 Design used in simulation

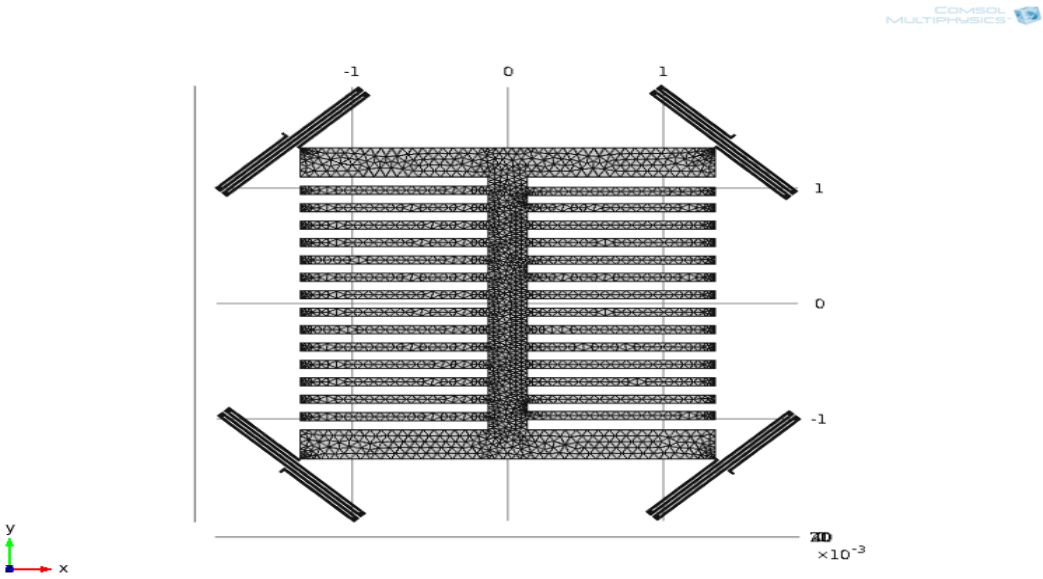

Figure 3.3 Fine mesh of the design to increase the accuracy of the solution

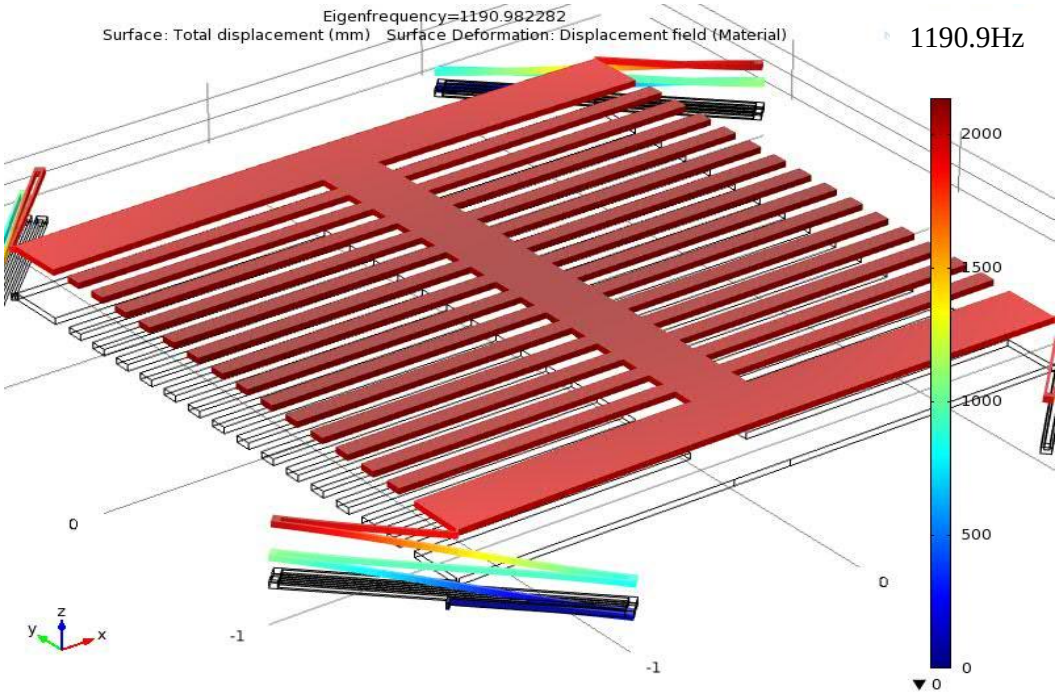

Figure 3.4 The first mode is resonating in out of plane direction with F=1190.9Hz

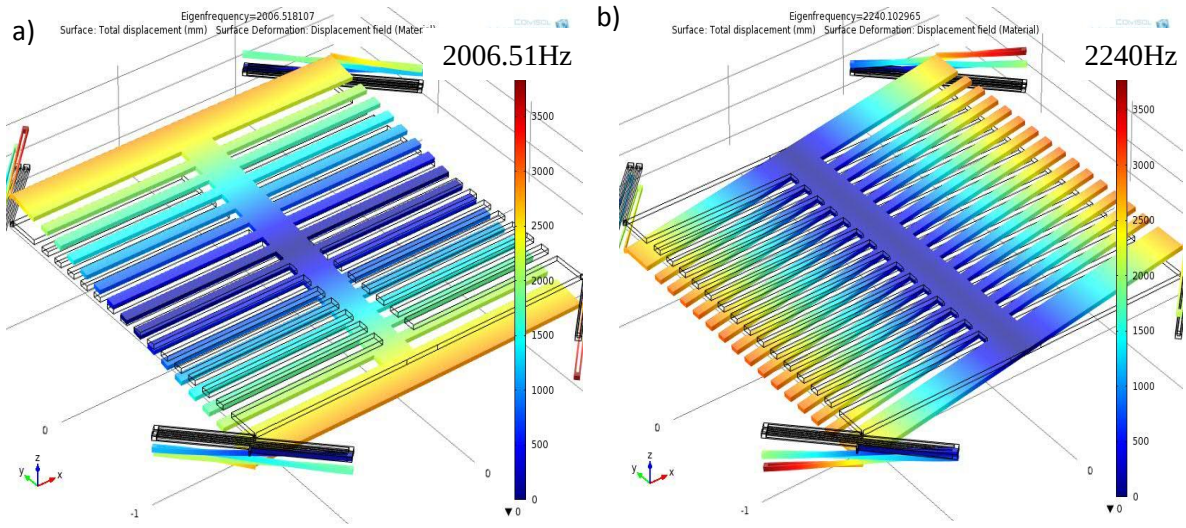

Figure 3.5 a) Second mode of resonance rotation around x b) Third mode of resonance rotation around y

Table 3.2: Simulation and theory results of frequencies modes

Mode frequencies	**FEM simulation Results (Hz)**	**Simulation results from literature (Hz) [66]**
First mode (out of plane translation)	1190 Hz	1156
Second mode (rotation around x)	2006.51Hz	1913
Third mode (rotation around y)	2240 Hz	2230

According to Figure 3.4 the fundamental mode is out of plane translation occurring at frequency equal to 1190 Hz, which fulfill the requirement of having the essential mode oscillating out of plane. Figure 3.5a shows the second mode which is rotational mode around the x axis at frequency equal to 2006.5 Hz and Figure 3.5b is the third mode is rotating around the y axis at frequency equal to 2240 Hz. Comparing these results to the one obtained in the literature of exactly the same design, the results are comparable (Table 3.2). Additionally when comparing the fundamental mode to the second mode a good separation between them is maintained, which fulfills the condition of having the first mode separated from the following mode to ensure the out of plane oscillation.

Using stationary study in Comsol Multiphysics the spring constant *"K"* is determined, to be used in further studies in the mechanical model, and to get the maximum displacement achieved by the structure. The following results were obtained by conducting a parametric study, in which the applied force is varied to monitor the change in the displacement in stationary study. Since the force can be given by:

$$F = kx \tag{3.1}$$

Where, F is the mechanical force, K the spring constant and x is the resulting displacement
Consequently, the slope of the force versus displacement graph in Figure 3.6 gives us the spring constant value.

Figure 3.6 shows the difference values of the force applied on the structure with the appropriate displacement occurring for each applied force, according to these results the value of the spring constant *"K"* equal 16.7 µN/µm.

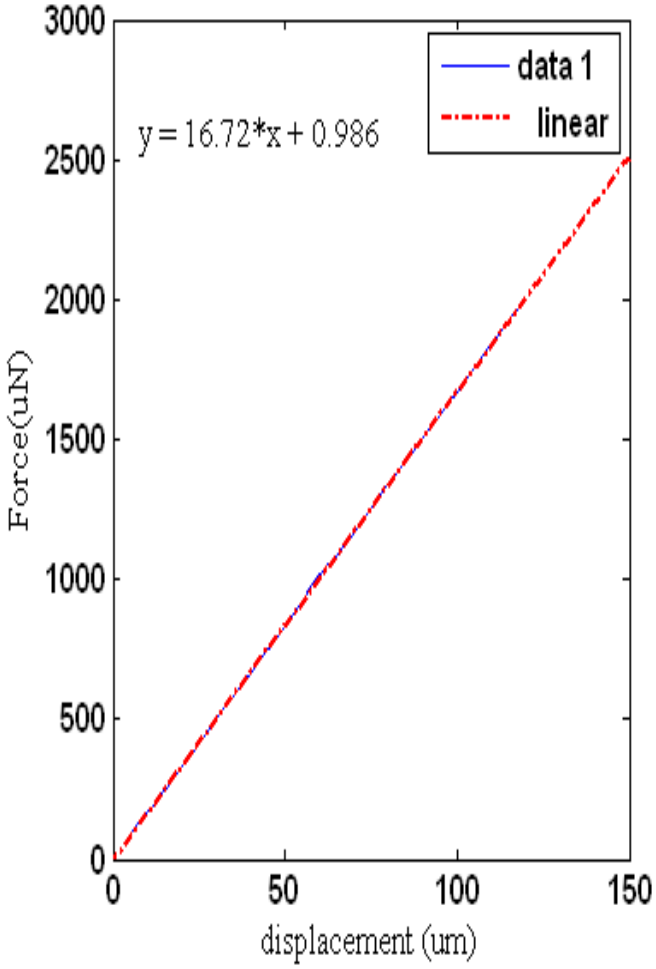

Figure 3.6 Force versus displacement curve to calculate the spring constant K

The structure can be considered as a parametrically exited MEMS oscillator. It can be modeled using the second order nonlinear differential equation of motion with a single degree of freedom (DOF). In the following part equations describing the system are given to be used in the analytical model for the system study [88-91].

The equation of motion can be given by:

$$m\frac{d^2z}{dt^2} + b\frac{dz}{dt} + k_f z = F_{es}(z,t) \quad 3.2$$

Where, m is the mass, b is the damping factor, K_f is the mechanical stiffness and F_{es} is the electrostatic force.

The restoring force, related to the mechanical springs can be given by [92]:

$$F_r(z) = k_f x \quad 3.3$$

The electrostatic force resulting between the comb drive fingers can be given by:

$$F_{es}(z,t) = N\frac{dc}{dz}V(t)^2 \quad 3.4$$

Where N is the number of fingers, C is the capacitance of a single finger, and V is the applied voltage.

For small displacement, the electrostatic force can be described by:

$$F_{es}(z,t) = (r_{1A}z + r_{3A}z)V^2(t) \quad 3.5$$

Where r_{1A} and r_{3A} are the Taylor series expansion coefficient of the deflection of the capacitance derivative, which has only odd terms

To produce harmonic excitation, the applied voltage used is:

$$V(t) = V_A\sqrt{1+\cos wt} \quad 3.6$$

Substituting these values in Eq. (3.2), thus the equation of motion becomes:

$$m\frac{d^2z}{dt^2} + b\frac{dz}{dt} + (K_f + r_{1A}V_A^2(\cos wt + 1))z + (r_{3A}V_A^2(\cos wt + 1))z^3 = 0 \quad 3.7$$

The right hand side of Eq. (3.7) is equal to zero, thus it has no constant force term, and consequently the system is not exited by applying DC voltage.

In order to study the design and get the maximum displacement that can be achieved by applying certain value of voltage, the Taylor series coefficients must be calculated and a solution from the differential equation of motion has to be used to get the value of the out of plane displacement.

To calculate the Taylor series expansion coefficient of the deflection of the capacitance derivative, the rate of capacitance displacement with respect to the z-direction displacement (dc/dz) for the comb drive fingers should be modeled using Maxwell 3D® simulator (Figure 3.7). Even though the force is independent of the displacement in in-plane actuation, but for out-of-plane motion the actuation is highly dependent on the displacement.

.

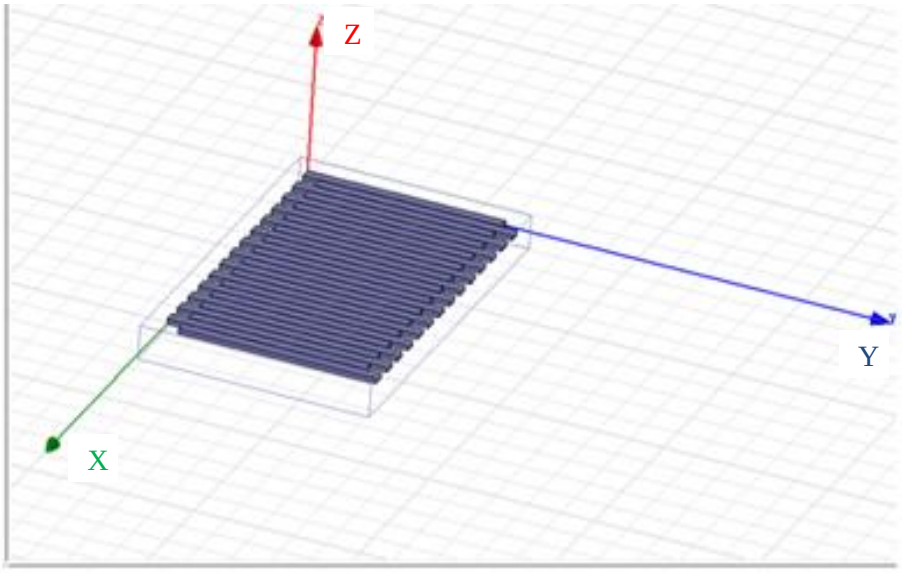

Figure 3.7 Comb drive model using Maxwell 3D simulator to get the rate of capacitance displacement versus z-direction displacement

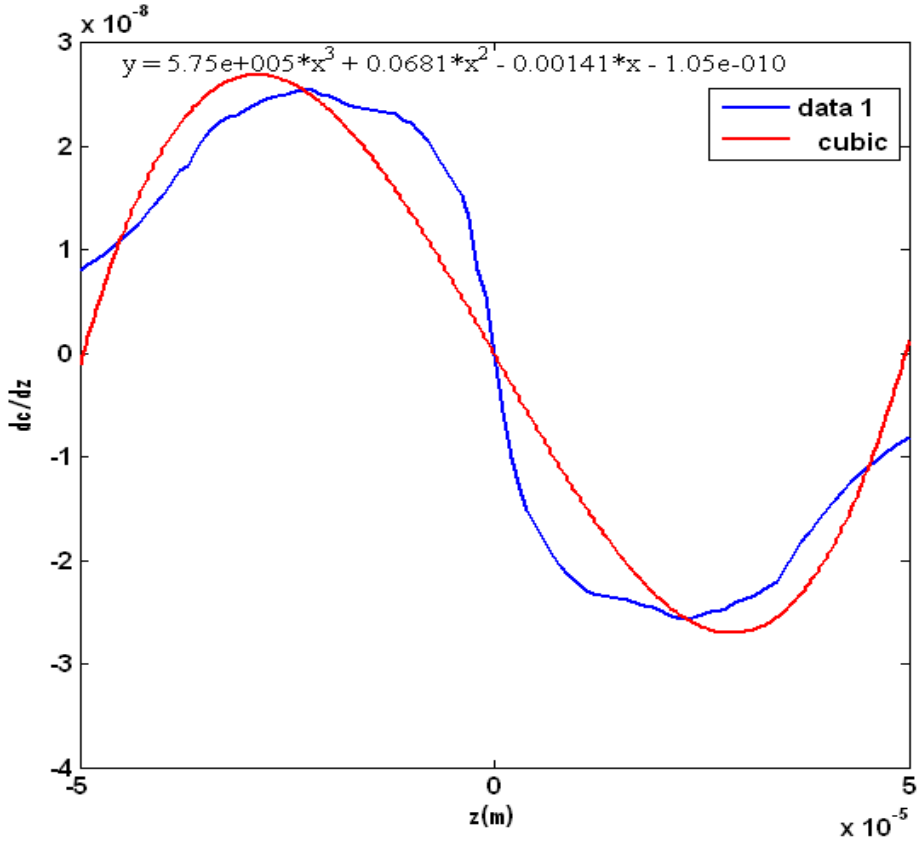

Figure 3.8 Rate of capacitance displacement with respect to the z-direction displacement and the cubical fitting

Figure (3.8) shows the results obtained for the rate of capacitance change with respect to the z-direction displacement by modeling the comb drive using Maxwell 3D simulator. From these results, the Taylor series coefficient r_{3A} and r_{1A} are equal to 5.75e+005 and -0.00141 respectively.

Consequently after calculating the Taylor series coefficient a solution for the differential equation of motion (Eq. 3.7) is required to calculate its coefficient and get the displacement.

Normalizing the equation to the mass m, and combining some coefficient together, the equation of motion that will be used in this analysis becomes:

$$\frac{d^2z}{d\tau^2} + 2\xi\frac{dz}{dt} + z(1+\lambda_1+\lambda_1\cos\Omega\tau) + z^3(\lambda_3+\lambda_3\cos\Omega\tau) = 0 \qquad 3.8$$

Where, ξ is the normalized damping coefficient, λ_1 is the linear electrostatic excitation amplitude, λ_3 is the non linear electrostatic excitation coefficient, Ω is the normalized excitation frequency.

$$\tau = \omega_0 t \qquad 3.9$$

$$\omega_0 = \sqrt{\frac{k}{m}} \qquad 3.10$$

Where $\omega_0$is the resonance frequency of the structure.

$$\Omega = \frac{\omega}{\omega_0} \qquad 3.11$$

In this type of oscillators the excitation frequency should be nearly twice the mechanical resonance frequency of the structure, in order to achieve the instability region to begin the oscillation causing the maximum displacement from the structure (Figure 3.9) [93]. In this case the resonance frequency of the fundamental mode is 1190 Hz, and so the excitation frequency should be around 2380 Hz.

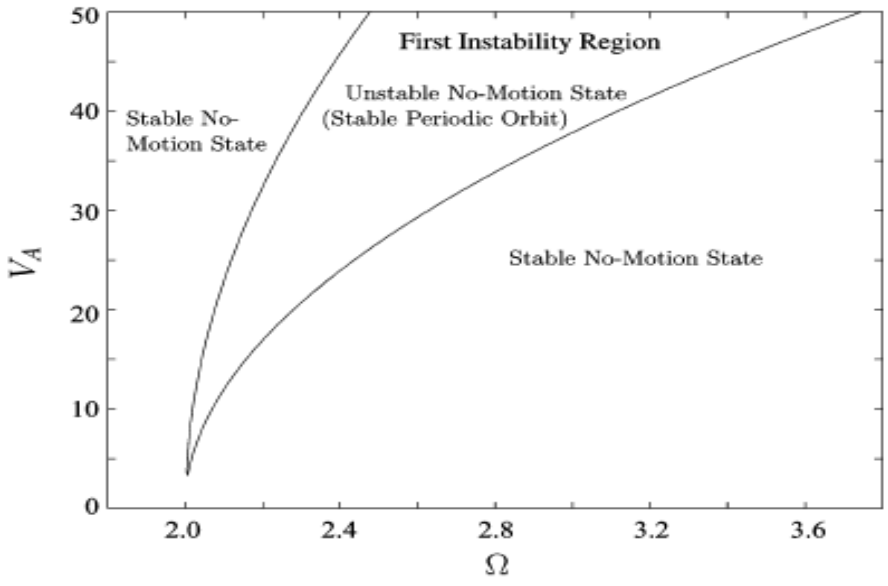

Figure 3.9 Excitation voltage versus normalized frequency [97]

In this analysis a coefficient σ is introduced to measure the nearness of the excitation frequency to the fundamental resonance of the structure and also to analyze the stability of the system around this excitation frequency, such as:

$$\Omega = 2 + \sigma \tag{3.12}$$

The approach used for the analysis of (Eq. 3.8) is the averaging approach in which a coordinate transformation is applied to change the equation into amplitude and phase coordinated such as:

$$z(\tau) = a(\tau)\cos(\frac{\Omega\tau}{2} + \psi(t)) \tag{3.13}$$

$$z'(\tau) = -a(\tau)\frac{\Omega}{2}\sin(\frac{\Omega\tau}{2} + \psi(t)) \tag{3.14}$$

In the following solution, steady state analysis are conducted and zero damping is considered, which results in a solution for this equation including three sets of coefficient as a solution for this differential equation, given by [91]:

$$a_1 = \sqrt{\frac{4\Omega - 2\lambda_1}{\lambda_3}} \tag{3.15}$$

$$a_2 = \sqrt{\frac{4\Omega - 6\lambda_1}{5\lambda_3}} \tag{3.16}$$

$$a_3 = \sqrt{\frac{-2\lambda_1}{\lambda_3}} \tag{3.17}$$

Replacing the previous results for the Taylor series coefficient r_{1A} and r_{3A} in the coefficients a_1, a_2, a_3, we get the frequency response of the design using MATLAB (Figure 3.10).

Figure (3.10) shows the frequency response "σ "which is equal to $(\Omega - 2)$ versus the displacement, thus it shows us the behavior of the structure for different excitation frequencies approaching to the double of the fundamental resonating frequency. This model is used to study the stability of the system by varying the excitation frequency by σ which is the coefficient measuring the closeness of the excitation frequency to the condition requiring it to be around the double of the fundamental resonance frequency.

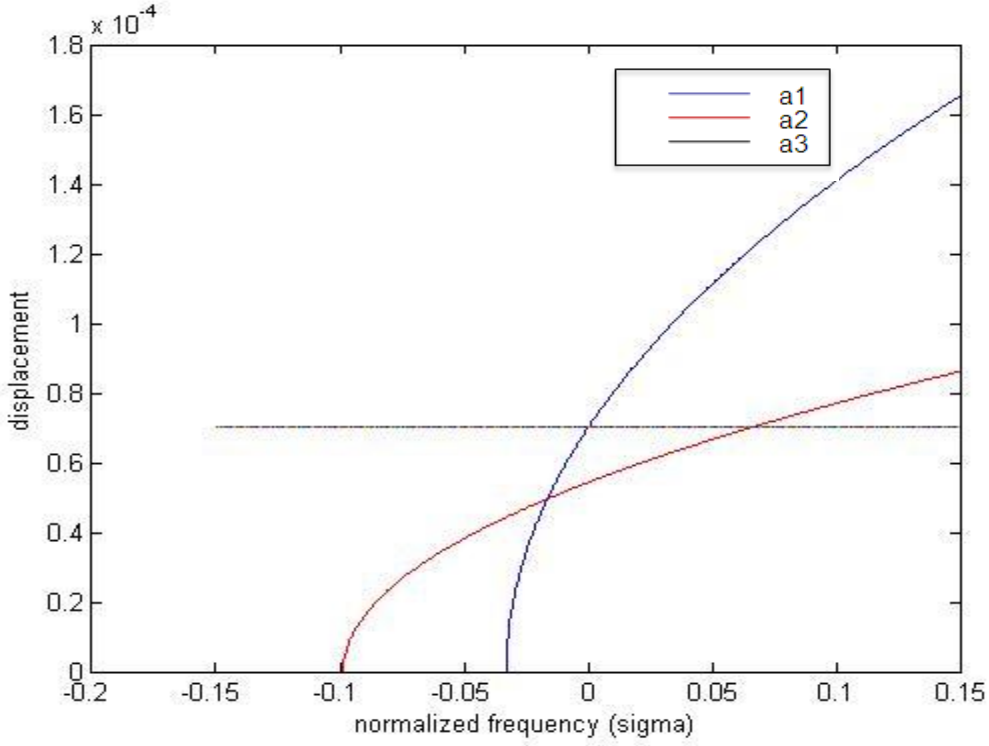

3 Frequency response of the design which is σ versus displacement

Using a Matlab model, stability analysis based on phase plane trajectory were generated for different values of sigma "σ", Figure (3.10) shows that the stable region around which the excitation can occur is from$\sigma = -0.04$ to $\sigma = -0.1$, which will be proved in the following stability analysis by taking different values for σ.

In Figure (3.11) when sigma =0 this means that the excitation frequency is exactly equal to the double of the fundamental resonance frequency. In this case the solution is zero and the system is unstable. Therefore a variation of the value of sigma is needed until an intersection

between phase and amplitude occurs in this case these points of intersections are considered as a solution for the system.

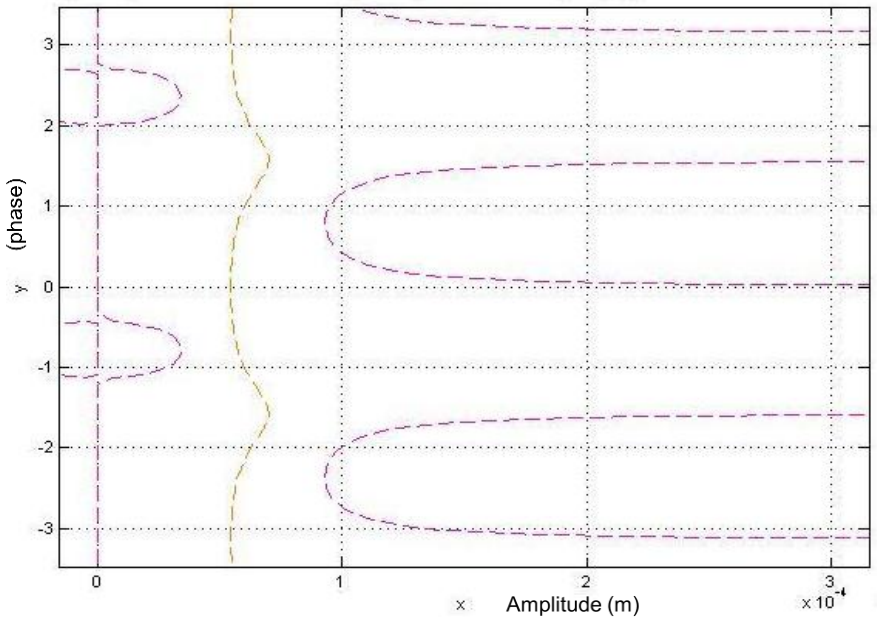

Figure 3.10 Stability diagram forσ =0

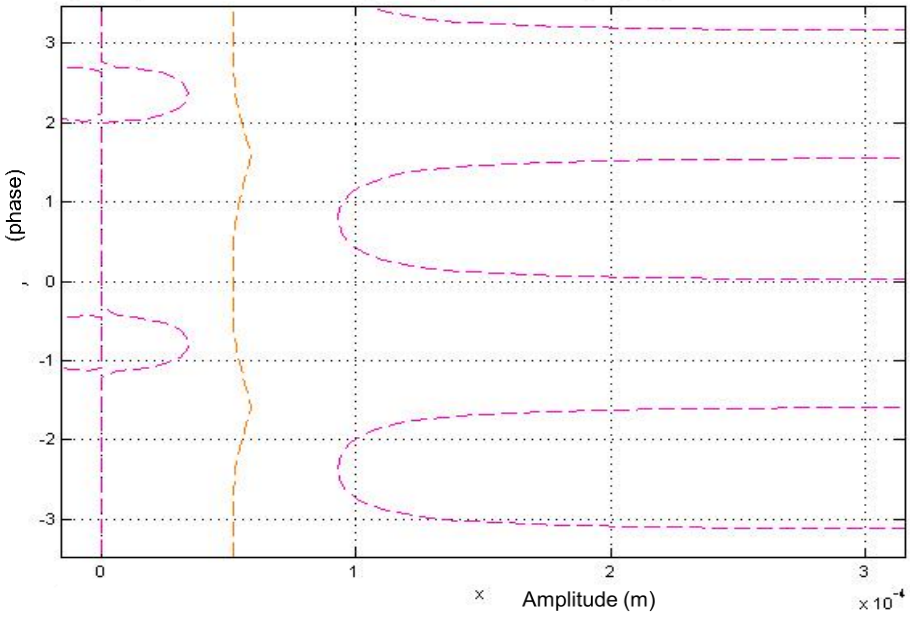

Figure 3.11 Stability diagram for σ= -0.01

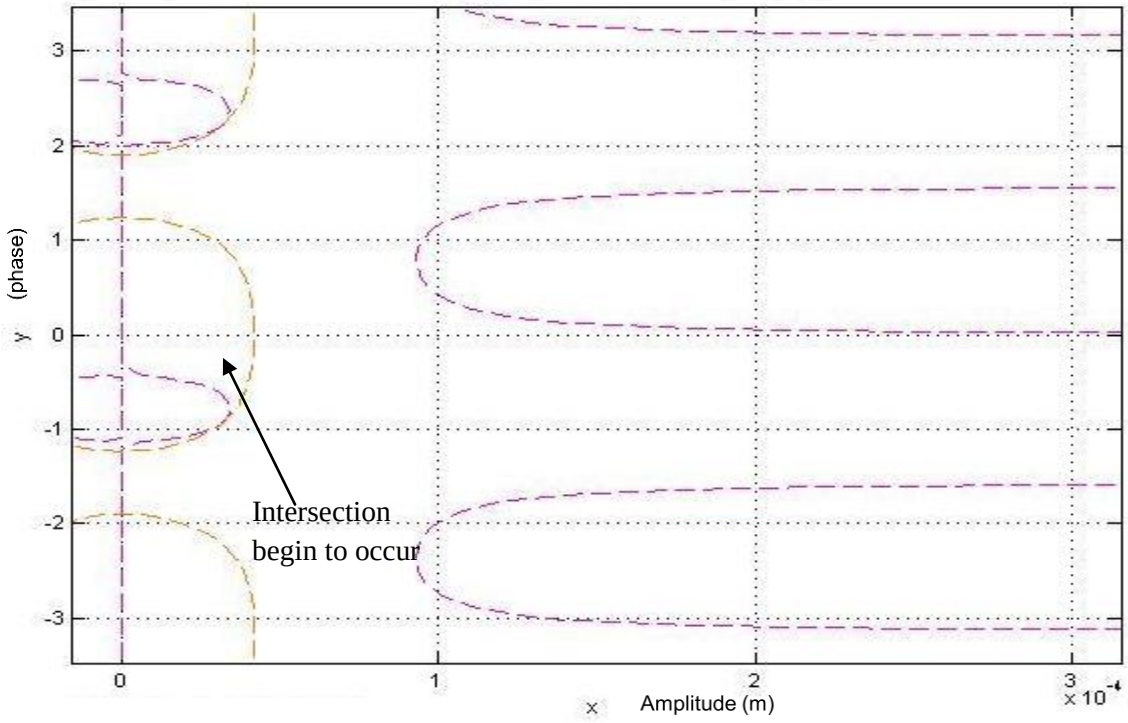

Figure 3.12 Stability diagram for σ =-0.04

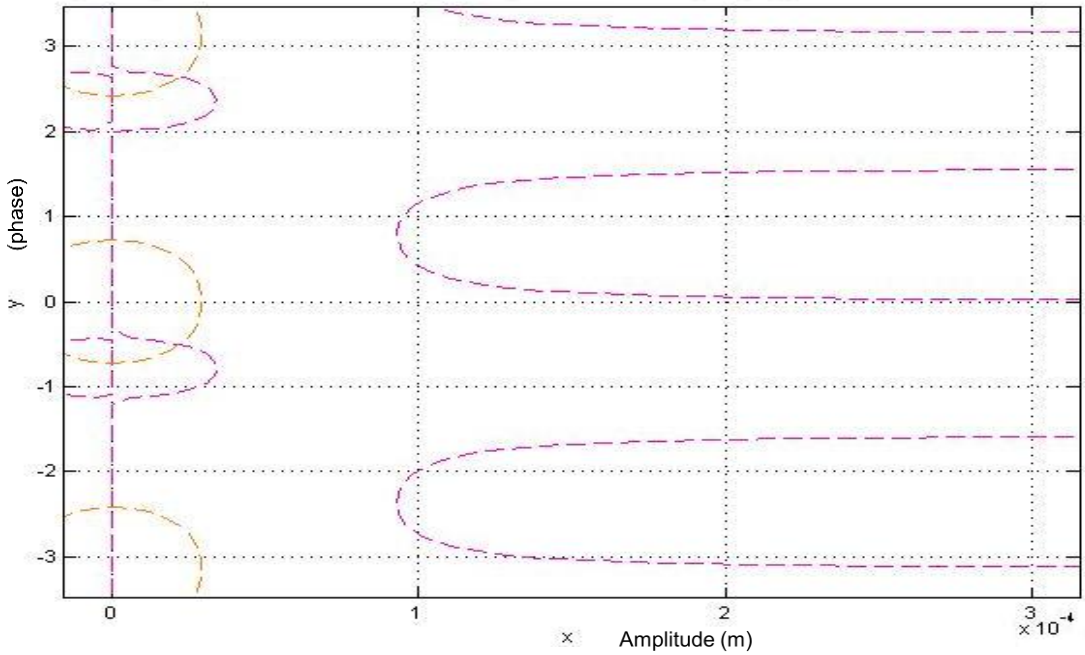

Figure 3.13 Stability diagram for σ =-0.07

Figure (3.13) and figure (3.14) show the beginning of an intersection that is occurring between the amplitude and phase giving a solution for the system. Values of x axis represent the initial displacement that can be used as the initial condition to be given to the system in order to start the oscillations.

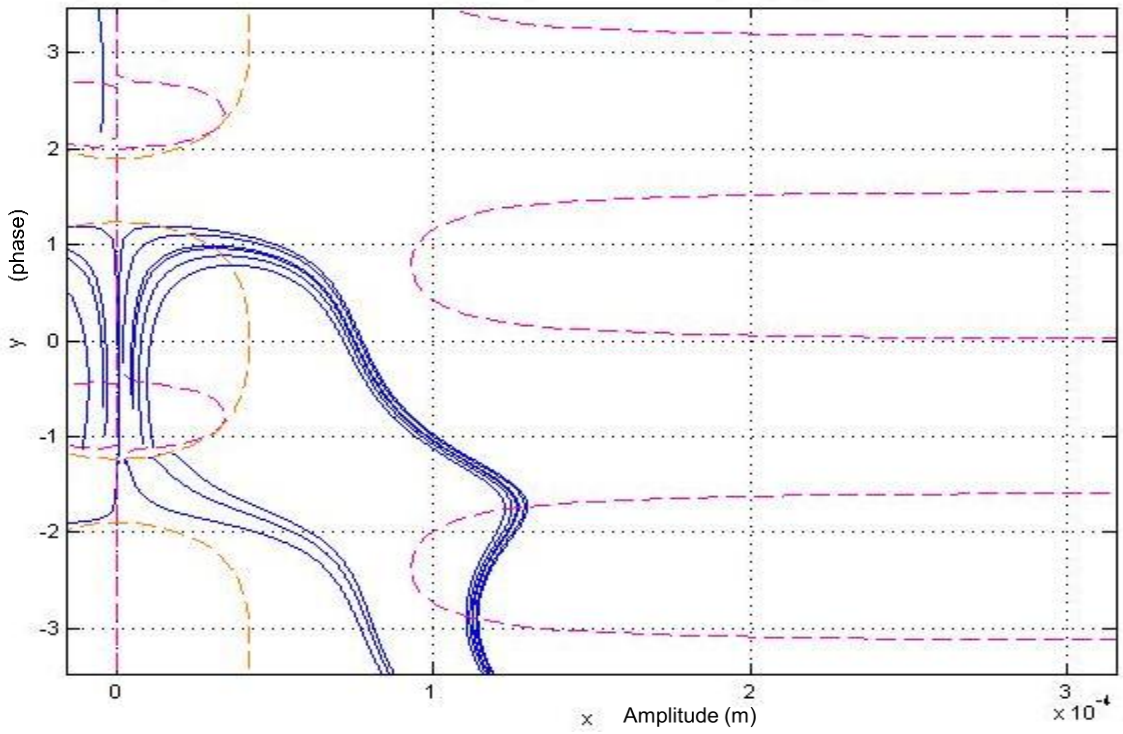

Figure 3.14 Stability diagram for σ=-0.04 showing the initial conditions that can be used as initial displacement for the oscillator

In Figure 3.15, the blue line shows the path taken by hitting a point as initial condition which would be like the noise that will start up the oscillations, the lines do not decay into zero which prove the stability of the system.

To analyze the maximum displacement that can be achieved using this design, a Simulink model was generated on MATLAB, in which all the previous results and calculated coefficient were used as an input for the model, as well as the initial condition taken from the stability diagram were used (Figure 3.16).

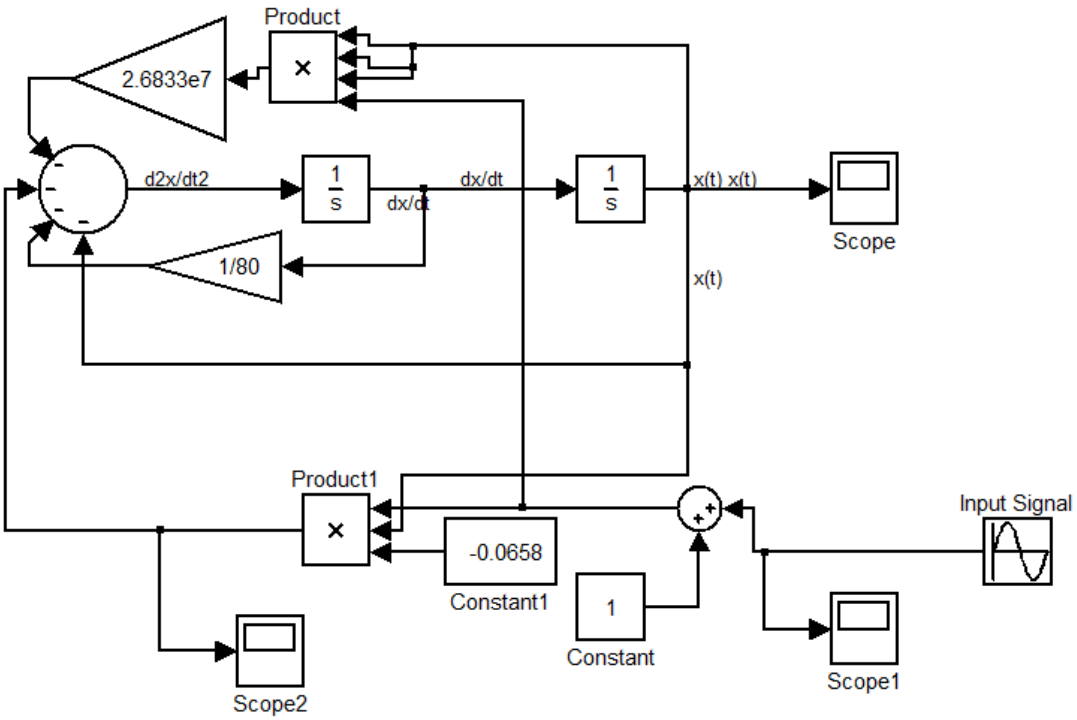

Figure3.15 Simulink model used to get the transient response of the system

Figure 3.17 shows the transient response of the structure. The maximum displacement achieved is 84 μm, with applied voltage 28 V.

The resolution of the system is given by:

$$\frac{\Delta\lambda}{\lambda} = 0.17\frac{\lambda}{d_{\max}} \qquad 3.18$$

In this case the resolution of the structure according to the achieved displacement is 0.3 nm to 1.13 nm for wavelengths 380 nm and 750 nm respectively.

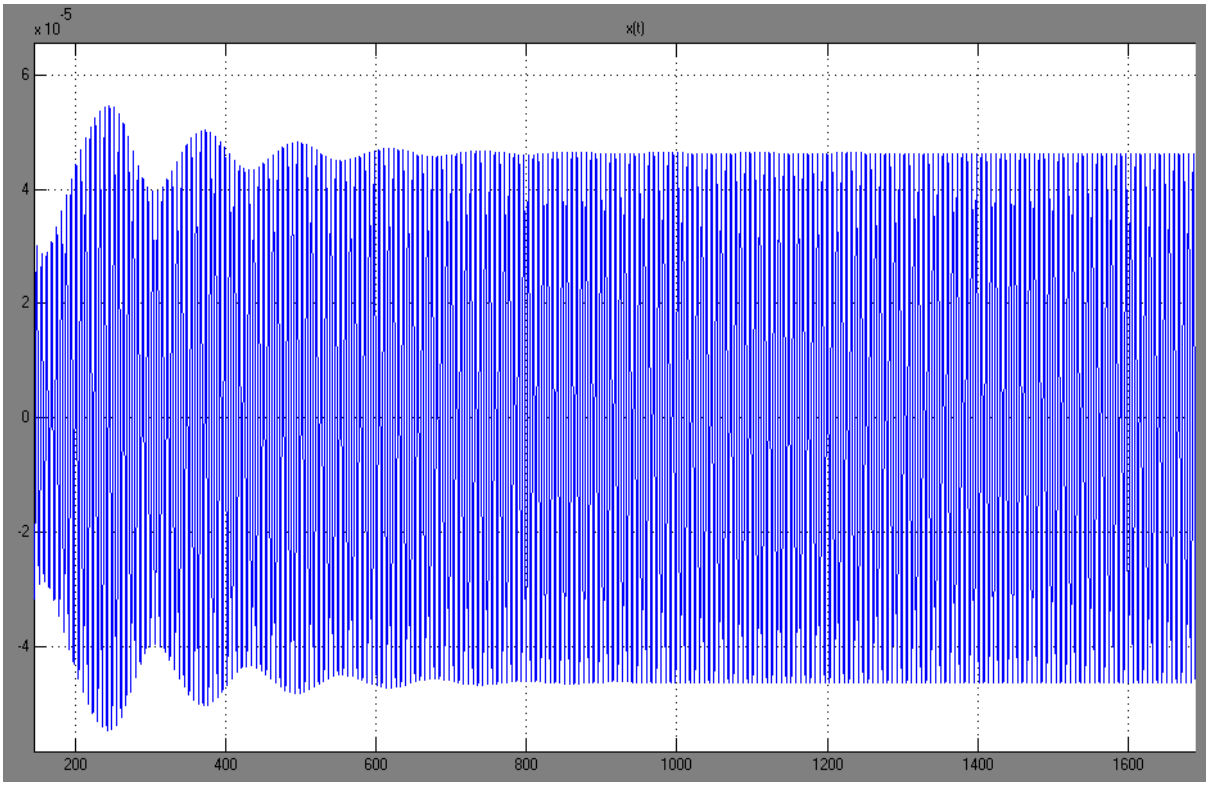

Figure3.16 Transient response of the system achieving displacement from -42 µm to 42 µm

According to (Eq. 3.18), the resolution of the spectrometer is inversely proportional to the maximum displacement that can be achieved, hence for further improvement of the design higher displacement are required.

A variation of certain parameters of the design was conducted in order to study its effect on the performance of the interferometer, and if we can achieve higher displacement. The first parameter to be studied is the thickness of the structural layer of the design.

Table 3.3: The variation of the thickness of the structural layer with the frequency modes for each thickness

Thickness	F1 (Hz)	F2 (Hz)	F3 (Hz)
30 μm	874	1477	1654
50 μm	1390	2145	1259
75 μm	1934	2148	2162

From Table 3.3, the results show that when the thickness is increased the fundamental resonance frequency is increased this affects the speed requirements for the detection. Additionally when the thickness is increased, the mode separation is decreased which makes a disadvantage for separating the fundamental mode and the other Eigen modes.

According to (Eq. 3.4), the electrostatic force is directly proportional to the square of the applied voltage. The results in Table 3.4 show that increasing the voltage increases the displacement but at some point, the effect is nearly stable.

Table 3.4: Variation of the applied voltage and the resulting displacement

V(t)	d_{max}
28 V	*-50 μm to 50 μm*
40 V	-62 μm to 62 μm
75 V	-61 μm to 61 μm

Further important design parameters that affect the structure are the design of the folded beam suspension. If the number of folded suspension in increased, the stiffness “k” decreases

which allows the achievement of higher displacement. However the separation between the modes becomes lower, thus a compromise between the higher displacement and the mode separation has to be done. Additionally the spaces between the folded beams affect highly the fundamental mode of oscillation which may eliminate the out of plane mode to be the first mode of oscillations, hence destructing the behavior of the design.

3.2 Novel interferometer design

We have seen that the lamellar grating interferometer design has eliminated the use of beam splitter used in conventional Fourier transform spectrometer by using a variable depth grating that divide the wave fronts instead of wave amplitudes. It has increased the maximum optical path difference by using out of plane translation at resonance thus achieving high displacement at lower applied voltage. However this structure suffers from high non linearity as it is considered a nonlinear parametric oscillator. Also a compromise between the mode separation and high displacement is required. Additionally, the integration of this design with the microfluidic platform for the optical detection of heavy metal is difficult. Hence a novel spectrometer that is based on spatial division of the beam using V shape mirror will be introduced in this section, solving the problem of integrating the beam splitter in MEMS based spectrometer, but at the same time with simple, robust and low cost design.

The approach is based on spatial division of an input Gaussian beam into two symmetric Semi-Gaussian beams using V shape mirror. The main advantage of this design that it can be fully integrated; additionally it can be used over a wide spectrum range in the visible and infrared regions. Moreover there is no power reflected back to the source, hence we are taking advantage of the whole power. Accordingly, multiple reflecting mirrors can be used to increase the optical path difference to improve the resolution [98].
In the following sections, a simulation of the design using Finite Difference Time Domain method is conducted to study the design and the effect of different parameters. Finally a mechanical model for the actuation of the mirror is developed achieving 160 μm displacement.

3.2.1 Design

The proposed design shown in Figure 3.18 uses a V shaped MEMS mirror to spatially divide a Gaussian beam into two equally semi-Gaussian beams. The fabrication of the proposed design is simple and feasible using MEMS technology, as it allows accurate alignments of the center of the input source relative to the V shape mirror hence ensuring perfect beam splitting. In order to

increase the reflectivity of the mirrors a thin aluminum layer is deposited on the whole structure, which doesn't require complicated steps to cover specific areas.

After the V shape mirror, the incident Gaussian beam is divided and the width of the Semi-Gaussian Beam (SGB) is now half the width of the input source. Due to diffraction phenomena the width of the SGB will be larger than the half value of the input source. Afterward the SGB passes through movable reflecting mirrors, which increases the optical path difference consequently increasing the resolution. The required applied voltage is decreased as well as the area. In this design it is increased by a factor of four, and at the same time all the power is reflected so there is no power going back to the source which increases the power to noise ratio. At the end the final mirrors are titled a little to ensure the occurrence of interference between the outputs SGB and the interference pattern is detected [98]. In this proposed design the V shape mirror has a sharp edge which may be difficult to adjust during fabrication, thus in the following parts the V shape mirror with sharp edge is replaced with rounded edge mirror and the behavior of the design is studied.

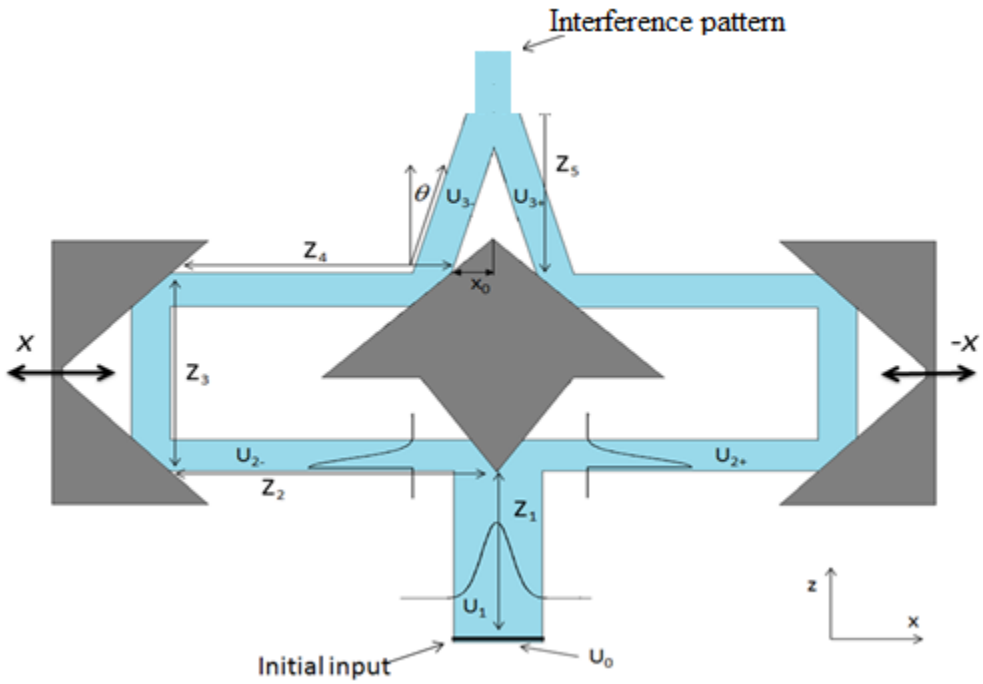

Figure 3.17 Novel design for beam splitting using V shape mirror [98]

3.2.2 Optical modeling and verification

For the optical modeling of the interferometer there are many numerical and analytical techniques to be conducted for the optical modeling. One of the most commonly used numerical analysis is the Finite Difference Time Domain method FDTD which is a computational electrodynamics method used to solve Maxwell equations in the time domain via replacing the derivatives by finite differences [94, 95]. This method rely on a systematic and accurate scheme for modeling optical beam propagation in complex geometry.

The design described above (Figure 3.18) is modeled using Lumerical FDTD simulator to study the beam splitting and the electric field propagation. Figures (3.19, 3.20) show the result of the Electric field propagation versus the position for wavelengths 700 nm and 1.55 µm respectively using an input Gaussian beam of 30 µm waist. The sharp V shape mirror divide the input beam into two symmetrically SGB. Then the SGB is reflected through the movable reflecting mirror until an interference occur at the output where we can see the fringes (dark and light fringes) constituting the interference pattern.

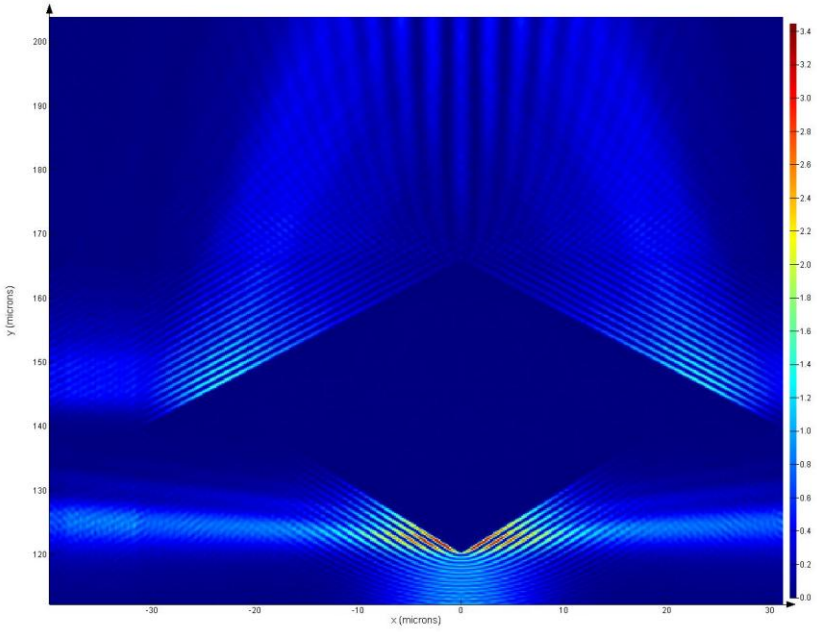

Figure 3.18 Electric Field intensity versus position for wavelength 700nm in the visible range

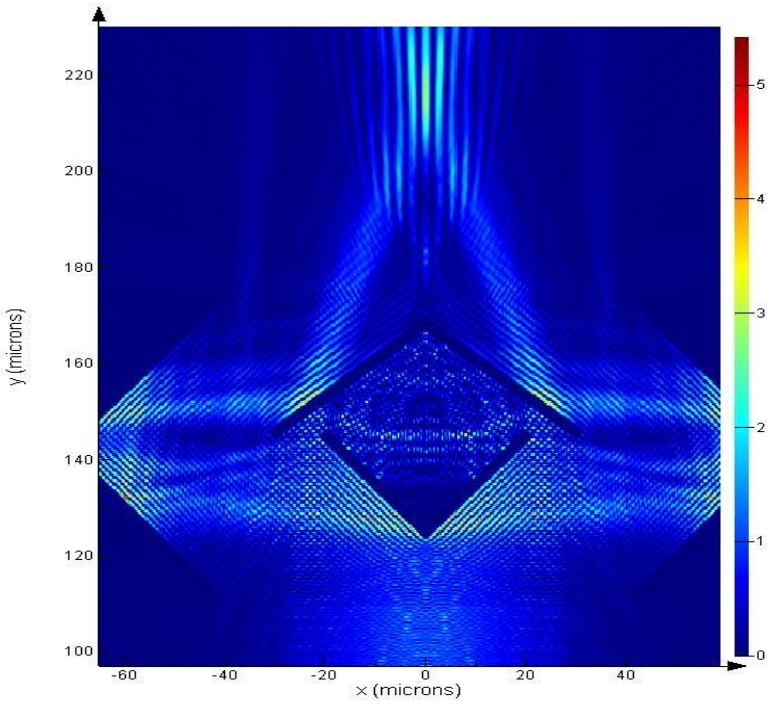

Figure 3.19 Electric Field intensity versus position for wavelength 1.55 µm in the IR range

Figure 3.21a shows the results for a working wavelength 700 nm in the visible range, while Figure 3.21b shows the results for a working wavelength 1.55 μm in the Infrared region. For these wavelengths a small wide band is used in simulations not a single wavelength. This shows that the design can be used over a wide range of wavelengths from the visible range to the infrared region giving an advantage to be applied in many applications. It doesn't also require a modification of the design, only the detector used define the working range of wavelengths.

In order to study the behavior of the design, one of the mirrors is moved in order to have an optical path difference of $\lambda/2$. In this case a destructive interference takes place, Figure 3.22 shows the results for both constructive and destructive interference simultaneously.

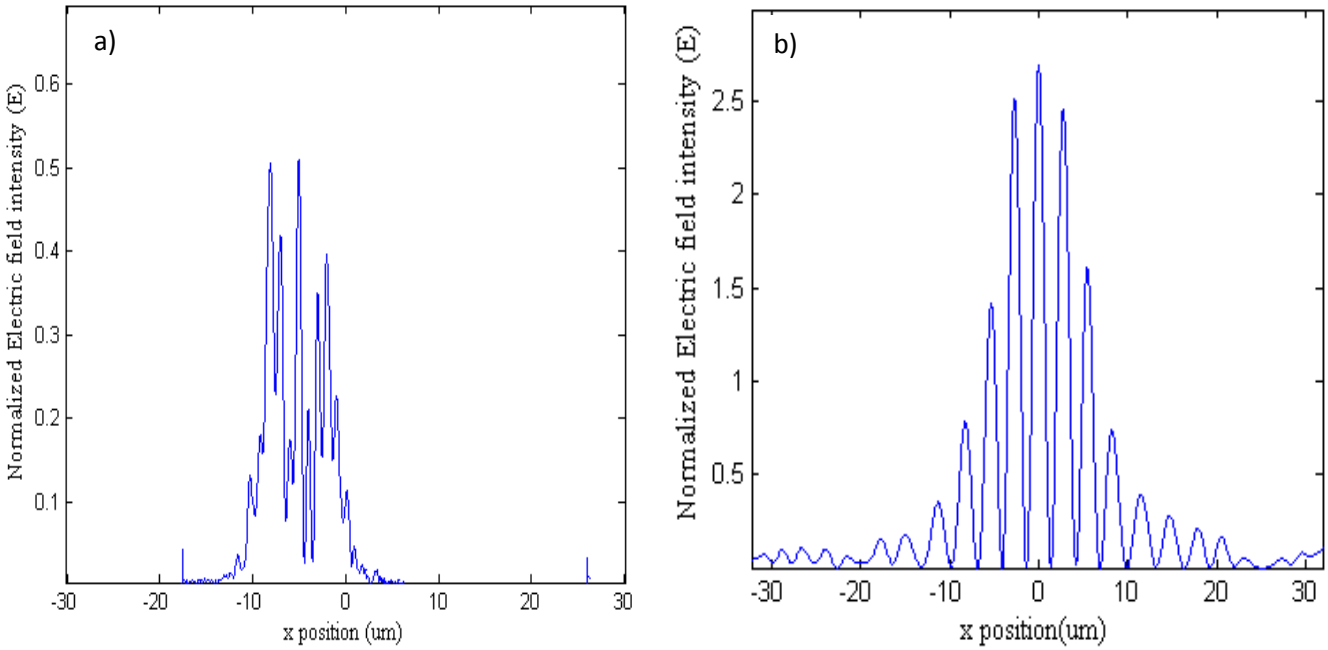

Figure 3.20 Normalized Electric Field intensity versus x position for a) 700 nm wavelength b) 1.55 µm wavelength

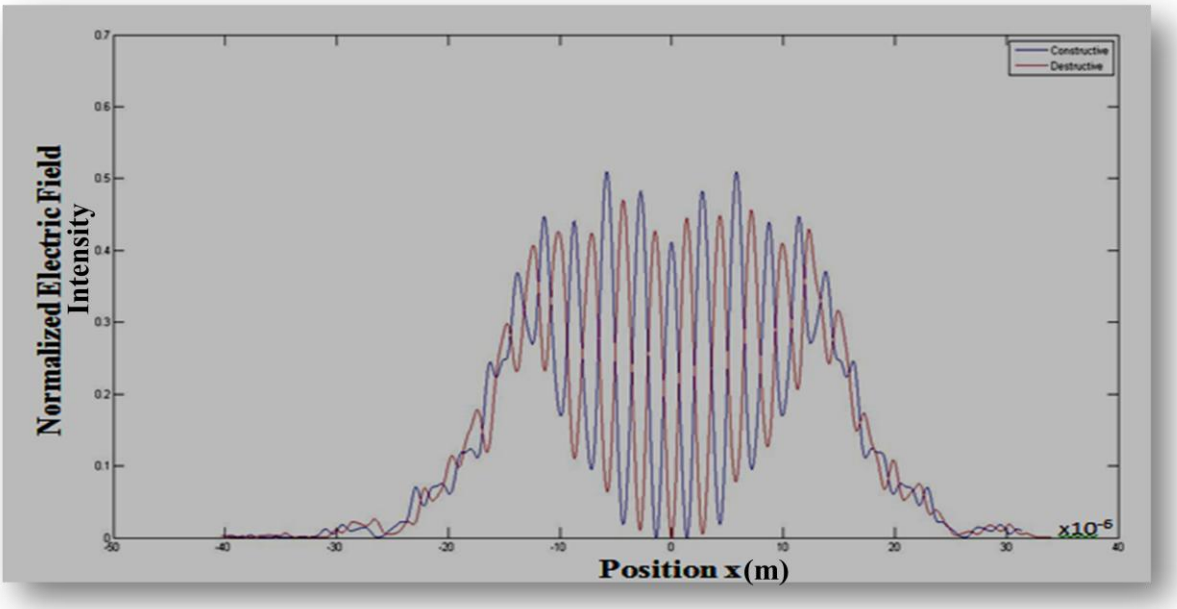

Figure 3.21 Constructive and destructive interference for 700 nm wavelength

In order to study the effect or any mismatches during the fabrication, the sharp V shape mirror in the design is substituted with a rounded edge V shape mirror (Figure 3.23), and the analysis are done after this modification.

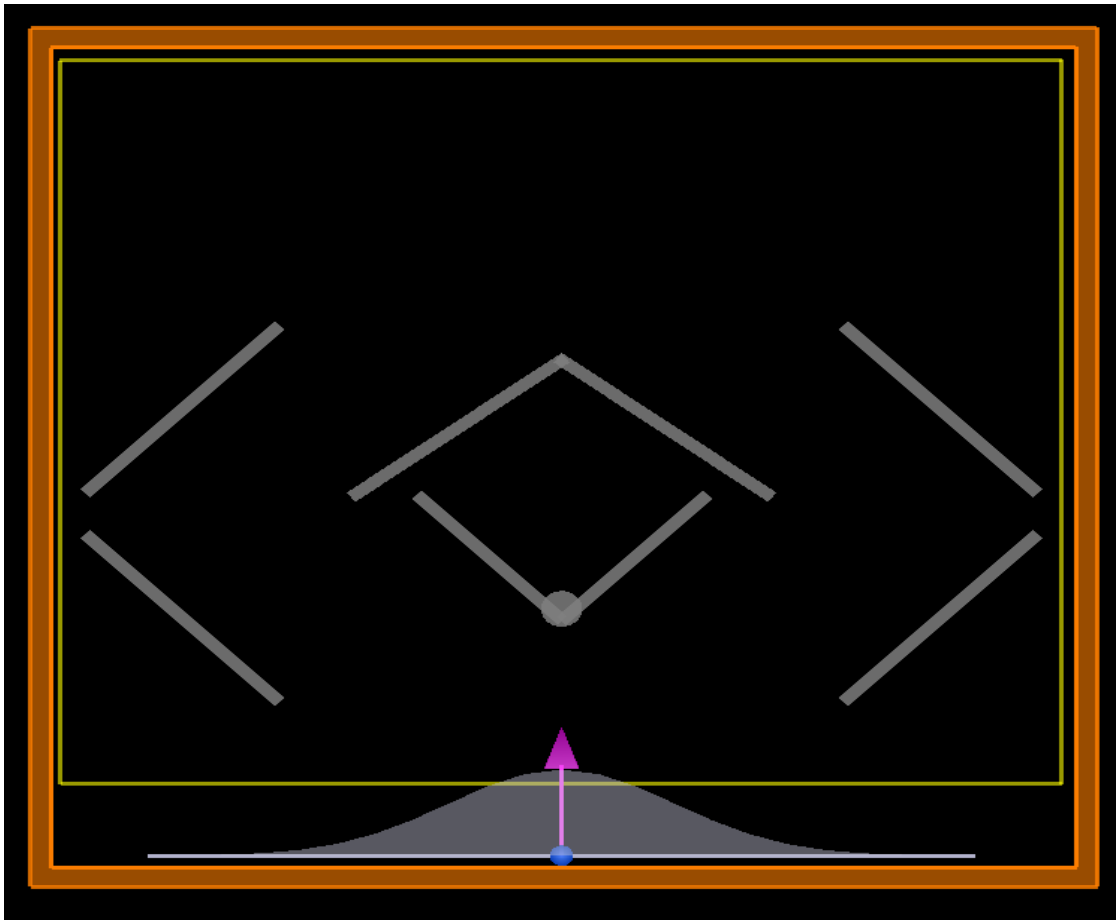

Figure 3.22 Illustration of the design with rounded edge V shape mirror

Figures (3.24, 3.25) show the result of the Electric field propagation versus the position through the design for the rounded edge V shape mirror. The first rounded shape mirror shows the division of the input beam into two symmetrically SGB, thus the division is still occurring with the rounded edge but there are some reflections that are taking place specially in the visible range.

.

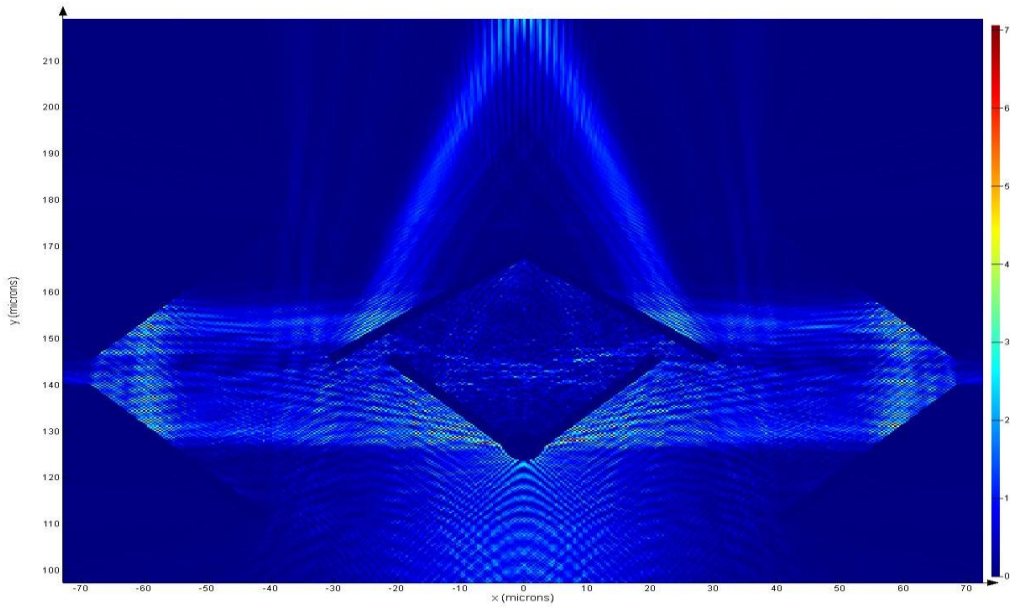

Figure 3.23 Electric Field intensity versus position for wavelength 700 nm in the visible range with rounded edge V shape mirror

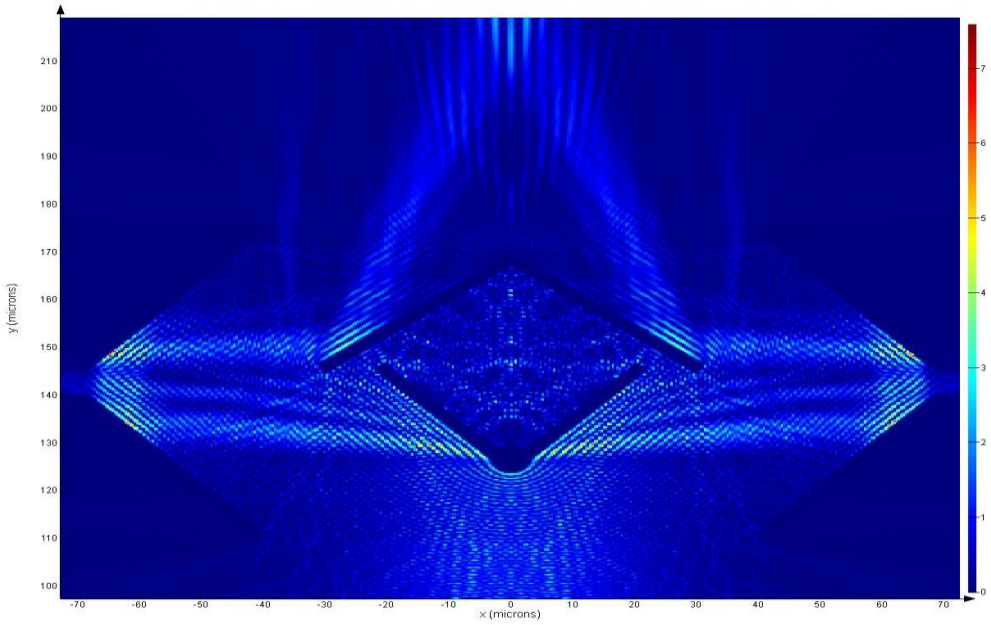

Figure 3.24 Electric Field intensity versus position for wavelength 1.55 µm in the IR range with rounded edge V shape mirror

The interference pattern versus the x position is given in Figure 3.26 and Figure 3.27 for the wavelengths 700 nm and 1.55 μm respectively.

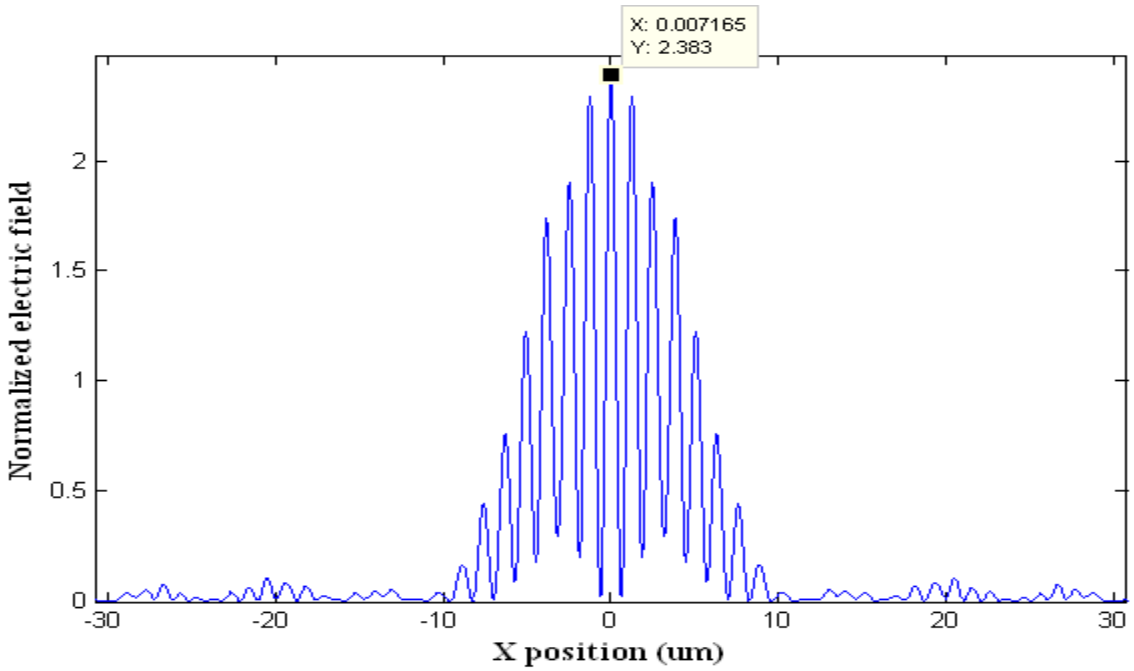

Figure 3.25 Interference pattern (normalized electric field versus x position) for working wavelength 700 nm

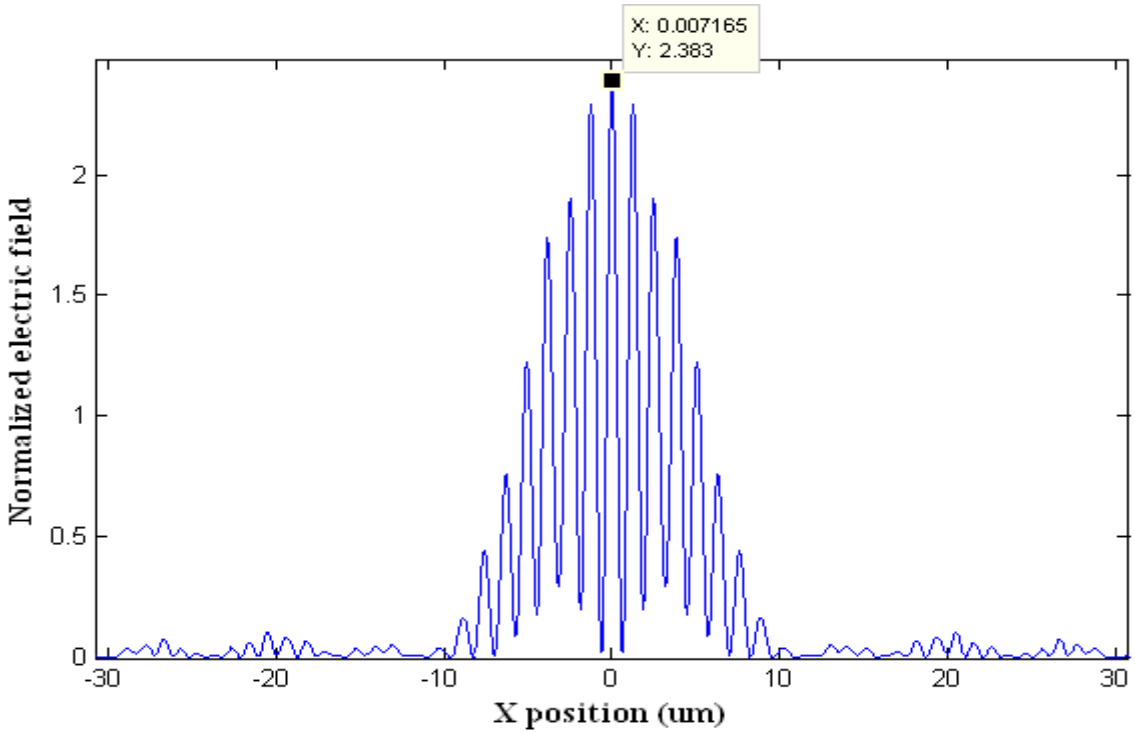

Figure 3.26 Interference pattern (normalized electric field versus x position) for working wavelength 1.55 μm

After verifying the working principle of the interferometer, Section 3.2.3 presents a study on the propagation distance that will help in finding the optimum point at which the detector can be placed. Finally a mechanical model of the movable structure of the mirrors is described in order to achieve large displacement to enhance the resolution of the interferometer.

3.2.3 Propagation distance effect

In the following part, a study for the propagation distance at which the output signal is detected is conducted. In this model we assume that the input source is a Gaussian beam with a beam waist w_0 30 µm/2. Additionally as it was shown in the design, the output mirrors are tilted to allow the occurrence of the interference between the two SGB. In order to introduce interference between the two SGB at small propagation distance, a tilt angle in the final mirror should be introduced. The tilted mirror tilts the phase front of the SGB and increase the number of the fringes in the interference pattern. According to the titling angle introduced the interference pattern can be enhanced by introducing a titling angle that allow the two SGB to be merged together which increase the intensity of the detected signal. In this study a tilting angle of 40^o is used.

In the following step a variation is made on the propagation distance at which the output is detected in order to have an idea about the detector place, the variation is done under 40^o tilting angle and at a working wavelength 700 nm.

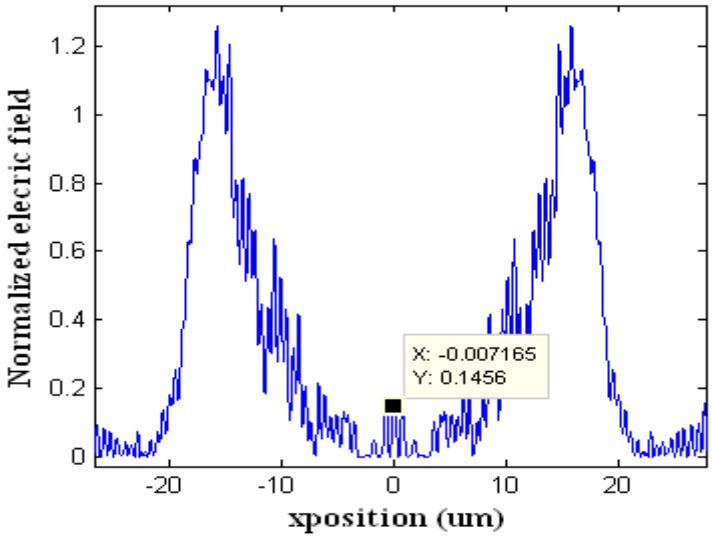

Figure 3.27 Intensity versus position at propagation distance 10 µm

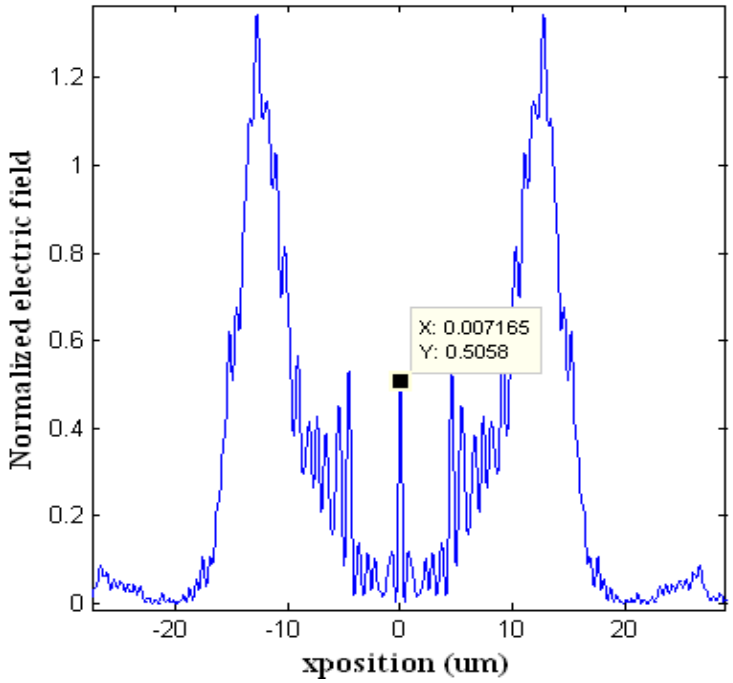

Figure 3.28 Intensity versus position at propagation distance 20 µm

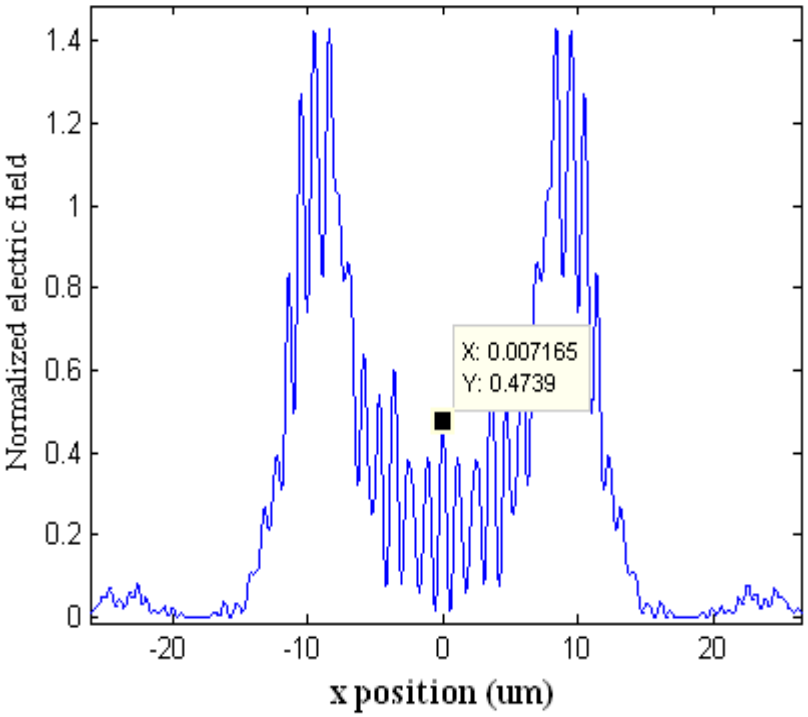

Figure 3.29 Intensity versus position at propagation distance 30 µm

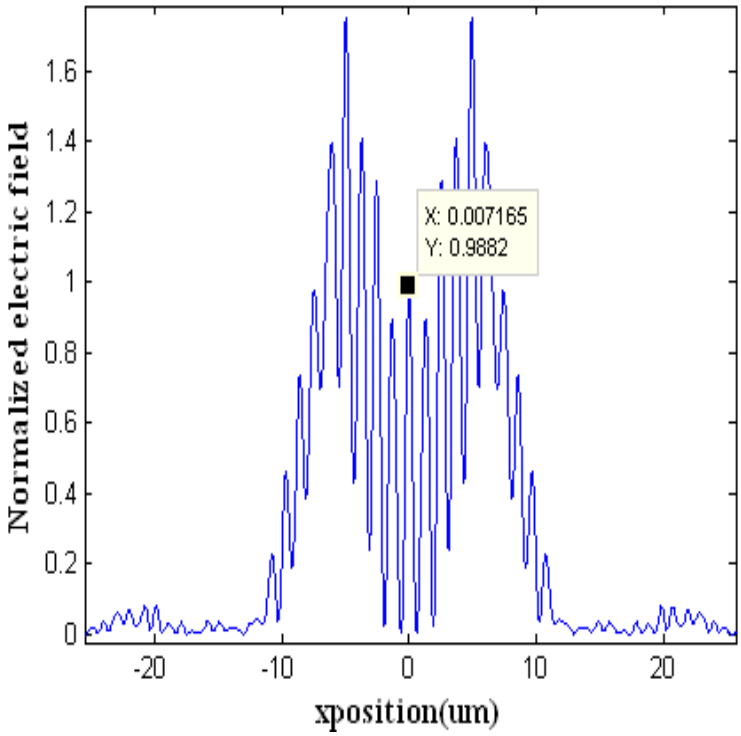

Figure 3.30 Intensity versus position at propagation distance 40 µm

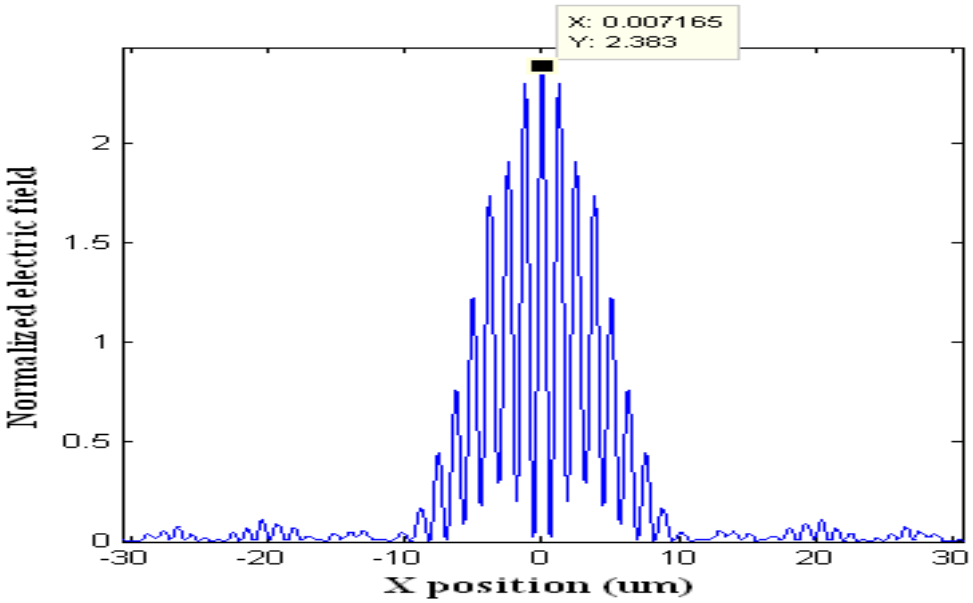

Figure 3.31 Intensity versus position at propagation distance 50 µm

Figure (3.32) to Figure (3.36) show the effect of the propagation distance at which the output signal is detected. The figures show that when the propagation distance increases, the intensity increases. This is due to the diffraction effect that is taken into consideration and results in more interference between the SBG, and as we approach to the tilted mirror the intensity decrease as the two SGB did not interfere completely yet, accordingly the point at which the detector will be placed has to be chosen carefully.

Giving the previous results, an interference pattern can be obtained without introducing a tilting but at longer distance of propagation due to the diffraction of the SGBs that will result in an interference pattern. Additionally the point at which the detector is placed has to be chosen carefully to get the higher intensity and resolution of the resulting interferogram.

The resolution of the spectrometer depends on the optical path difference between the two SGB. One of the major drawbacks of using MEMS technology to miniaturize the optical spectrometer is the limited mechanical displacement achievable in the MEMS mechanical systems. Therefore, increasing the OPD to enhance the spectrometer performance is considered a challenge in the MEMS based spectrometer. Our design proposes a novel approach to increase the OPD over the mechanical displacement by a factor of four using differential displacement between the right and left reflecting mirrors. A higher multiplication factor is achievable by repeating the mirror structure hold by the comb drive. However, using large number of reflecting mirror will decrease the detected optical power due to the power loss in the mirrors. Therefore, a tradeoff between the resolution and the signal to noise ratio is needed.

3.2.4 Mechanical model

Electrostatic Comb drive actuators are the most commonly used MEMS actuators devices. It is composed of two sets of fingers, one of them is fixed and the other one is movable. Once a driving voltage is applied between the two sets of fingers, this produces electrostatic force between the comb-fingers, which drive the movable fingers of the comb. Generally this result in a longitudinal (F_x) and lateral (F_y) electrostatic force (Figure 3.28), however the lateral forces balance out each other where $\sum F_y = 0$, and the longitudinal force is the one driving the movement of the structure. The force generated by the structure is relative to the variation in the capacitance between the two combs finger, the applied voltage, the number of comb fingers and the gap between the fingers [96, 97].

The capacitance *"C"* between the comb fingers can be described by [97]:

$$C = \frac{2N\varepsilon_0\varepsilon_r w(x + x_o)}{g} \qquad 3.19$$

Where N is the number of fingers, ε_0 is the vacuum permittivity ε_r is the relative permittivity of the material, t is the thickness, xo is the initial overlap between the comb finger, x is the displacement of the structure (which is equivalent to the half of the optical path difference), and g is the gap between the fingers. The resulting electrostatic force is relative to the capacitance and can be described by [97]:

$$F = \frac{1}{2}\frac{\partial C}{\partial x}V^2 \qquad 3.20$$

Where V is the driving voltage applied between the moving and fixed set of fingers.

Substituting Eq. (3.19) in (3.20), the force can be given by:

$$F = \frac{Nw\varepsilon_0\varepsilon_r V^2}{g} \qquad 3.21$$

The movable sets of fingers are attached to a spring to create a restoring mechanical force that opposes the electrostatic force generated. In this case a folded beam suspension is used which has a spring constant *"K"* that can be given by:

$$K = \frac{2Etw^3}{L^3} \qquad 3.22$$

Where E is the young's modulus of the material, w is the width of the beam, L is the length. The mechanical force is given by:

$$F = Kx \qquad 3.23$$

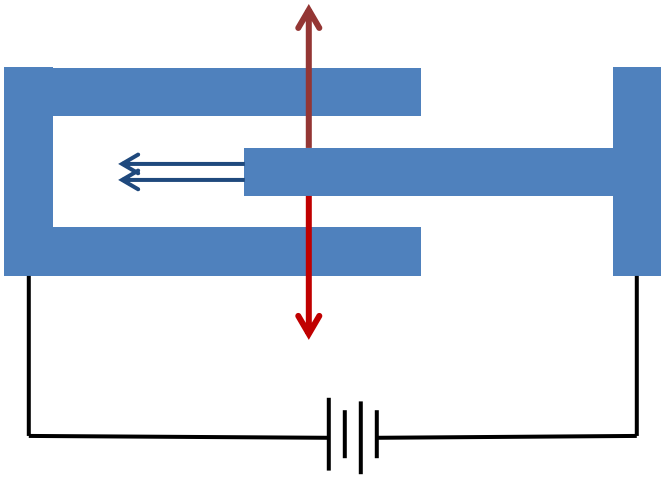

Figure 3.32 Schematic describing the electrostatic force generated between the comb fingers when a driving voltage is applied

The design of our comb drive actuator is shown in Figure (3.29), in which a folded beam flexure are used as this design of flexure highly decrease the expansion of axial forces, hence enabling the achievement of higher values of linear deflection. Consequently this design of flexure meets our requirements to achieve high values of displacements.

For this design, structural mechanics module in Comsol Multiphysics is used; Static analysis is conducted in which a force equivalent to the driving voltage is applied on the structure giving us the appropriate displacement. In the simulation only the movable part is simulated fixed in the folded flexure beam, additionally Comsol enable the study of the half of the structure if it is symmetric, using "Symmetry" in the boundary condition.

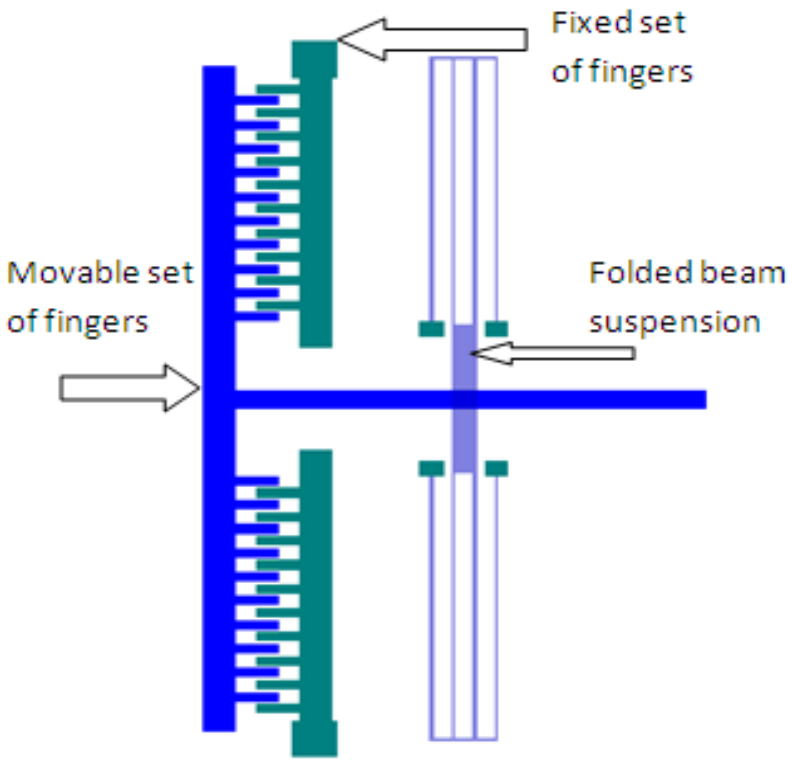

Figure 3.33 Schematic of the comb-drive design

The goal of this design is to achieve 160 μm mechanical displacement; accordingly conducting an analytical model on Matlab, the design made resulted in 160.6 μm mechanical displacement with 70 V driving voltage. Commonly the association of the electrostatic force with the driving voltage, result in familiar phenomena, which is "pull-in" when the voltage exceeds certain edge the fingers stick together "front sticking". As we are working in a large displacement range with a relatively high value of a driving voltage, the pull-in condition was taken into consideration in the modeling to verify that the critical value of the pull-in voltage does not occur before 70 V, which is the value of the driving voltage used to achieve the 160.6 μm mechanical displacement, from (Figure 3.30), the point at which the intersection occur between the electrostatic force and the restoring force gives us the value of the pull-in distance x_p, applying this value in Eq.(3.24), the critical value of the driving voltage at which the front sticking occur V_{cr_pullin} is calculated [96].

$$V_{cr} = \sqrt{\frac{Kx_p}{N\varepsilon_0 w(\frac{1}{g} - \frac{b}{(d - x_p)^2})}} \quad 3.24$$

Where *k* is the spring constant, x_p is the displacement at which pull-in occur "value calculated from point of intersection Figure 3.30a", N number of fingers, $\varepsilon_0$is the vaccum permittivity ε_r is the relative permittivity of the material, *w* the width of the fingers, *g* is the gap between the fingers and *d* is the initial displacement between the comb fingers.

From Figure 3.30, the pull-Voltage is calculated from x_p, and the value at which pull-in occur is 80 V. Afterward the design is modeled on Comsol Mutiphysics software to verify the results achieved with Matlab, using the structural mechanics module, and by simulating half of the structure using the symmetry condition as shown in Figure 3.31, and by applying an appropriate force equivalent to the 70 V driving voltage, the FEM simulation results shows 160.8 μm displacement as shown in Figure 3.31, which is in a good agreement with the analytical model.

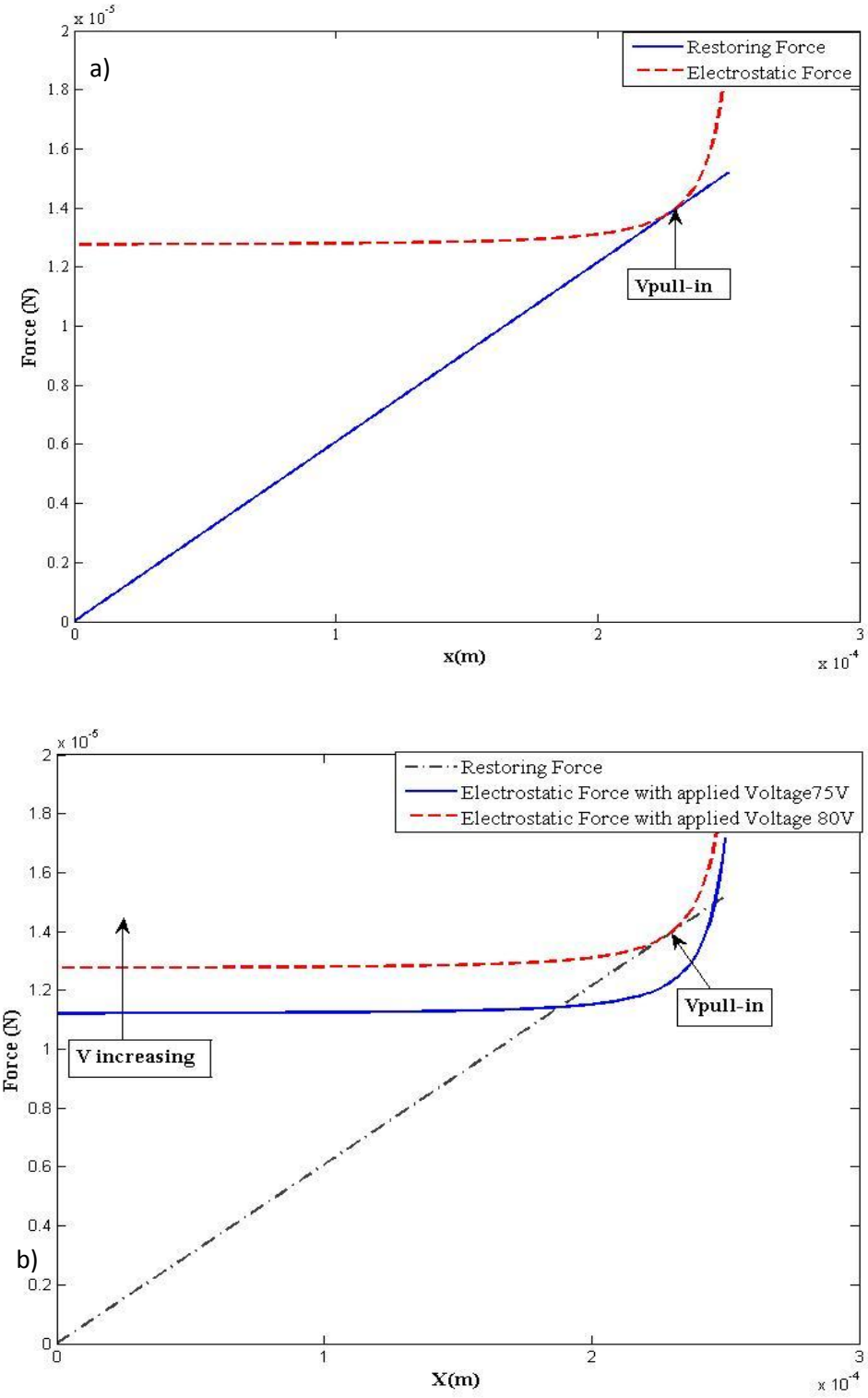

Figure 3.34 a) Electrostatic force and restoring force versus displacement the point of intersection determine the pull-in point b) The effect of the voltage increase on the pull-in phenomena

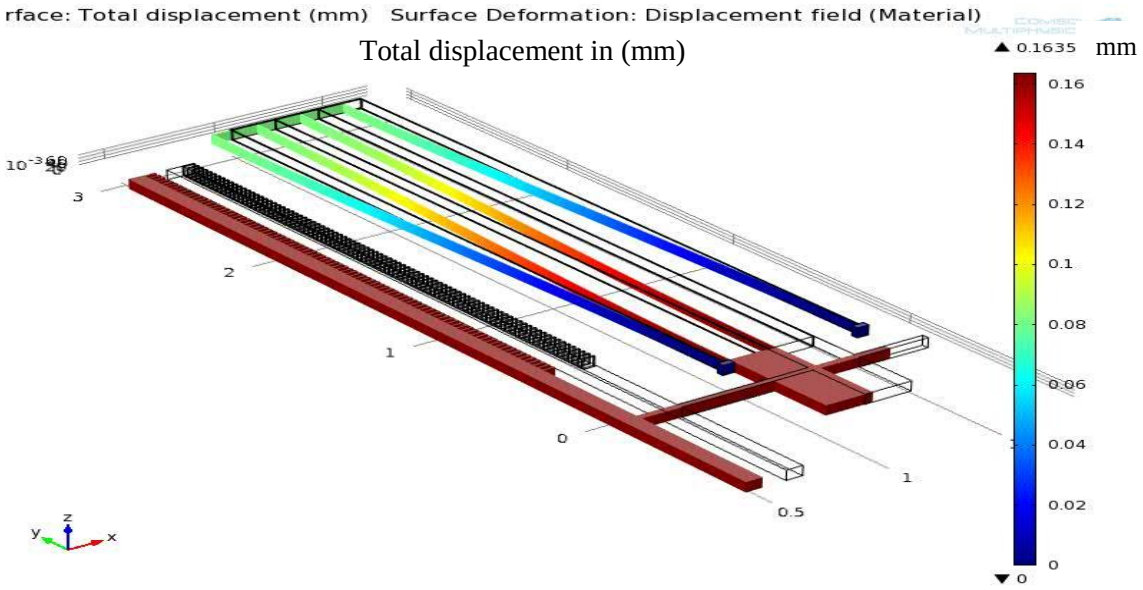

Figure 3.35 Total displacement of the comb drive in mm

In this section a new approach for optical beam splitting in the MEMS based optical spectrometer was introduced. The approach is based on using V shaped mirror to spatially divide the input Gaussian beam into two symmetric Semi-Gaussian beams. The mirror design presented here makes the optical path difference four times the mechanical displacement; which increases the spectrometer resolution. The design presented here is fully integrated and it has the potential to be used for commercial application.

4 Chapter IV Conclusions and future work

Conclusion

In this work the main objective was to develop microfluidics microchannels that can be used on a microfluidic platform for the handling and separation of fluids. The second part was to develop a microspectrometer that can be integrated afterward with the microfluidic platform as an optical detector.

In this context polymer based microchannels using a new acrylic thick negative photoresist “AZ nxt 125” were fabricated with thickness up to 300 µm using a single spinning process. This kind of photoresist offers many advantages over the SU-8 conventionally used such as rapid processing because in the case of AZ125nxt photoresist, post exposure baking is eliminated which makes the process less time consuming, in addition it has a good adhesion to silicon thus eliminating the use of adhesion promoter. These results show that this kind of resist has a better performance than the conventional one SU-8, so it may replace it in many applications in order to have a biocompatible and robust design with lower costs and short processing time.

In the second part, simulations of lamellar grating microspectrometer were conducted, followed by a stability analysis to study the behavior and the excitation of the microspectrometer. The maximum displacement achieved is 84 µm, with applied voltage 28 V, which gives a resolution of 0.3 nm to 1.13 nm for wavelengths 380 nm and 750 nm respectively. Afterward a study on different design parameter was given to study its effect on the maximum displacement that can be achieved, and it was concluded that by varying the design parameters of the comb drive and suspension a compromise between the higher displacement and the mode separation has to be done. Additionally the spaces between the folded beams affect highly the fundamental mode of oscillation which may eliminate the out of plane mode to be the first mode of oscillations, hence destructing the behavior of the design.

Finally simulation results of a novel approach for beam splitting in interferometer based microspectrometers is given, using V shape mirror with modified rounded edge instead of using a sharp edge to facilitate the fabrication process. In this case the incident beam was splitted into two Semi-Gaussian beams by the V shape mirror and an interferogram was observed at the output, hence eliminating the use of beam splitters that are difficult to integrate in MEMS technology. The design was studied for the visible range and infra-red range and it is working for both ranges without any modification in the design parameters only the output detector will be different for each range of wavelengths. In addition a study on the propagation distance is conducted which will help in finding the optimum point at which the detector can be placed. Also a mechanical model for electrostatic actuation was done for the movable reflecting mirror with a maximum displacement of 160.8 μm thus given a maximum total displacement with the mirrors design of 160.8 μm times four due to the differential displacement between the right and left reflecting mirrors thus achieving higher displacement which results in a higher resolution of the interferometer.

Future Work

- In order to develop the microfluidic platform for the heavy metal detection, it would be useful to introduce a separation scheme into the microchannel, thus increasing the selectivity of the system
- A study on the deposition of a sensitive optical material for the detection and the effect of the fluid flow and viscosity on the efficiency of the detection.
- For the optical interferometer, by repeating the mirror structure hold by the comb drive a higher multiplication factor for the displacement could be achieved thus increasing the resolution. However using a higher number of reflecting mirrors may decrease the detected power. Accordingly a tradeoff between the resolution and detected power had to be taken into consideration

5 References

[1] G. L. Turdean, "Design and Development of Biosensors for the Detection of Heavy Metal Toxicity," International Journal of Electrochemistry, vol. 2011, 2011.

[2] N. Langford and R. Ferner, "Toxicity of mercury," Journal of human hypertension, vol. 13, p. 651, 1999.

[3] Z. Zou, "Heavy metals measurement using polymer lab-on-a-chips and its applications in environmental health", vol. 70, 2009.

[4] T. Mayr, "Optical Sensors for the Determination of Heavy Metal Ions," 2002.

[5] I. Oehme and O. S. Wolfbeis, "Optical sensors for determination of heavy metal ions," MicrochimicaActa, vol. 126, pp. 177-192, 1997.

[6] M. T. S. R. Gomes, "Application of piezoelectric quartz crystals to the analysis of trace metals in solution: a review," IEEE sensors journal, vol. 1, pp. 109-118, 2001.

[7] R. W. Cattrall, Chemical sensors vol. 1: Oxford University Press New York, 1997.

[8] K. J. Albert, N. S. Lewis, C. L. Schauer, G. A. Sotzing, S. E. Stitzel, T. P. Vaid, and D. R. Walt, "Cross-reactive chemical sensor arrays," Chemical Reviews, vol. 100, pp. 2595-2626, 2000.

[9] R. Malstrom and T. Hirschfeld, "On-line uranium determination using remote fiber fluorimetry," Du Pont de Nemours (EI) and Co., Aiken, SC (USA). Savannah River Lab.; Lawrence Livermore National Lab., CA (USA)1983.

[10] R. Malstrom, "Uranium analysis by remote fiber fluorimetry," Du Pont de Nemours (EI) and Co., Aiken, SC (USA).Savannah River Lab.1988.

[11] P. Bühlmann, E. Pretsch, and E. Bakker, "Carrier-Based Ion-Selective Electrodes and Bulk Optodes.Part 2.Ionophores for Potentiometric and Optical Sensors," ChemInform, vol. 29, pp. no-no, 1998.

[12] F. P. Schmidtchen and M. Berger, "Artificial organic host molecules for anions," Chemical Reviews, vol. 97, pp. 1609-1646, 1997.

[13] J. R. Lakowicz, Topics in Fluorescence Spectroscopy: Volume 4: Probe Design and Chemical Sensing: Springer, 1994.

[14] S. A. El-Safty, "Functionalized hexagonal mesoporous silica monoliths with hydrophobic azo-chromophore for enhanced Co (II) ion monitoring," Adsorption, vol. 15, pp. 227-239, 2009.

[15] M. Alfimov, S. Gromov, W. Retting, B. Strhmel, S. Schroder, and H. Seifert, "Applied fluorescence in chemistry, biology, and medicine," ed: Eds W. Rettig, B. Strehmel, S. Schrader, H. Seifert, Springer Verlag, Berlin, 1999.

[16] S. A. El-Safty, D. Prabhakaran, Y. Kiyozumi, and F. Mizukami, "Nanoscale Membrane Strips for Benign Sensing of HgII Ions: A Route to Commercial Waste Treatments," Advanced Functional Materials, vol. 18, pp. 1739-1750, 2008.

[17] J. Shi, F. Tang, H. Xing, H. Zheng, B. Lianhua, and W. Wei, "Electrochemical detection of Pb and Cd in paper-based microfluidic devices," Journal of the Brazilian Chemical Society, vol. 23, pp. 1124-1130, 2012.

[18] J. Wang and K. Rogers, Electrochemical sensors for environmental monitoring: A review of recent technology: US Environmental Protection Agency, Office of Research and Development, Environmental Monitoring and Support Laboratory, 1995.

[19] K. S. Yun, J. Gil, J. Kim, H. J. Kim, K. H. Kim, D. Park, J. Y. Kwak, H. Shin, K. Lee, and J. Kwak, "A miniaturized low-power wireless remote environmental monitoring system using microfabricated electrochemical sensing electrodes," 2003, pp. 1867-1870.
[20] G. Aragay and A. Merkoçi, "Nanomaterials application in electrochemical detection of heavy metals," ElectrochimicaActa, 2012.
[21] Y. Liu, Y. Li, and X. P. Yan, "Preparation, Characterization, and Application of L-Cysteine Functionalized Multiwalled Carbon Nanotubes as a Selective Sorbent for Separation and Preconcentration of Heavy Metals," Advanced Functional Materials, vol. 18, pp. 1536-1543, 2008.
[22] J. Morton, N. Havens, A. Mugweru, and A. K. Wanekaya, "Detection of Trace Heavy Metal Ions Using Carbon Nanotube-Modified Electrodes," Electroanalysis, vol. 21, pp. 1597-1603, 2009.
[23] T. H. Kim, J. Lee, and S. Hong, "Highly selective environmental nanosensors based on anomalous response of carbon nanotube conductance to mercury ions," The Journal of Physical Chemistry C, vol. 113, pp. 19393-19396, 2009.
[24] W. Chang, D. Tzebotich, L. P. Lee, and D. Liepmann, "Blood flow in simple microchannels," 2000, pp. 311-315.
[25] G. Hetsroni, A. Mosyak, E. Pogrebnyak, and L. Yarin, "Fluid flow in micro-channels," International Journal of Heat and Mass Transfer, vol. 48, pp. 1982-1998, 2005.
[26] M. P. Y. N. Soin and F. Ibrahim, "A Review on Design Parameters of Micro-Fluidic System," 2007, p. 316.
[27] S. K. Mitra and S. Chakraborty, Microfluidics and Nanofluidics Handbook: Fabrication, Implementation, and Applications vol. 2: CRC Press, 2011.
[28] B. H. Weigl, R. L. Bardell, and C. R. Cabrera, "Lab-on-a-chip for drug development," Advanced Drug Delivery Reviews, vol. 55, pp. 349-377, 2003.
[29] Y. C. Chen, G. Y. Chen, Y. C. Lin, and G. J. Wang, "A lab-on-a-chip capillary network for red blood cell hydrodynamics," Microfluidics and Nanofluidics, vol. 9, pp. 585-591, 2010.
[30] S. Chakraborty, Microfluidics and microfabrication: Springer Verlag, 2010.
[31] S. SENTURIA, "Microsystem design (2nd corr. printing 2005)," Recherche, vol. 67, p. 02, 2001.
[32] R. W. Tjerkstra, M. De Boer, E. Berenschot, J. Gardeniers, A. van den Berg, and M. Elwenspoek, "Etching technology for microchannels," 1997, pp. 147-152.
[33] J. Meint, "de Boer et al., Micromachining of Buried Micro Channels in Silicon, Mar. 2000," Journal of Microelectromechanical systems, vol. 9, pp. 94-103.
[34] J. L. Perry and S. G. Kandlikar, "Review of fabrication of nanochannels for single phase liquid flow," Microfluidics and Nanofluidics, vol. 2, pp. 185-193, 2006.
[35] I. Papautsky, J. Brazzle, H. Swerdlow, and A. B. Frazier, "A low-temperature IC-compatible process for fabricating surface-micromachined metallic microchannels," Microelectromechanical Systems, Journal of, vol. 7, pp. 267-273, 1998.
[36] K. B. Lee and L. Lin, "Surface micromachined glass and polysiliconmicrochannels using MUMPs for BioMEMS applications," Sensors and Actuators A: Physical, vol. 111, pp. 44-50, 2004.
[37] I. Papautsky, B. K. Gale, S. Mohanty, T. A. Ameel, and A. B. Frazier, "Effects of rectangular microchannel aspect ratio on laminar friction constant," Proceedings of SPIE-

The International Society for Optical Engineering, Proceedings of the 1999 Microfluidic Devices and Systems II, Santa Clara, vol. 3877, pp. 147-158, 1999.
[38] M. L. Adams, M. Enzelberger, S. Quake, and A. Scherer, "Microfluidic integration on detector arrays for absorption and fluorescence micro-spectrometers," Sensors and Actuators A: Physical, vol. 104, pp. 25-31, 2003.
[39] A. Bahadorimehr, J. Yunas, and B. YeopMajlis, "Low cost fabrication of microfluidic microchannels for Lab-On-a-Chip applications," 2010, pp. 242-244.
[40] J. Friend and L. Yeo, "Fabrication of microfluidic devices using polydimethylsiloxane," Biomicrofluidics, vol. 4, p. 026502, 2010.
[41] A. Tuantranont, T. Lomas, T. Maturos, A. Wisitsora-at, P. Thavarungkul, P. Kanatharana, W. Limbut, and S. Loyprasert, "Development of low-cost microfluidic systems for lab-on-a-chip biosensor applications," NanoBiotechnology, vol. 2, pp. 143-149, 2006.
[42] S. Westwood, "Polymer microchannels with integrated interconnect and applications as cell research platforms," SIMON FRASER UNIVERSITY, 2009.
[43] J. C. McDonald and G. M. Whitesides, "Poly (dimethylsiloxane) as a material for fabricating microfluidic devices," Accounts of chemical research, vol. 35, pp. 491-499, 2002.
[44] S. M. Westwood, S. Jaffer, O. A. Lui, and B. L. Gray, "Thick SU-8 and PDMS three-dimensional enclosed channels for free-standing polymer microfluidic systems," 2007, pp. 12-15.
[45] Y. Hongbin, Z. Guangya, C. F. Siong, W. Shouhua, and L. Feiwen, "Novel polydimethylsiloxane (PDMS) based microchannel fabrication method for lab-on-a-chip application," Sensors and Actuators B: Chemical, vol. 137, pp. 754-761, 2009.
[46] R. Lo and E. Meng, "A reusable in-plane polymer integrated microfluidic interconnect," 2007, pp. 2067-2070.
[47] R. Lo and E. Meng, "Integrated and reusable in-plane microfluidic interconnects," Sensors and Actuators B: Chemical, vol. 132, pp. 531-539, 2008.
[48] R. Lo and E. Meng, "Reusable, adhesiveless and arrayed in-plane microfluidic interconnects," Journal of Micromechanics and Microengineering, vol. 21, p. 054021, 2011.
[49] R. Lo, "Modular bio microelectromechanical systems (bioMEMS)| Intraocular drug delivery device and microfluidic interconnects," UNIVERSITY OF SOUTHERN CALIFORNIA, 2010.
[50] R. Wolffenbuttel, "MEMS-based optical mini-and microspectrometers for the visible and infrared spectral range," Journal of Micromechanics and Microengineering, vol. 15, p. S145, 2005.
[51] J. Antila, "Miniaturized spectrometer technologies," 2010, pp. 1-4.
[52] A. N. Das, J. Sin, D. O. Popa, and H. E. Stephanou, "Design and manufacturing of a fourier transform microspectrometer," 2008, pp. 837-840.
[53] R. F. Wolffenbuttel, "State-of-the-art in integrated optical microspectrometers," Instrumentation and Measurement, IEEE Transactions on, vol. 53, pp. 197-202, 2004.
[54] S. Grabarnik, R. Wolffenbuttel, A. Emadi, M. Loktev, E. Sokolova, and G. Vdovin, "Planar double-grating microspectrometer," Optics express, vol. 15, pp. 3581-3588, 2007.
[55] R. A. Crocombe, "MEMS technology moves process spectroscopy into a new dimension," Spectroscopy Europe, vol. 16, pp. 16-19, 2004.

[56] H. P. Herzig, T. Scharf, and O. Manzardo, "Microspectrometer: From ideas to product," 2008, pp. 58-59.
[57] S. Grabarnik, A. Emadi, H. Wu, G. De Graaf, G. Vdovin, and R. Wolffenbuttel, "Fabrication of an imaging diffraction grating for use in a MEMS-based optical microspectrograph," Journal of Micromechanics and Microengineering, vol. 18, p. 064006, 2008.
[58] B. Kim, J. Sinibaldi, and G. Karunasiri, "MEMS Scanning Diffraction Grating Spectrometer," 2006, pp. 46-47.
[59] S. C. Truxal, N. T. Huang, and K. Kurabayashi, "A nano grating tunable mems optical filter for high-speed on-chip multispectral fluorescent detection," 2009, pp. 6693-6695.
[60] A. Zarifkar and R. Yousefi, "A new binary multi-layer diffraction grating," 2008, pp. 151-154.
[61] S. Grabarnik, A. Emadi, H. Wu, G. de Graaf, and R. Wolffenbuttel, "Microspectrometer with a concave grating fabricated in a MEMS technology," Procedia Chemistry, vol. 1, pp. 401-404, 2009.
[62] C. W. Wong, Y. Jeon, G. Barbastathis, and S. G. Kim, "Analog tunable gratings driven by thin-film piezoelectric microelectromechanical actuators," Applied optics, vol. 42, pp. 621-626, 2003.
[63] S. Bhalotraa, H. Kunga, D. Knippb, H. Stiebigc, and D. Millera, "All-silicon standing-wave microspectrometer with tunable spectral resolution."
[64] P. R. Griffiths and J. A. De Haseth, Fourier transform infrared spectrometry vol. 171: John Wiley & Sons, 2007.
[65] M. Ebermann and N. Neumann, "New MEMS Microspectrometer for Infrared Absorption Spectroscopy."
[66] C. Ataman and H. Urey, "Vertical resonant comb actuators for fourier transform spectroscopy," 2006, pp. 44-45.
[67] H. Omran, M. Medhat, B. Mortada, B. Saadany, and D. Khalil, "A Fully Integrated Mach-ZhenderMEMSInterferometer with Two Complementary Outputs," Quantum Electronics, IEEE Journal of, pp. 1-1, 2011.
[68] K. Yu, D. Lee, U. Krishnamoorthy, N. Park, and O. Solgaard, "Micromachined Fourier transform spectrometer on silicon optical bench platform," Sensors and Actuators A: Physical, vol. 130, pp. 523-530, 2006.
[69] B. Saadany, T. Bourouina, M. Malak, M. Kubota, Y. Mita, and D. Khalil, "A Miniature Michelson Interferometer using Vertical Bragg Mirrors on SOI," 2006, pp. 50-51.
[70] J. M. Dell, J. S. Milne, J. Antoszewski, A. J. Keating, L. P. Schuler, and L. Faraone, "MEMS-based Fabry-Perot microspectrometers for agriculture," 2009, p. 73190K.
[71] A. Keating, J. Antoszewski, K. Silva, K. Winchester, T. Nguyen, J. Dell, C. Musca, L. Faraone, P. Mitra, and J. Beck, "Design and characterization of Fabry–Perot MEMS-based short-wave infrared microspectrometers," Journal of electronic materials, vol. 37, pp. 1811-1820, 2008.
[72] J. F. J. Lo, P. Butte, Q. Fang, S. J. Chen, T. Papaioanou, E. S. Kim, M. Gundersen, and L. Marcu, "Multilayered MOEMS Tunable Spectrometer for Fluorescence Lifetime Detection," Photonics Technology Letters, IEEE, vol. 22, pp. 486-488, 2010.
[73] J. P. Carmo, R. P. Rocha, M. Bartek, G. de Graaf, R. F. Wolffenbuttel, and J. H. Correia, "A review of visible-range Fabry–Perot microspectrometers in silicon for the industry," Optics & Laser Technology, 2012.

[74] M. Blomberg, H. Kattelus, and A. Miranto, "Electrically tunable surface micromachinedFabry–Perot interferometer for visible light," Sensors and Actuators A: Physical, vol. 162, pp. 184-188, 2010.
[75] J. Milne, J. Dell, A. Keating, L. Schuler, and L. Faraone, "Widely tunable Fabry-Perot optical filter using fixed-fixed beam actuators," 2008, pp. 66-67.
[76] C. P. Chang and R. S. Huang, "A 16-channel array-type microspectrometer using integrated Fabry-Perot etalons and lateral pin photodetectors," 2003, pp. 675-678.
[77] F. Lee, G. Zhou, H. Yu, and F. S. Chau, "A MEMS-based resonant-scanning lamellar grating Fourier transform micro-spectrometer with laser reference system," Sensors and Actuators A: Physical, vol. 149, pp. 221-228, 2009.
[78] H. R. Seren, S. Holmstrom, N. P. Ayerden, J. Sharma, and H. Urey, "Lamellar-Grating-Based MEMS Fourier Transform Spectrometer," Microelectromechanical Systems, Journal of, pp. 1-9, 2010.
[79] W. Shouhua, Y. Hongbin, and C. F. Siong, "A Miniaturized Lamellar Grating Based Fourier Transform Spectrometer With Electrostatic Actuation," Sensors Journal, IEEE, vol. 10, pp. 1869-1874, 2010.
[80] C. Ataman, H. Urey, and A. Wolter, "A Fourier transform spectrometer using resonant vertical comb actuators," Journal of Micromechanics and Microengineering, vol. 16, p. 2517, 2006.
[81] O. Manzardo, R. Michaely, F. Schadelin, and H. P. Herzig, "Micro-sized spectrometer based on a lamellar grating interferometer," 2003, pp. 175-176.
[82] O. Ferhanoglu, H. R. Seren, S. Lüttjohann, and H. Urey, "Lamellar grating optimization for miniaturized fourier transform spectrometers," Optics express, vol. 17, pp. 21289-21301, 2009.
[83] O. Ferhanoglu, H. Seren, and H. Urey, "Lamellar grating interferometer based compact FT spectrometers," 2009, pp. 326-327.
[84] C. Ataman, H. Urey, S. Isikman, and A. Wolter, "A MEMS based visible-NIR Fourier transform microspectrometer," 2006, pp. 1-9.
[85] O. Manzardo, F. Schädelin, N. de Rooij, H. P. Herzig, S. Bühler, and C. Meier, "Micro-Fabricated Lamellar Grating Interferometer for Spectroscopy in the VIS and near-IR," Fourier Transform Spectroscopy/Hyperspectral Imaging and Sounding of the Environment, 2005.
[86] T. Ueda, "Development of a PDMS removable enclosure for microchannels using ultra-thick SU-8 process on silicon and glass substrates," School of Engineering Science-Simon Fraser University, 2008.
[87] U. S. DIXIT, "FINITE ELEMENT METHODS IN ENGINEERING," 2007.
[88] C. Ataman, O. Kaya, and H. Urey, "Analysis of parametric resonances in comb-driven microscanners," 2004, pp. 128-36.
[89] J. F. Rhoads, S. W. Shaw, K. L. Turner, J. Moehlis, B. E. DeMartini, and W. Zhang, "Generalized parametric resonance in electrostatically actuated microelectromechanical oscillators," Journal of Sound and Vibration, vol. 296, pp. 797-829, 2006.
[90] J. F. Rhoads, S. W. Shaw, K. L. Turner, J. Moehlis, B. E. DeMartini, and W. Zhang, "Nonlinear response of parametrically-excited MEMS," 2005.
[91] W. Zhang, R. Baskaran, and K. L. Turner, "Nonlinear dynamics analysis of a parametrically resonant MEMS sensor," 2002.

[92] G. K. Fedder, "Simulation of microelectromechanical systems," UNIVERSITY of CALIFORNIA, 1994.
[93] B. E. DeMartini, J. F. Rhoads, K. L. Turner, S. W. Shaw, and J. Moehlis, "Linear and nonlinear tuning of parametrically excited MEMS oscillators," Microelectromechanical Systems, Journal of, vol. 16, pp. 310-318, 2007.
[94] M. Mansuripur, "Certain computational aspects of vector diffraction problems," JOSA A, vol. 6, pp. 786-805, 1989.
[95] A. Taflove and S. C. Hagness, Computational electrodynamics: Artech house Boston, 1995.
[96] A. M. Elshurafa, K. Khirallah, H. H. Tawfik, A. Emira, A. K. S. Abdel Aziz, and S. M. Sedky, "Nonlinear dynamics of spring softening and hardening in folded-MEMS comb drive resonators," Microelectromechanical Systems, Journal of, pp. 1-16, 2011.
[97] R. Legtenberg, A. Groeneveld, and M. Elwenspoek, "Comb-drive actuators for large displacements," Journal of Micromechanics and Microengineering, vol. 6, p. 320, 1996.

[98] Kareem Khirallah, InasRamsis, MoahemdSerry, Mohamed A. Swillam, SherifSedky, "Spatial beam splitting for fully integrated MEMS interferometer", MOEMS and Miniaturized Systems XII conference, 2013SPIE 8616-22

.